Lateral Organisation of Modelbiomembranes and Partitioning of Dually Lipidated N-Ras Proteins into Ternary Model Raft Lipid Mixtures

Dissertation

zur Erlangung des Doktorgrades
der Naturwissenschaften
(Dr. rer. nat.)

eingereicht beim
Fachbereich Chemie
der Universität Dortmund

von

Dipl.-Chem. Chiara Nicolini

aus Rovigo, Italien

Dortmund 2006

Alla mia famiglia

Mein Dank gilt:

Contents _____ I

1   Introduction

1.1   Biological membranes

Biological membranes consist of a 5 nm thick fluid bilayer, which assembles membrane proteins. A simple but often used model to describe lipid membranes is known as "fluid mosaic" model (SINGER, 1972) and considers lipid membranes as being two dimensional fluids composed of two leaflets. The outer surface of the leaflet is composed primarily of the ionic and polar head groups and interacts with the aqueous solution, whereas the inner portion of the membrane is composed of the hydrocarbon chains of the lipids, which interact with each other through van der Waals forces. Integral membrane proteins and lipid molecules, which are confined to the bilayer, can diffuse laterally. According to this model, membranes are a dynamic system in which proteins and lipids can move and interact. Besides proteins, the major components of natural membranes are lipids and cholesterol, with a small amount of other materials such as fatty acids.

The plasma membrane encloses each cell, defines the cell extent and maintains the essential differences between its content and the environment, but not as a passive barrier it rather allows nutrients to enter and waste products to leave the cell. There are three main classes of lipid molecules in the plasma membrane: glycerophospholipids, sphingolipids and sterols (Figure 1.1). Phosphatidylcholine molecules are glycerophospholipids with a choline as polar head group. The two hydrophobic hydrocarbon tails tend to be not identical. They may differ in length and/or the presence/absence of double bonds. These differences in tail length and saturation are important because they influence the fluidity of the membrane. When unsaturated they possess low transition temperatures (T_m). Another determinant of membrane fluidity is cholesterol, which is the principle form of sterols found in vertebrates. Cholesterol molecules orient themselves in the bilayer with their hydroxyl groups close to the polar head groups of the phospholipid molecules. Their platelike steroid rings interact with, and partly immobilize, those regions of the hydrocarbon chains closest to the polar head groups, leaving the rest of the chain flexible. The third main components of the plasma membrane are sphingolipids. They are based on ceramide and have either a phosphocholine head group (sphingomyelin) or one of a range of carbohydrate structures (glycosphingolipids). They are embodied in all animal cell plasma membranes in the outer monolayer and show a most striking and consistent asymmetry in their distribution. These molecules are found only in the outer half of the bilayer, and their sugar groups are exposed to the surface of the cell. Sphingolipids differ from most biological phospholipids in containing

long, largely saturated acyl chains. This allows them to pack together tightly, a property that gives sphingolipids much higher melting temperatures than membrane phospholipids.

Due to the different lipid compositions of the two sides of the bilayer the plasma membrane is asymmetrical (Figure 1.2(B)). This aspect might have a function such as helping, for example, to keep membrane proteins properly oriented in the bilayer. All membrane proteins are associated with the membrane in a highly asymmetrical fashion, a feature crucial to their function (ALBERTS, 1983).
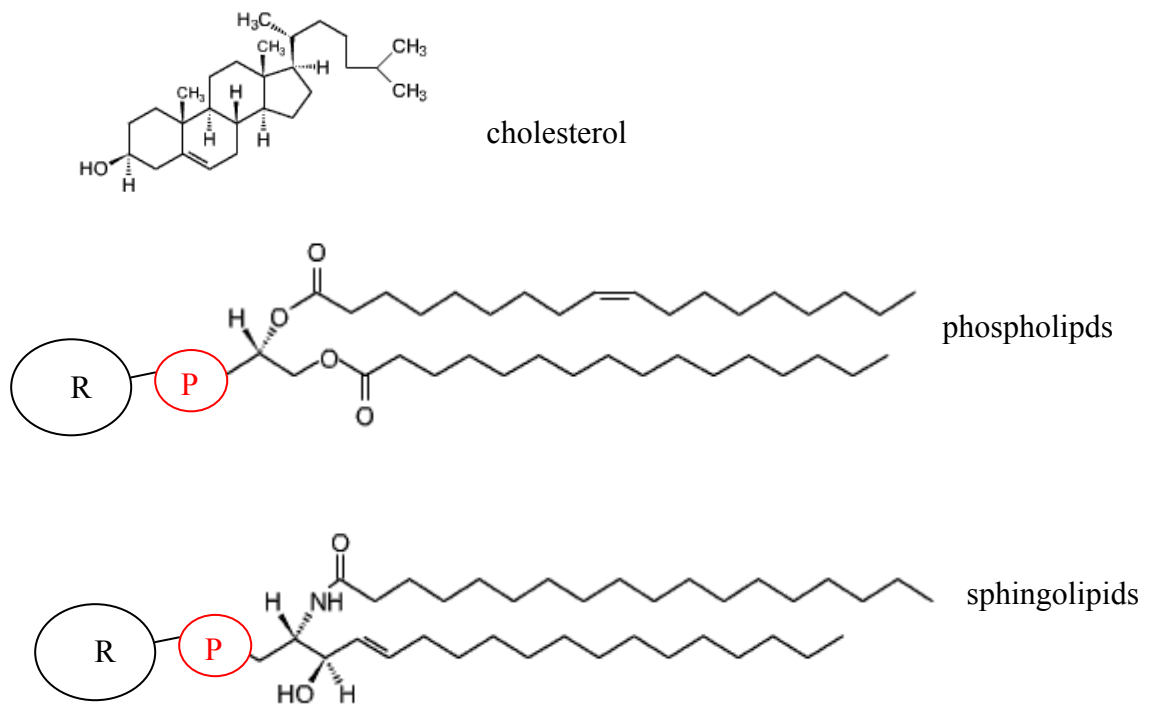
Figure 1.1 Chemical structure of cholesterol, phospholipid and sphingolipid, respectively.

1.1.1   Rafts and caveolae

The simple "fluid mosaic" model of cell membranes was refined in the last years through the postulation of the existence of fine structure in cell membranes in the form of lipid rafts. Lipid rafts are membrane microdomains that are enriched by cholesterol and glycosphingolipids (Figures 1.2(A) and 1.2 (B)). It was supposed they could be implicated in endocytic events (NABI, 2003; PARTON, 2003) as well as in the trafficking of cholesterol (IKONEN, 2000).

The original raft-like domain, which is still the only one that is identifiable morphologically, is the caveola. Caveolae are small plasma membrane invaginations with a diameter of ca. 25-150 nm (Figure 1.2(C)) (THORN, 2003). The invaginated structure of caveolae seems to be stabilized by the protein caveolin (FRA, 1995; LE, 2002). Originally, caveolae were isolated by extracting cells with 1% Triton X-100 at 4 °C and then floating the lysate on 5-30% sucrose gradient (BROWN, 1992). The resulting fractions included a variety of proteins like caveolin (ROTHBERG, 1992), GPI (glycosylphosphatidylinositol)-linked proteins (BROWN, 1992) and numerous proteins involved in cell signalling (FOSTER, 2003; VON HALLER, 2001). Caveolae could also be prepared using a non-detergent method (SCHNITZER, 1995), which separates invaginated caveolae from a low-density Triton X-100-resistant membrane fraction containing all the GPI-linked proteins. Thus, these findings suggested that detergent-resistant membranes comprise at least two types of domains – those that contain caveolin (caveolae) and those that lack caveolin (lipid rafts).

The problem to define lipid rafts is due the fact that different methods (detergent-based and non-detergent methods) and a variety of detergents, besides Triton-X-100, were applied in the last years to isolate raft fractions from the cell. Unsurprisingly, the use of different tools in the preparation of rafts yields membrane domains with lipid compositions different from those of standard, Triton-X-100-resistant membranes (SCHUCK, 2003). The observation that raft composition depends heavily on the method used to obtain it suggests that a raft is a highly dynamic moving target (LAI, 2003).

For the raft identification in live cells different techniques have been used recently including fluorescence resonance energy transfer (FRET) (VARMA, 1998; KENWORTHY, 2000), photonic force microscopy (PRALLE, 2000) and single molecule microscopy (SCHUTZ, 2000). The results suggest that rafts are relatively small, most probably in the low nanometre range. However, there is still considerable variation between the size estimated depending on the technique applied and, probably, on the specific molecule(s) traced and the biological membrane analysed.
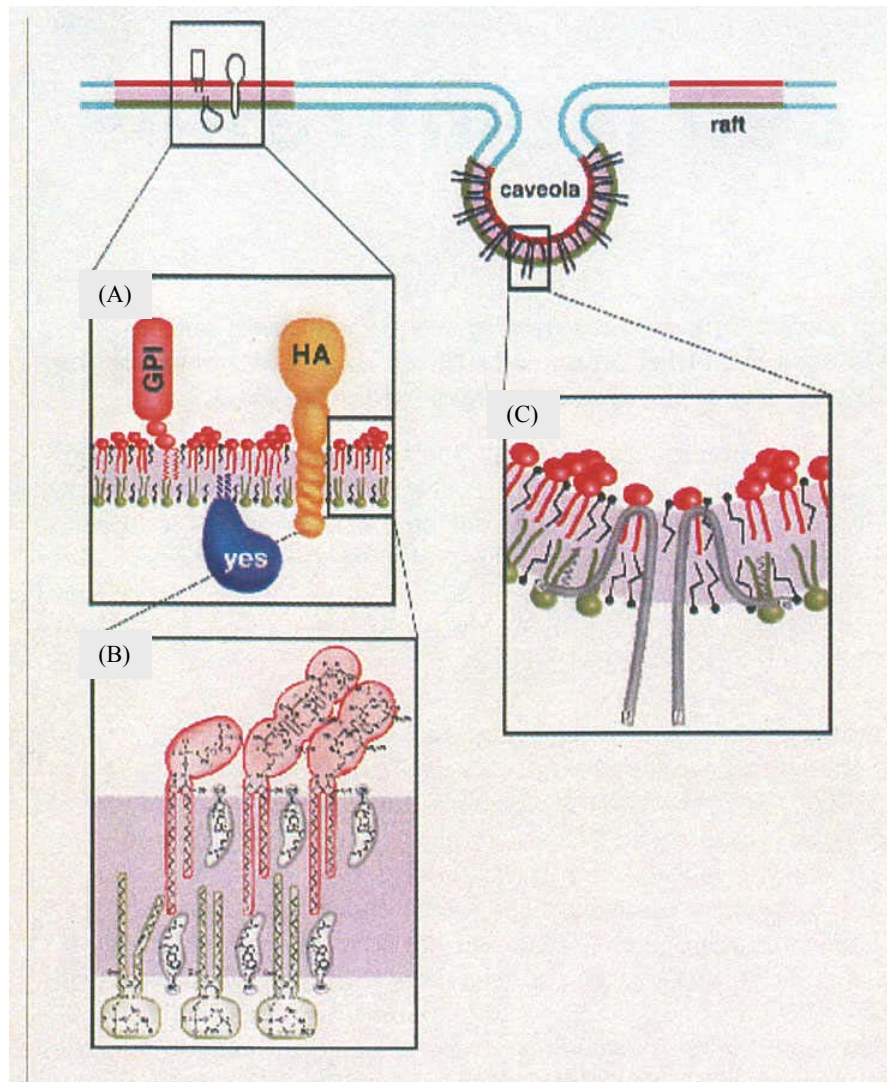
Figure 1.2 Model for the organization of rafts and caveolae in the plasma membrane. The rafts (red) segregate from the other regions (blue) of the bilayer, in which unsaturated phosphatidylcholine is predominantly in the exoplasmic leaflet. (A) Rafts contain proteins attached to the exoplasmic leaflet of the bilayer. (B) The lipid bilayer in rafts is asymmetric, with sphingomyelin (red) and glycosphingolipids (red) enriched in the exoplasmic leaflet and glycerolipids (green) in the cytoplasmic leaflet. Cholesterol (grey) is to be seen in both leaflets. (C) Caveolae are formed by self-associating caveolin molecules making a hairpin loop in the membrane (SIMONS, 1997).

1.1.2   Lipid phases and microdomains

In simple models, domains are described as phase separation of lipids with different melting temperatures. At low temperatures, the acyl chains of the lipid bilayers are in an ordered chain conformation typical of a gel phase ($P_{\beta'}$). The solid phase is not thought to be of physiological relevance (MUNRO, 2003). Above the melting temperature the conformational order is lost and the lipids form a liquid-crystalline phase (L_α). The presence of cholesterol in a system can

change the phase behaviour drastically. The cholesterol molecule interacts differently with the degrees of freedom of the lipid acyl chains. At low concentrations, it does not prefer one of the lipid phases to the other. However, at higher concentrations ($\geq$ 25%) cholesterol causes chain order in the liquid phase and breaks the crystallinity of the solid phase. The result is the formation of a new phase: the liquid-ordered phase, which is a liquid from the point of view of the translational degrees of freedom (lateral diffusion), but otherwise rigid from the point of view of the acyl chain order (MOURITSEN, 1991). The theory has led to the following terminology for the various phases of the lipid/cholesterol mixtures. The gel phase is denoted by s_o, the indices "s" standing for solid in two dimensions and "o" for orientationally ordered chains, the liquid-crystalline phase l_d by the indices "l" for two-dimensional liquid and "d" for disordered chains and, finally, the new liquid ordered phase is denoted by l_o (Figure 1.3). An important property of the l_o phase is the enormous increase in mechanical strength over the l_d phase (NEEDHAM, 1990), which must be partly due to the increased importance of the van der Waals interaction for the ordered chains in the lipid molecule. This phenomenon in combination with increased bilayer thickness reduces membrane permeability greatly (BLOOM, 1991). It is supposed that the l_o is a "biologically relevant" phase (LIPOWSKY, 1995).

In the plasma membrane a high level of cholesterol is present, therefore it is important to consider how cholesterol affects the physical properties of lipid bilayers. Studies, carried out on bilayer containing different cholesterol concentrations, indicated that the l_o and l_d states could be relevant to the question of lipid microdomains. The cholesterol-rich l_o and cholesterol-poor l_d phases coexist within a single bilayer; increasing cholesterol level induces a continuous l_o phase. Generally, lipids that contain exclusively saturated acyl chains promote the formation of l_o phase because of their capacity to pack more readily against cholesterol. This feature is much more prevalent in sphingolipids because of their ability to form intermolecular hydrogen bonds (LI, 2001; RAMSTEDT, 2002).

gel   liquid disordered (l_d)   liquid ordered (l_o)
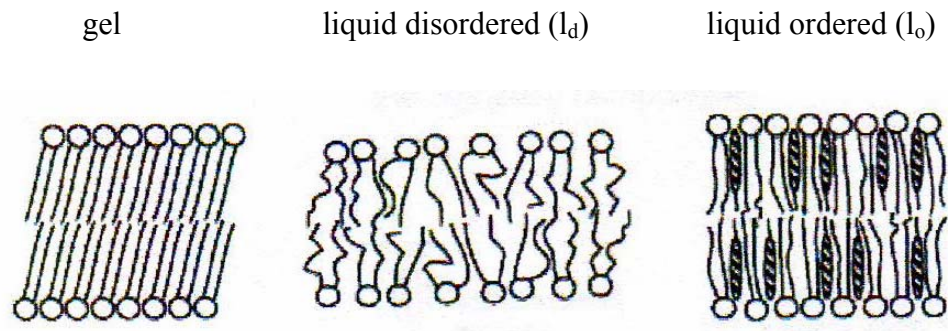
Figure 1.3 Membrane phases of the lipids of the plasma membranes. The gel phase melts above T_m to form a fluid phase (liquid-disordered (l_d), sometimes referred to as "liquid-crystalline"). The presence of cholesterol (hatched ovals) forms an intermediate phase between gel and l_d, for which the term liquid-ordered (l_o) was coined (MUNRO, 2003).

1.1.3   Artificial membranes as model systems

The discovery that artificial raft lipid mixtures which mimic the composition of detergent-resistant membranes were partially resistant to detergent and showed spectroscopic evidence for a more ordered (raft) phase coexisting with a disordered phase in the plane of the membrane (AHMED, 1997; SCHROEDER, 1994; DIETRICH, 2001), opened up the possibility to study model membrane systems. In particular, to measure their properties, which could resemble features typical of natural membrane raft domains. To work with model systems has many advantages, for example, domains can be directly observed with different spectroscopic methods, miscibility and transition temperatures can be measured, and liquid phases can be studied from a more controlled physical perspective than in cells (VEATCH, 2003). Since artificial lipid mixtures can be prepared without proteins, it is possible to study the pure lipid contribution to membrane phase separation. The subsequent addition of a protein to the system will lead to additional changes due to possible lipid-protein interactions. However, a number of issues need to be considered when properties of model membrane systems are compared to living cells. Lipid model systems are simplified models, often consisting of two or three homogeneous lipids, at non physiological temperature and sometimes in monolayer, where the lateral pressure may be less than in a bilayer. Biological bilayers, on the contrary, have acyl chains with great heterogeneity in their length and saturation and also contain a large number of different integral proteins. Another important point is that many studies on

domains in model membranes rely on using different methods to detect phase transitions as temperature is altered.

1.1.4   Lipid monolayer

The monolayer, being half of a membrane, is a well-defined planar system to study intermolecular interactions between lipids and also between lipids and proteins.

When spread on an air-water interface, water insoluble amphiphilic molecules, like long-chain fatty acids and phospholipids, form mono-molecular layers called Langmuir films. These systems are quasi-bidimensional and macroscopic because usually they are formed by at least 10-15 molecules. Monolayers are studied because they represent phases with varied forms of order, similar to the order in smectic liquid crystals. The amphiphilic nature of the surfactants dictates the orientation of the molecules at the interface (air/water or oil/water) in such a way that the polar head group is immersed in the water and the long hydrocarbon chain is pointing towards air, gas or oil.
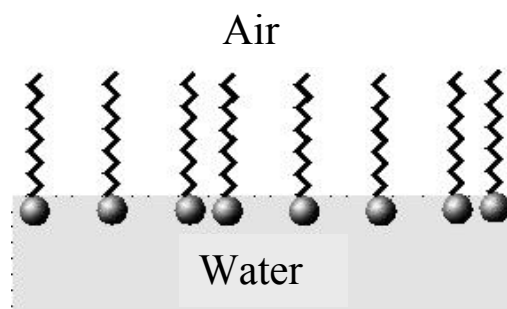
Figure 1.4 A schematic illustration showing a spread monolayer at the air/water interface.

The remarkable observation made by Langmuir was that monomolecular films can be compressed, using a simple film balance, to form two-dimensional versions of the well-known states of matter in three dimensions. For the two dimensional phases, film area (A) and two dimensional film pressure (Π) play the roles volume and hydrostatic pressure play in three dimensions. Π is given by the following relationship:

$$\Pi = \gamma - \gamma_0 \qquad\qquad (1.1)$$

where γ is the interfacial tension and γ_0 the surface tension of pure water. Figure 1.5 shows the resulting isotherm. The two horizontal portions on the isotherm signal two phase transitions, one from a gas phase to a liquid phase and one from a liquid phase to a solid phase.
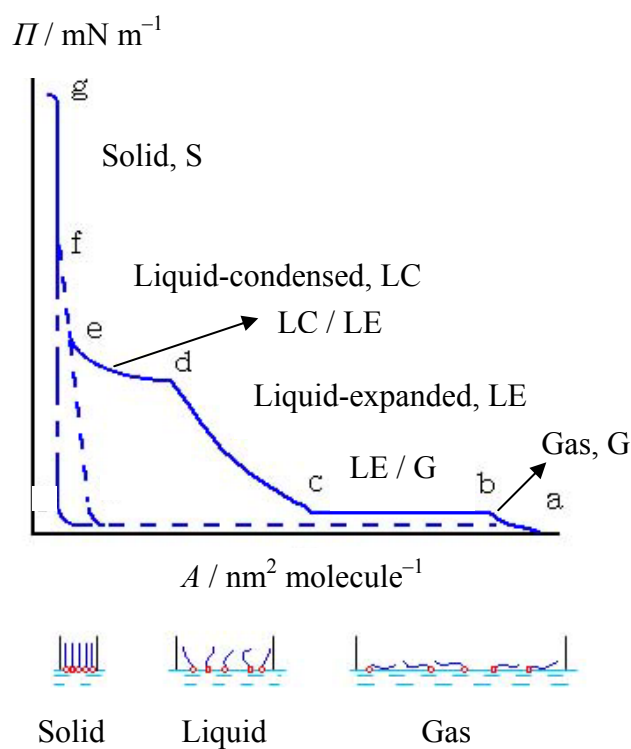
Figure 1.5 At the top: schematic illustration of an isotherm that provides the relationship between A and Π. At the bottom: orientation of the molecules in different phases.

Characteristics of the monolayer of an amphiphilic material are obtained by measuring the surface pressure as a function of the area of water surface available to each molecule. This is carried out at constant temperature and is called "isotherm". As shown in Figure 1.5, at the top, several phases appear. Generally, adsorption of fatty acids at the water interface leads to

three distinct regions: gas (G), liquid (L) and solid (S), whereas phospholipids possess an additional, almost horizontal transition phase (LE/LC) between two different liquid phases: liquid-expanded (LE) and liquid-condensed (LC). The position of this intermediate phase is very temperature dependent.

1.1.5   Giant unilamellar vesicles (GUVs)

Vesicular self-assembly produces closed species with an internal water core. There is a geometrical analogy here with the living cell, and in fact liposomes have been viewed for a long time as precursors of the protocell. The most obvious advantage of giant vesicles with respect to conventional ones, is that they can be observed by optical methods as an individual macromolecular entity. However, working with individual species needs an approach different from working with statistics of large numbers. In fact, each individual often tends to behave differently – one giant vesicle is large, another is smaller, one is stable to rupture, the other is not. Such individuality, generally, means a deviation from reproducibility and it might represent a problem. Events contemplated with one giant vesicle are sometimes not easily observed again.

1.1.6   Morphology of vesicles

Biomembranes exhibit a rather complex morphology. The surfaces formed by intracellular organelles often have a very complicated topology, such as those of the endoplasmatic reticulum (ER) or the Golgi apparatus. Trafficking from the ER to the plasma membrane is effected on a molecular and a mesoscopic level. In general, the former holds for small molecules and ions and is mediated by pumps and co-transporters. The second route occurs via vesicles and is associated with local membrane instabilities in the course of a vesicle budding→fission→fusion chain of events. Likewise, the plasma membrane can develop small buds as in exo- or endocytosis, microvilli, i.e. finger-like protusions, and pseudopods. Dynamic shape transformations are also used in cell locomotion. Some aspects of these morphological transformations can be experimentally studied with lipid vesicles like giant unilamellar vesicles (GUVs). In general, to study membrane topological behaviour, GUVs are objects of great interest both for their cell dimensions and for the possibility to observe them directly under the microscope (BAGATOLLI, 1999). Moreover, it is possible to study mechanical properties of the membrane through the calculation of elementary deformation parameters. For example, Käs and Sackmann studied the shape transitions induced by area-to-

volume changes of GUVs formed by synthetic phospholipids in the liquid crystalline state, using optical microscopy (KÄS, 1991). Morphological changes induced by temperature were found in lipid vesicles formed by bovine brain sphingomyelins (DÖBEREINER, 1993), showing how the intrinsic physical properties of the lipid membrane can play an important role in the naturally occurring budding and fission processes of the cell membranes.

The current theoretical understanding of the morphology and morphology transformations of vesicles is based on the important notion of bending elasticity introduced some twenty years ago, but performed only recently (SVETINA, 1989; BERNDL, 1990; MIAO, 1991; SEIFERT, 1991). These studies revealed a large variety of shapes, which minimize the energy for certain physical parameters such as enclosed volume and the area of the vesicle. An increase in temperature transforms a quasi-spherical vesicle via thermal expansion of the bilayer to a prolate shape and then to a pear. Finally, a small bud is expelled from the vesicle. Usually, the buds remain connected to the mother vesicle via narrow constrictions or necks. Another shape transformation, the discocyte-stomatocyte transition, is shown in Figure 1.6. This transition resembles a shape transformation which can be induced in red-blood cells by depletion of cholesterol. Budding and fission have also been observed in vesicles consisting of lipid mixtures (DÖBEREINER, 1993). For example, if two components form domains, the line energy associated with these domain boundaries can be reduced by budding of such a domain (LIPOWSKY, 1992).
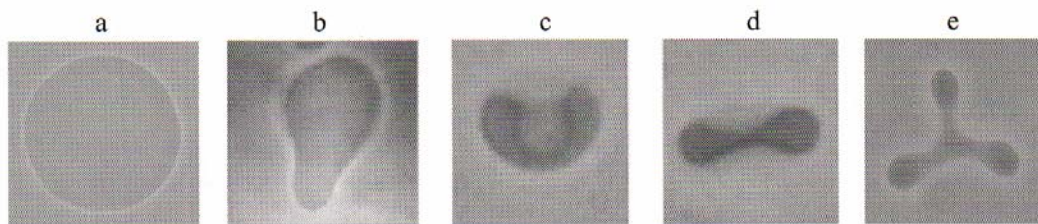
Figure 1.6 Lipid vesicle shapes found experimentally: (a) sphere, (b) pear shape, (c) stomatocyte, (d) discocyte, (e) starfish shape (MOURITSEN, 2005).

Many theoretical approaches to determine membrane conformations, topology, and shapes assume the membrane to be a two-dimensional liquid interface imbedded into a three-dimensional space. The membrane is taken to be in its fluid state. Thus, it does not resist shear forces within the plane of the membrane. Therefore, when the membrane is mechanically deformed, there are only two possible modes of deformation left: bending and stretching/compressing. In this model we can neglect area compressibility, if we assume that

the interface is infinitely thin with no internal structure and its area is fixed; in doing so, bending is left as the sole possibility. Bending induces curvature, and the curvature of the interface at given (arbitrary) internal coordinates is characterized by its two principal radii of curvature R_1 and R_2, which determine the mean curvature H and the Gaussian curvature K of the membrane surface, which are defined as:

$$H \equiv \frac{\left(\dfrac{1}{R_1} + \dfrac{1}{R_2}\right)}{2} \tag{1.2}$$

and

$$K \equiv \frac{1}{R_1 R_2}. \tag{1.3}$$

Surfaces with $H = 0$ everywhere are called minimal surfaces.

The general expression for the differential elastic bending energy, dE_{surface}, that is required for deforming an element of area dA to a shape which is described by R_1 and R_2 (Figure 1.7) is given by:

$$dE_{\text{surface}} = \left[\frac{k}{2} \left(\frac{1}{R_1} + \frac{1}{R_2} \right)^2 + \frac{k_G}{R_1 R_2} \right] dA. \tag{1.4}$$

Thus the total bending energy for deforming the entire interface called, S, is the sum (i.e., the integral) over all the elements of area (MOURITSEN, 2005):

$$E_{\text{surface}} = \oint_S dE_{\text{surface}} = E_k + E_{k_G} \tag{1.5}$$

k is the normal bending modulus (also called the mean curvature bending modulus), k_G is the so-called Gaussian curvature modulus, an additional property of the interface will determine the bending energy and hence the shape of the interface.
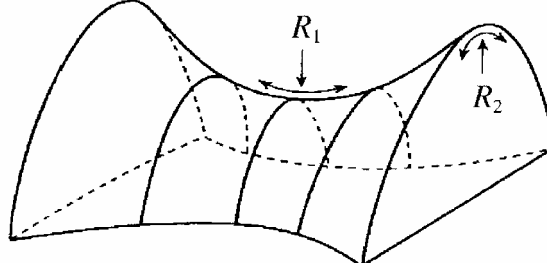
Figure 1.7 The two principle radii of curvature describ the local curvature of a mathematical interface (MOURITSEN, 2005).

The Gaussian curvature modulus, k_G, controls the topological complexity of the interface. The Gauss-Bonnet theorem shows that for a closed interface, the contribution of the Gaussian curvature to the energy of the interface is proportional to a topological invariant, $4\pi(1-g)$:

$$E_{k_G} = k_G \oint_S \frac{1}{R_1 R_2}\, \mathrm{d}A = k_G 4\pi(1-g) \tag{1.6}$$

g is the so-called genus number, which describes the topology of the closed interface (Figure 1.8). For a sphere, $g = 0$. More complex surfaces with holes have higher values of g. The value of the Gaussian curvature modulus is difficult to determine experimentally; k_G is generally believed to be of the same order of magnitude as the mean curvature modulus, k.
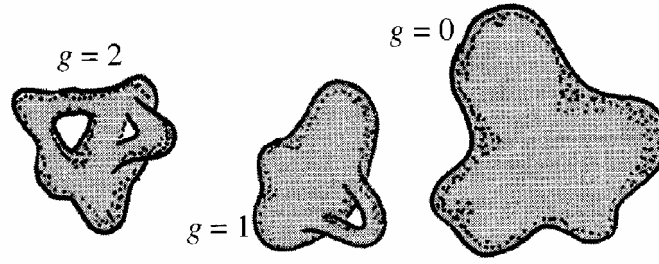
Figure 1.8 Closed interfaces of different topology characterized by different values of the genus number g (MOURITSEN, 2005).

The lipid membrane to form a vesicle initially needs to compress or stretch the relaxed area of the inner monolayer, A_0^{inner}, and of the outer monolayer, A_0^{outer}, to produce a closed vesicle. Thus the fixed mean area is:

$$A = \frac{1}{2}\left(A^{inner} + A^{outer}\right) = \frac{1}{2}\left(A_0^{inner} + A_0^{outer}\right) \tag{1.7}$$

This implies that although the mean area is fixed, there can be a deviation in the differential area, $\Delta A = A^{inner} - A^{outer}$, from its equilibrium value $\Delta A_0 = A_0^{inner} - A_0^{outer}$. Because of the different stressing of the two monolayers the total energy for the membrane should consider another term, beside the area compressibility modulus, k, and the bilayer thickness, d_L, the Area-Difference-Energy (ADE). The definition is as follows:

$$E_{ADE} = \frac{\alpha \kappa \pi}{2 A d_L^2}\left(\Delta A - \Delta A_0\right)^2. \tag{1.8}$$

Note that in contrast to the spontaneous curvature, the differential area is not an intrinsic property. α is a constant that is close to unity for all phospholipids.

The total bending energy, which will determine the equilibrium shape of a closed lipid vesicle, is given by:

$$E_{\text{total}} = \frac{\kappa}{2} \oint_S \left(\frac{1}{R_1} + \frac{1}{R_2} - \frac{2}{R_0} \right)^2 \, dA + \frac{\alpha \kappa \pi}{2 A d_L^2} (\Delta A - \Delta A_0)^2 \, . \qquad (1.9)$$

The equilibrium shape of a given fluid vesicle is obtained by minimizing E_{total}, and the results are given in form of a phase diagram as shown in Figure 1.9. Note that here the stable phases are given as a function of two reduced parameters: the reduced vesicle volume, $v = V \big/ 4/3 \pi (A/4\pi)^{3/2}$, and a parameter, $\Delta a_0 = \Delta A_0 \big/ (16 \pi R_0 d_L)$, which is a combination of spontaneous curvature and preferred differential area. To solve equation (1.9) geometrical and mechanical parameters of the vesicles, the volume V and area A, and the spontaneous curvature R_0^{-1} and the preferred differential area ΔA_0 are needed as input parameters.

Experimentally, changes of vesicle shapes are observed by varying temperature or pressure, adding various amphiphiles or adsorbents, by mechanical, electrical or magnetic treatments, or by adhesion (LUISI, 2000; KÄS, 1991). Temperature changes induce area/volume differences due to the different expansion coefficients of lipid and water, as well as due to the two- and three-dimensional response of the system to external stress, respectively. Budding, discocyte-stomatocyte, dumbbell-pear, and spontaneous tether formation transitions have been observed in lecithin GUVs (KÄS, 1991; SACKMANN, 1986). Beney *et al*. observed shape changes of GUV upon decompression of egg lecithin vesicles. Because water was pushed out during the compression, being lecithin more compressible than water, budding off was observed due to the excess of surface area upon quick decompression. The compressibility of cholesterol-containing bilayers is smaller and no shape changes were observed (BENEY, 1997). Moreover, upon the creation of a pH gradient across the membrane of giant vesicles containing acidic lipids, shape changes were observed. The gradient caused flip-flop of acidic lipids producing dramatic shape changes (FARGE, 1992). Such observations may have biological relevance, because it is already known that flip-flop reorientations occur from the inner to the outer monolayer in cell apoptosis and senescence of red blood cells. Shape transformations are also predicted to arise in vesicles consisting of bilayers with different components due to different mechanism (BAUMGART, 2005). If, for example, two components form domains, the line energy associated with these domain boundaries can be reduced by budding of such a domain. Furthermore, even if the membrane is in a one-phase region, a temperature induced budding process may lead to a curvature-induced phase

segregation since, in general, the two components couple differently to the local curvatures (SEIFERT, 1993). So far, many of these effects are not yet verified experimentally even though budding and fission have been observed in vesicles consisting of lipid mixtures.
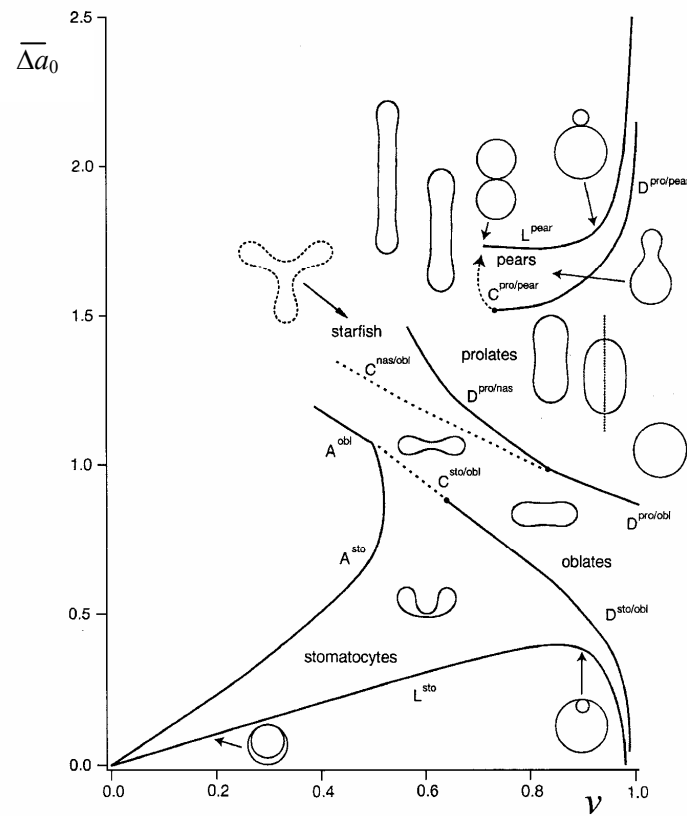
Figure 1.9 Phase diagram for closed vesicle membranes. The names of several of the shapes refer to the shapes that have been found for red blood cells (MOURITSEN, 2005).

1.2   Membranes and signal transduction

While the basic structure of biological membranes is determined by the lipid bilayer, their specific functions are carried out largely by proteins. Many membrane proteins, because of their position between a cell and its neighbours and the external environment, serve as primary mediators of the signals which regulate the activity of the cell. Membrane proteins are divided into two classes: intrinsic and extrinsic (SINGER, 1972). The first ones are inserted to varying degrees into the hydrophobic core of the lipid bilayer. The extrinsic on the other hand associate noncovalently with the surface of membranes, and do not penetrate the lipid bilayer. A third class of membrane-associated proteins links to the membrane through covalent attachment to either a fatty acid or a glycolipid headgroup (SEFTON, 1987). Like intrinsic membrane proteins, removal of these proteins from the lipid bilayer may require the use of detergents. However, as these proteins do not penetrate the lipid bilayer, they are best thought of as extrinsic membrane proteins.

1.2.1   Anchor proteins

Many extrinsic membrane proteins insert into the membrane structure through co- or post-translational lipid anchor. For example, glycosylphosphatidylinositol (GPI) belongs to a family of secreted signalling molecules. In the endoplasmic reticulum (ER), the C-terminus of a new protein, composed of hydrophobic amino acids, is cleaved off and replaced by the GPI-anchor. The protein then processes through the secretory route, it is transferred to the Golgi and finally attached to the exterior leaflet of the cell membrane (SHAROM, 2002).

The function of the steroid cholesterol as lipid anchor was discovered in connection with the *Hedgehog*-family. The *Hedgehog* (*Hh*) gene family encodes a group of secreted signalling molecules that are essential for growth and patterning of many different body parts of vertebrate and invertebrate embryos (PORTER, 1996). A precursor of the *Hh* cleavages autocatalytically into a new C-terminus, which will be modified through an ester-bond with the cholesterol.

Proteins with an N-myristoylated group, like the Src-kinase, have a myristoyl acid anchor at the N-terminal glycine. This saturated C_{14}-chain is fixed co-translationally through an amid-bond by an N-myristoyltransferase (JOHNSON, 1994).

Instead, proteins with a palmitoyl group bind to cystein-residuals with a saturated C_{16}-chain post-translationally via a thioesterbond. (RESH, 1999). The hydrolysis and the formation

of the thioesterbond are important to regulate the modified state of the cell, but also to localise and to adjust the activity of the protein.

At or near the C-terminus prenyl proteins have 1-2 isopren modifications. The formation of a stable thioether bond between a cystein residual and C_{15}-farnesyl, C_{20}-geranyl-geranyl-isopren body, respectively, is catalysed by specific isoprentransferases. The sequence of the C-terminus is crucial to identify the different transferases (SINENSKY, 2000). Figure 1.10 shows some examples of lipid modifications of anchor proteins.
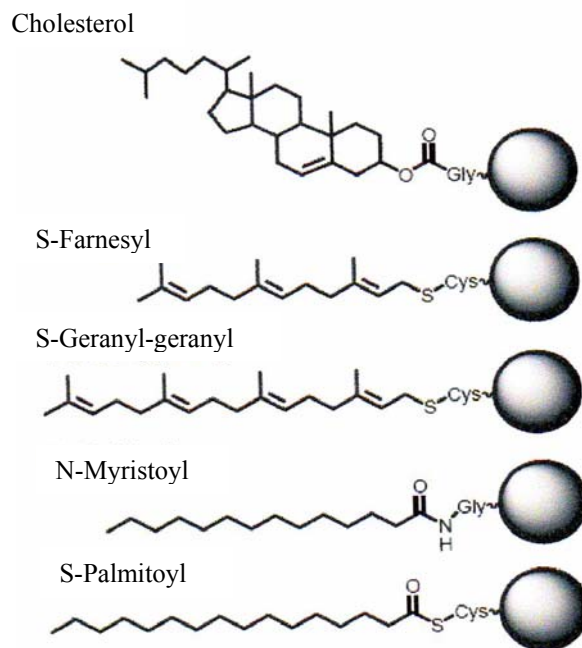
Figure 1.10 Examples of lipid modifications of anchor proteins (KAHMS, 2004).

1.2.2   Submembrane localisation

The lipid anchors probably play a crucial role in the localisation of the proteins in the plasma membrane. It was postulated, for example, that many GPI-anchor proteins are located in lipid rafts (HOOPER, 1999). Likewise, many transmembrane proteins, because of their amino acids next to the transmembrane helix, as well as proteins modified through a cholesterol anchor, like for example the Hedgehog proteins (RIETVELD, 1999), and proteins with a myristoyl and/or palmytoyl anchor, are found to bind preferentially to the more ordered parts of the plasma membrane. The latter phenomenon might be explained in terms of energies. Saturated lipid anchors which bind in the thicker packed lipid rafts are energetically favoured (SIMONS,

2001), compared to prenyl proteins which possess a farnesyl or geranyl-geranyl residue and are detected outside the rafts microdomains (MELKONIAN, 1999, ZACHARIAS, 2002). That is due to protein-protein interactions, which might influence submembran localisation. Examples are Src-Kinases Fyn (WARY, 1998) and eNO-Synthase (FERON, 1996), which interact directly with the protein caveolin, and other proteins like isoform of the GTPase Ras as discussed in the next paragraphs.

1.3   Ras protein

Ras proteins are low-molecular-weight GTPases that serve as GDP/GTP-regulated relay switches. They control signal-transduction cascades which are initiated by diverse extracellular stimuli active cell-surface receptors. Ras are members of the Ras superfamily as well as the Rho-family (MACKAY, 1998), which take part in the organisation of the cytoskeleton, the Rab- and Arf-proteins responsible for the vesicular transport, the Ran protein for the nuclear transport (MOORE, 1998) and the Rag-, Rheb- and Rit-proteins. The role of the last family is still unknown.

Ras protein function is regulated by its association with the guanine nucleotides guanosine triphosphate (GTP) and guanosine diphosphate (GDP). Ras functions as a binary molecular switch that cycles between an active GTP-bound and an inactive GDP-bound state (Figure 1.11). Ras possesses an intrinsic GTPase activity catalyzing the hydrolysis of the bound GTP to GDP and an intrinsic GDP/GTP exchange activity to cycle back to the active state. These activities, however, are too low to allow Ras proteins to be rapidly controlled in their GDP/GTP cycling. Instead, GDP/GTP cycling is controlled by guanine nucleotide exchange factors (GEFs; Sos1/2, RasGRF1/2 and RasGRP) acting as positive regulators to promote the formation of Ras-GTP and GTPase activating proteins (GAPs; p120 GAP and neurofibromatosis type 1 protein, NF1) acting as negative regulators to cycle Ras back to its inactivate GDP-bound state.
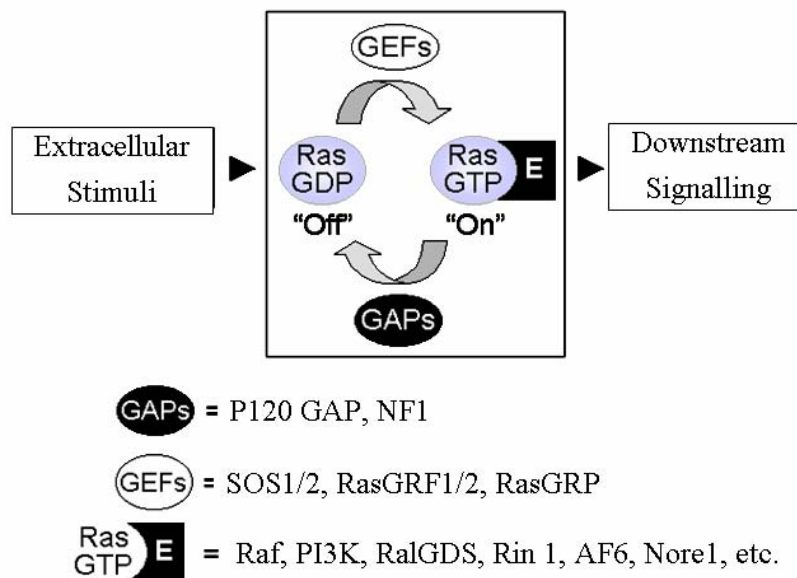
Figure 1.11 Switch function of Ras proteins. Guanine nucleotide exchange factors (GEFs) catalyse the nucleotide exchange from GDP to GTP. Ras-GDP binds effector proteins and starts the signalling cascade. Ras proteins will then be inactivated by GTPase-activating proteins (GAPs), which catalyse the hydrolyses from GTP to GDP releasing a phosphate.

1.3.1   Ras isoforms

The ras genes were discovered initially as the genes responsible for the potent cancer-causing activity of the Harvey and Kirsten murine sarcoma viruses (Ha-MSV and Ki-MSV) (MOLUMBRES, 2002).

Three human ras genes were found to encode four different Ras proteins: H(arvey)-Ras, K(irsten)-Ras4B and N(euroblastome)-Ras, whereas K(irsten)-Ras4A and K(irsten)-Ras4B are encoded from the same gene by use of alternative fourth exons that differ only in their carboxyl-terminal 25 amino acids. H-Ras, N-Ras and K-Ras4A exhibit 189 amino acids, K-Ras4B only 188 and they are all approximately 21 kilodaltons in size. The amino terminal 84 residues are identical among the four Ras proteins (Figure 1.12). The significance of sequence identity in this region is highlighted by the fact that it includes the effector domain (residues 25 to 45), as well as the switch I (residues 30 to 38) and II (residues 59 to 76) regions. The effector domain is involved in the binding of activated Ras with its downstream effector targets. Identity among effector domains and flanking sequences suggests that the different Ras proteins are capable of binding to and/or activating the same targets. The next 80 residues of the four Ras proteins also share strong sequence identity (85%). However, the

carboxyl terminal 25 residues of Ras proteins are highly variable (4% identity) and therefore comprise the "hypervariable" region. In concert with posttranslational modifications signalled by the carboxyl terminal CAAX tetrapeptide motif (where C = cysteine, A = aliphatic amino acid, and X = methionine or serine), the hypervariable region contains sequence determinants that specify Ras protein association with the inner surface of the plasma membrane.
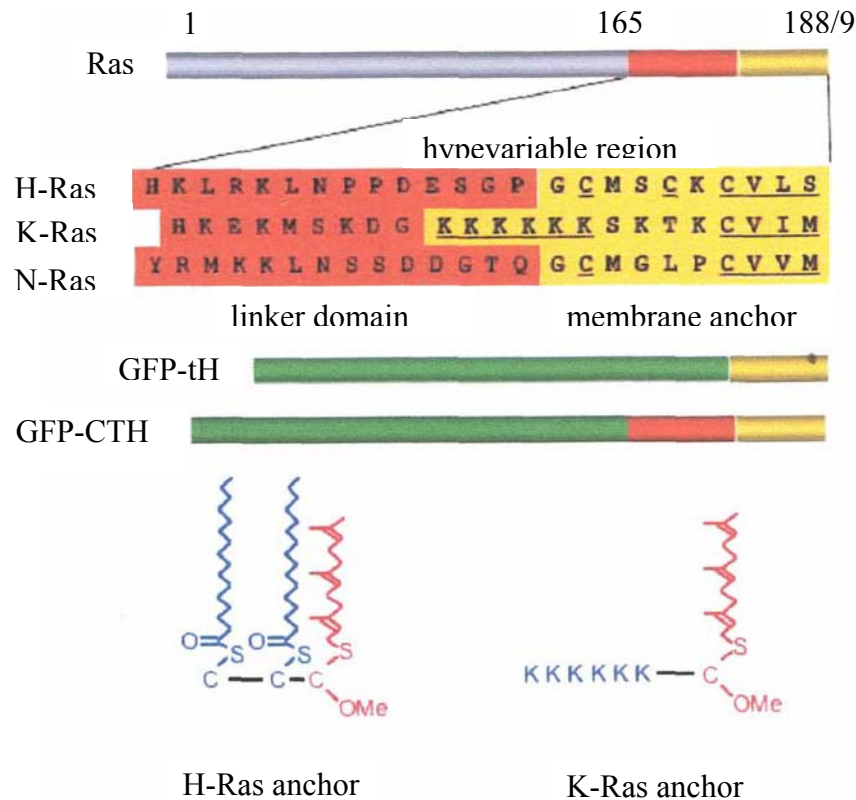
Figure 1.12 The N-terminal 165 amino acids of H-, K- and N-Ras (grey) are highly conserved and mediate all of the protein interactions with effectors and exchange factors. In contrast the C-terminal 24-25 amino acids of the hypervariable region (HVR) diverge significantly. The HVR encodes for sequences that direct attachment of the C-terminal membrane anchor (yellow). The C-terminal CAAX motif is farnesylated, the AAX amino acids removed and the now C-terminal cysteine is methylated. H- and N- Ras are then palmitoylated. The structure of the mature anchor of H- and K-Ras is shown (that of N-Ras is comparable to H-Ras but with a single palmitate). The adjacent protein sequence of the linker domain (orange) modulates the microdomain interactions of H-Ras. As example, the structure of fusion proteins like green fluorescent proteins (GFP)-tH (GFP with the minimal H-Ras membrane anchor) and GFP-CTH (GFP with the complete H-Ras HVR) are also shown.

In quiescent, no dividing cells, Ras is found predominantly in the GDP-bound form (more than 95%). Following an extracellular growth stimulus, GDP/GTP exchange induces a rapid and transient cycling to the GTP-bound state. GDP/GTP cycling causes a change in the

structural conformation of Ras, corresponding to the switch I and II regions, that greatly increases its binding affinity for downstream cytoplasmic effector targets, thus initiating various signalling pathways. Upon hydrolysis to GDP, the activated effector protein dissociates from the GTPase, and the relay of the signal is terminated. In tumors, mutated ras genes encode Ras proteins with single amino acid substitutions at positions 12, 13 or 61. These mutated Ras proteins are insensitive to the negative regulation of GAPs and therefore are constitutively GTP-bound and activated in a stimulus-independent fashion. Consequently, the Ras signalling pathway is under persistent stimulation and this is a primary mechanism that causes activated Ras to contribute to cell proliferation.

1.3.2   Membrane localisation of Ras proteins

The post-translational modifications of the Ras proteins mediate the position of the proteins in the cell membrane structure. In 1983 the presence of Ras proteins in the plasma membrane was proved immunocytochemically through electron microscopy (WILLINGHAM, 1983). It was evidenced, using immuno detection of Ras proteins in cellular membrane fraction and immunofluorescence detection in cells that to localise Ras proteins in the membrane it was necessary in addition to a farnesyl group another one (HANCOCK, 1990). In these studies it was found that H-Ras needed a palmitoylated group for its subcellular localisation, whereas K-Ras, which is not palmitoylated, had another novel plasma membrane targeting signal consisting of a polybasic domain also acting in combination with the CAAX motif. Apparently, K-Ras is stabilized through the interactions between the positively charged lysine and the negatively charged phospholipids of the plasma membrane (GOMASHCHI, 1995). Moreover, for the first time, in studies with green fluorescent protein (GFP)-tagged N-Ras the presence of Ras protein in living cells was demonstrated. In addition, these experiments have shown that the CAAX motif alone targets proteins to the endomembrane system, whereas for the localisation in the plasma membrane, a palmitoylation for the H- and N-Ras isoforms or a polybasic domain for the K-Ras (CHOY, 1999) is necessary.

1.3.3   Ras isoforms and their localisation in the plasma membrane

An interesting issue that follows from the above observations is that palmitoylated- and polybasic-targeted Ras proteins may be directed to different subdomains of the plasma membrane. The biological differences between the Ras isoforms might be detected by their localisation in the different sites in the plasma membrane. In support of this idea it has been

reported that signalling through palmitoylated H-Ras, but not through polybasic K-Ras, is highly sensitive to perturbations of the cholesterol level of the plasma membrane (ROY, 1999). H-Ras function is therefore selectively dependent on the integrity of cholesterol-rich domains or lipid rafts, but the actual site of attachment of Ras proteins to the plasma membrane has not yet been elucidated. In their studies, Prior *et al*. reveal a dependence between the activation state of H-Ras and its membrane localisation. In this case it was postulated that when H-Ras is GDP-bound it is still in the lipid rafts, while the effect of GTP loading is to increase the residence time of H-Ras in the disordered regions of the plasma membrane (PRIOR, 2001). In FRAP (fluorescence recovery after photobleaching) experiments it was shown that H-Ras unlike K-Ras is localised in rafts microdomains, whereas the active mutants H-RasG12V and K-RasG12V exhibit concentration-dependent interactions with saturable nonrafts sites or domains (NIV, 2002). Lommerse *et al*. studied, using single molecule fluorescence microscopy, trajectories of individual H-Ras with C-terminus fused to an enhanced yellow fluorescent protein, diffusing in the cytoplasmic leaflet of the plasma membrane in live cells. The results indicate that the diffusion of 30-40% of the molecules is constrained in domains of a typical size of 200 nm. However, extraction with cholesterol or actin did not change the domain characteristics significantly, demonstrating that these kinds of domains are different from the supposed rafts (LOMMERSE, 2004).

To explicate this intriguing field of biology, many experiments using numerous techniques were also done *in vitro*, using model membranes. For example, in giant unilamellar vesicles, the effects of a fluorescent peptide containing a farnesyl (Far) and palmitoyl (Pal) anchor, Bodipy-Gly-Cys(Pal)-Met-Gly-Leu-Pro-Cys(Far)-OMe, which represents a membrane recognition model system for Ras proteins were studied. For this study a binary phospholipid mixture consisting of DMPC (dimyristoyl-phosphatidylcholine)/DSPC (distearoyl-phosphatidylcholine) and varying levels of cholesterol was chosen. Here it was shown that the peptide preferentially binds to the fluid phase of the binary lipid mixture DMPC/DSPC and that the addition of cholesterol leads the peptide to induce new fluid domains, i.e. the lipid matrix is conformationally ordered (JANOSCH, 2004). Experiments are also carried out on a doubly lipid modified (farnesyl and hexadecyl) heptapeptide of the C-terminus of the human N-Ras protein in a DMPC-(dimyristoylphosphatidylcholine) matrix using FTIR, NMR and neutron diffraction. With these unpolar lipid anchors, the peptide gains substantially in hydrophobicity, providing the driving force for membrane insertion. Moreover, in agreement with this model peptide chain insertion, the peptide part is localized at the lipid-water interface of the membrane (HUSTER, 2003).

1.4   Aims of the thesis

Lipids and proteins in mammalian cell membranes are often organized into microdomains. It is now also clear that such domains can exist in simple model membranes. One of the primary goals of this work is to study the lateral organization of three typical components of raft mixtures, such as sphingomyelin, DOPC or POPC and cholesterol, their heterogeneity and phase segregation originating from compositional fluctuations in dependence of different cholesterol concentrations, temperature (from ~2 up to 66 °C) and pressure (from 1 up to 9000 bar). To obtain a valid description over a large length scale down to the biologically relevant range of several tens of nanometres, different methods were applied, such as infrared spectroscopy, small-angle x-ray and neutron scattering, as well as fluorescence microscopy. Infrared spectral parameters, particularly the frequencies, widths, intensities, shapes and splitting of the infrared bands, are very sensitive to the structural and dynamical properties of membrane lipid molecules. The small-angle x-ray scattering technique was applied to determine the structure of the lipid bilayer systems while the small-angle neutron scattering is useful to detect lipid composition fluctuations on a length scale from 1-200 nm. The study of giant unilamellar vesicles is a relatively new approach, which allows direct microscopic visualization of domains and their topology on the μm scale. This particular feature was also utilized in the second part of this work. The purpose was in this case to visualize local and morphological changes on the membrane composed of DOPC/SM/Chol (33:33:33) or DOPC/DPPC/Chol (34.5:34.5:31) as well as the fluid mixture POPC/DLPC (50:50) due to high pressure perturbation. In this way, lipid-lipid interactions are studied without changes in thermal energy, and changes in bending rigidity and line tension of GUVs are observed. Budding and fission of small daughter vesicles are also detected.

In the third part of this thesis protein/membrane interactions are studied in GUVs and in monolayers. Firstly, two-photon fluorescence microscopy on giant unilamellar vesicles is applied to follow the insertion of a fluorescently Bodipy labelled and completely lipidated (hexadecylated and farnesylated) N-Ras protein into heterogeneous lipid bilayer systems. The bilayers consist of the canonical raft mixture POPC, sphingomyelin, and cholesterol, which - depending on the concentration of the constituents - separates into liquid-disordered (l_d), liquid-ordered (l_o), and solid-ordered (s_o) phases. Secondly, the insertion of N-Ras proteins with different lipidation patterns (farnesylated and hexadecylated N-Ras and doubly hexadecylated N-Ras protein) into Langmuir monolayers of a mixture of POPC, sphingomyelin and cholesterol is studied. The shapes of the amide I band were detected using infrared reflection absorption spectroscopy (IRRAS). Significant differences in band contours

were observed due to differences in the orientation of the N-Ras proteins as a consequence of the different lipidation patterns.

The last part deals with the temperature dependent behaviour of the structure of a solvated oligopeptide, GVG(VPGVG), which serves as an elastin-like model system, in various chaotropic and kosmotropic cosolvents by the use of circular dichroism and infrared spectroscopy. The peculiarity of this octamer is to undergo an inverse temperature folding transition, i.e. the folding of this peptide is achieved by increasing the temperature beyond typically 40 °C.

2   Methods and Sample Preparation

2.1   Fluorescence microscopy

Generally, optical microscopy is based on macroscopic properties such as phase gradients, light absorption, and birefringence. In contrast, fluorescence microscopy has the ability of monitoring the distribution of single molecular species based solely on the properties of fluorescence emission. By using intracellular components labelled with specific fluorophores, this method offers the possibility to detect their precise location as well as their associated diffusion coefficients, transport characteristics, and interactions with other biomolecules. In addition, the dramatic response in fluorescence to localize environmental variables enables the investigation of pH, viscosity, refractive index, ionic concentration, membrane potential, and solvent polarity in living cells and tissues.

2.1.1   Two-photon excitation fluorescence microscopy

To obtain 3-D images, the advent of the two-photon scanning technique was an alternative to the confocal laser scanning microscopes. Two-photon fluorescence excitation has many advantages including not only the 3-D resolution without using detection pinholes, but also the unique pro to localize photobleaching and photodamage to a sub-micron region at the focal point and not to the entire sample like in a conventional scanning confocal microscope.

The excitation of chromophores happens not by absorption of a single photon of visible light, but by the simultaneous absorption of two photons, each having half the energy (infrared) needed for the excitation transition (BIRGE, 1986). The two-photon excitation probability is proportional to the square of the excitation power. However, in order to have an appreciable two-photon excitation it is necessary to have a region of a high photon density. The high spatial concentration of photons can be achieved by focusing laser light with a high numerical aperture objective to a diffraction limited spot, whereas a high peak power mode locked laser is indispensable to obtain a high temporal concentration of photons. For a mode locked laser source with average power p_0, repetition rate f_p, pulse width τ_p, and wavelength λ, focused by an objective with numerical aperture A, the number of photon pairs absorbed per laser pulse and per chromophore, n_a, can be estimated as:

$$n_a \approx \frac{p_0^2 \delta}{\tau_p f^2_p} \left(\frac{\pi A^2}{hc\lambda} \right)$$
(2.1)

where c is the speed of light, h is Plank's constant and δ is the two-photon cross section, typical of the order of 10^{-50} to 10^{-49} cm^4 s photon^{-1} molecule^{-1} (KENNEDY, 1986). Fluorescence from the two-photon effect depends on the square of the incident light intensity, which in turn decreases approximately as the square of the distance from the focus. Thus, because of this high nonlinear (~fourth power) behaviour, only those dye molecules very near the focus of the beam are excited and this depth discrimination effect is impossible to achieve with one-photon excitation, whereas in a spatially uniform fluorescent sample equal fluorescence intensities are aided from each z-section above and below the focal plane. In contrast, in the two-photon case and for objectives with a numerical aperture of 1.25, over 80% of the total fluorescence intensity comes from a 1 μm thick region around the focal point. The spatial resolution in the two-photon is reduced in comparison with that obtained from one-photon excitation fluorescence microscopy and that is due to the larger diffraction limited spot of the longer wavelength two-photon excitation source (double the wavelength of the one photon source).

2.1.2   Instrumentation

The two-photon excitation microscope experiments were conducted at the Laboratory of Fluorescence Dynamics at the Physics Department at the University of Illinois in Urbana-Champaign. Figure 2.1 shows the scheme of the two-photon time resolved microscope. The laser light source consists of a mode locked titanium sapphire (Ti: Sapphire) laser (Mira 900, Coherent Inc., Palo Alto, CA) pumped by an argon ion laser (Innova 300, Coherent Inc., Santa Clara, CA) or a Verdi diode pumped intracavity doubled Nd:YVO$_4$, vanadate laser (coherent Inc. Santa Clara, CA). The argon ion laser pumps 8 W with multiple wavelengths to achieve an average of 1 W mode locked power between 750 and 850 nm from the Ti:Sapphire laser. The Verdi, on the other hand, pumps 5 W with a single 532 nm line to accomplish a similar Ti:Sapphire output. The high pulse repetition rate is 80 MHz, and the short pulse width 150 fs. In order to perform time resolved measurements both lasers must be phase locked (synchronized).

The beam expanded laser light is directed into the microscope (Zeiss Axiovert 35 inverted microscope) via a galvanometer driven *x-y* scanner (Cambridge Technology, Watertown, MA). The scanner accepts both digital and analogous control signals and diverts the laser light in the microscope and for two-photon imaging. This microscope has two accessible ports: a side port with 20% transmission and a top port with 80% transmission. Usually, a low cost colour-CCD camera (Sony C76258) and a monitor for alignment are installed on the side port. A dichroic beam splitter for two-photon epi-excitation and emission is integrated and on the top port there is a dual-channel splitter for two-colour measurements. In this microscope due to internal reflections, it is not possible to measure the polarization of the emission. Two Hamamatsu HC120 photon counting photomultipliers with interchangeable dichroic beam splitters and emission filters are used. In this microscope, two kinds of objectives were used: an x20-0.4 N.A. objective air for the experiments with the N-Ras protein, and an x63-1.4 N.A. immersion objective for the high pressure experiments with GUVs.
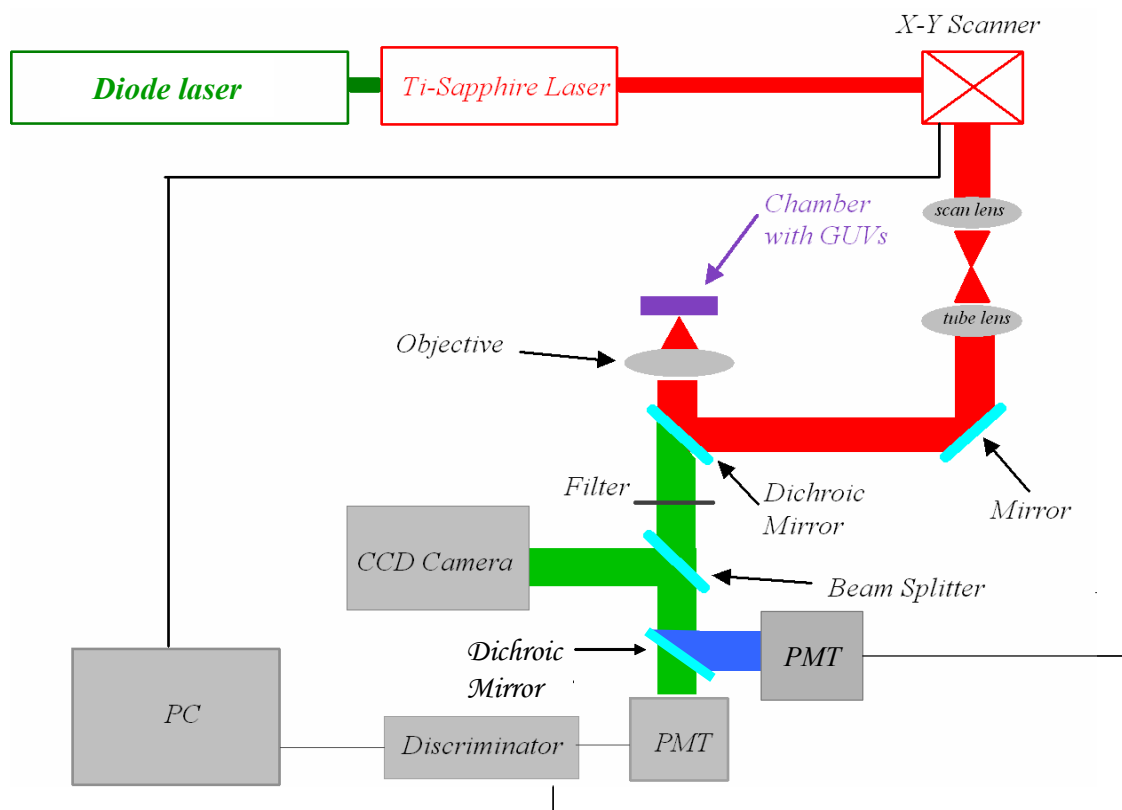
Figure 2.1 Two-photon microscope set-up.

2.1.3   GUVs electroformation method

The set-up to grow GUVs using the electroformation method consists of the electroformation device (chamber) and an external AC or DC supply. The AC supply is a low-frequency generator providing, for example, 0.1-50 Hz up to 7 V. The chamber can have two different geometries (Figure 2.2). Case (A) shows a Teflon chamber with two parallel cylindrical Pt wires. The bottom of the chamber was glued to the casing with 0.5 mm glass plates. The top of the chamber remains open to enable adding of Millipore water and proteins. In a ITO (indium tin oxide) cell, represented in Figure 2.2(B), the electrode consists of thin gold wires glued on a coated glass plate, which will be then stuck on a 1 mm thick coverslip. On the top of the ITO, a support is placed to enable adding of Millipore water. The used chambers are both self made.

The GUVs electroformation protocol consists of three steps: (i) depositing a dry lipid film on the electrode surface; (ii) filling the chamber with water or aqueous solution and applying an external electrical field for ~90 min at the temperature in which all the lipids are in the fluid phase.

(A)

(B)
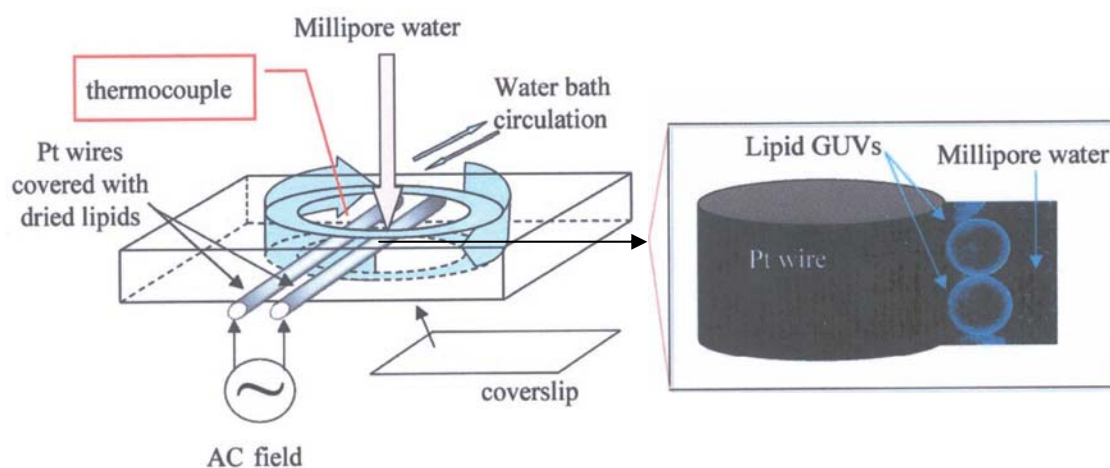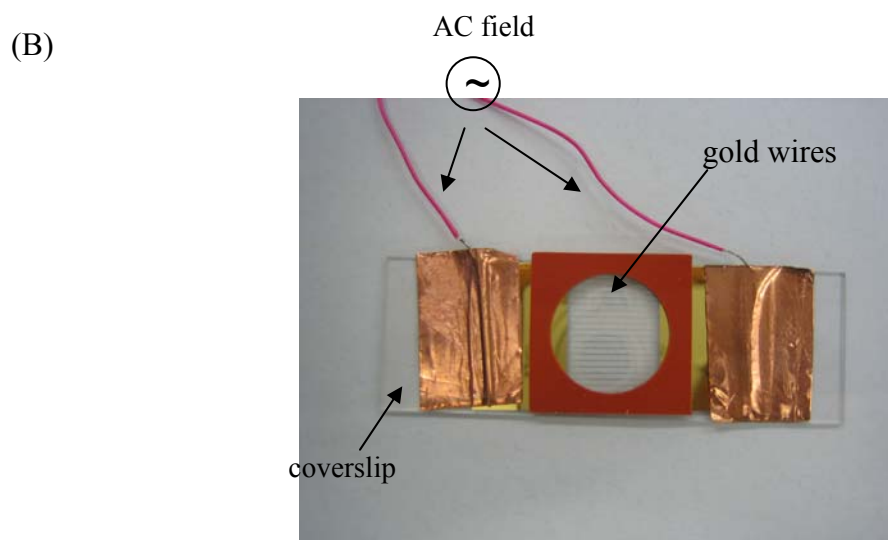
Figure 2.2 (A) Teflon chamber with two parallel cylindrical Pt wires. The bottom of the chamber was glued to the casing with 0.5 mm glass plates. The top of the chamber remain open to enable adding of water and proteins. (B) In the ITO cell the electrode consists of thin gold wires on a coated glass plate glued to a 1 mm thick coverslip. The chambers used are both self made.

Electroformed GUVs normally have a diameter of 5 up to 200 μm, depending on the lipid composition, swelling medium, and the external AC field parameters, which establish the amplitude of the electroosmotic vibration and consequently the membrane tension of a GUV just after its formation. The predominating mechanism of electroformation is the electroosmotic periodic movement of the water medium at the water-electrode interface. These vibrations are directed perpendicularly to the electrode surface, where the initial lipid film is deposited. The vibrations pull lipid lamellae off the electrode causing their separation and growth. The vesicles increase in size up to 10-20 μm, this size corresponds to vesicles forming spontaneously from swelling lipid films. At this stage they touch each other, increasing the contact zone, which is destabilized from the AC-field through electroosmotic vibrations. Thus, the neighbour vesicles fuse together into a large one, they become spherical and within a few minutes they close their neck and eventually separate from the electrode (Figure 2.3).
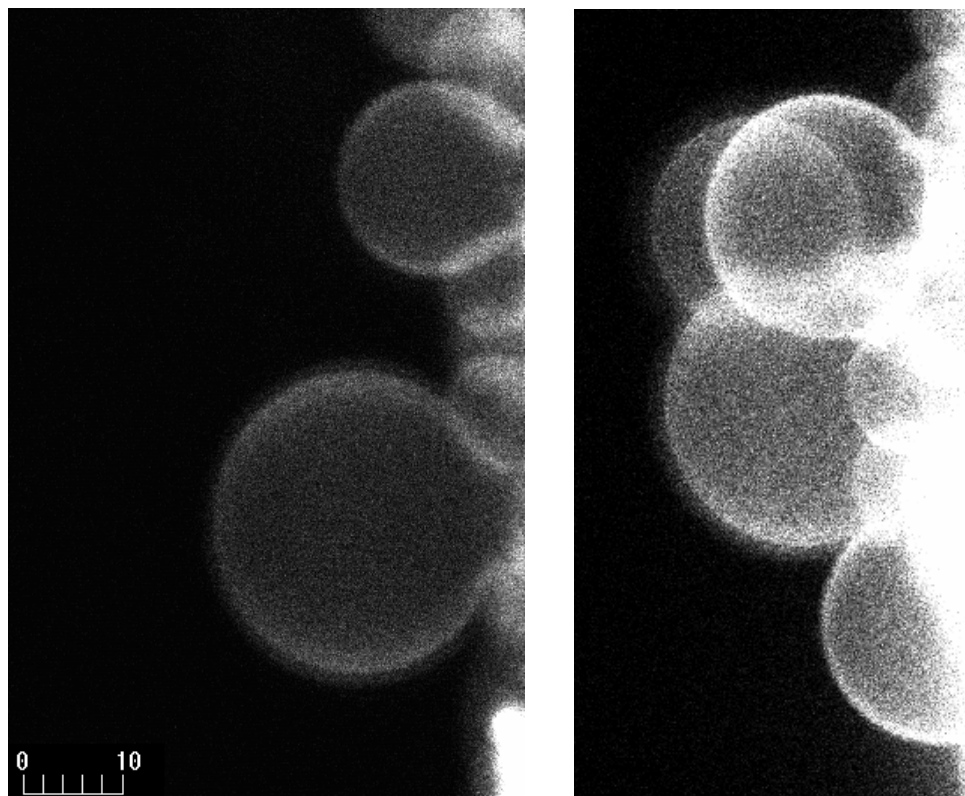
Figure 2.3 Examples of fluorescence images of electroformed GUVs made from DOPC/SM/Chol (1:1:1, molar ratio) in Millipore water at $T = 30$ °C, bar = 10 µm. The vesicles bind on the right part on the Pt wires.

2.1.4   Set up for the pressure experiments

The GUVs are first grown by electroformation in a Teflon or ITO chamber, after that they are sucked into a fused silica microcapillary (Polymicro, Phoenix, AZ) of cylindrical geometry, with an outer diameter of 360 µm and an inner diameter of 50 µm, by applying suction on one end of the open capillary after connecting it to a syringe, while the other end is in contact with the sample. Once the sample is loaded, the free end of the capillary is sealed. The seal at one end of the capillary occurs by touching the very extreme of the capillary with the flame of a blowtorch, which fuses the silica together. The last centimetre of the capillary is normally void of sample, so that the heat is not in direct contact with the sample. The thermal conductivity of fused silica is low. The other end of the capillary, which is inserted in a ~400 µm hole drilled in modified aluminum pressure plug (Figure 2.4) and secured with epoxy glue, is connected to commercially available pressure tubing (HPI, Erie, PA). The pressure plug fits the receptacle of the coupling unit, which provides the high pressure connection

between the capillary and the pressure tubing. The pressure tubing is connected with a homebuilt pressure generator, which uses ethanol as a pressure-transmitting medium. A manually operated piston screw pump (HIP 37-5.75-60, Erie, PA) was used to generate hydrostatic pressure. A standard pressure gauge (HIP 6PG75, Erie, PA) was connected to the pump for determining the pressure of the system.
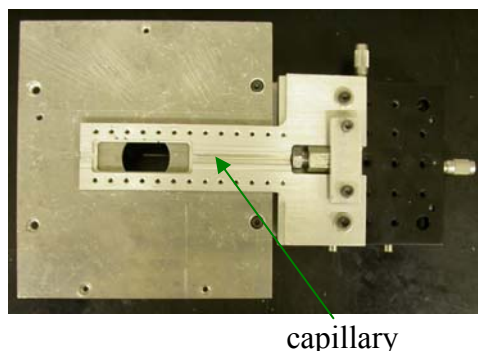
capillary

Figure 2.4 Capillary mounted on an aluminium plate, which fits the microscope stage.

The use of a thin fused silica capillary permits accommodation of the GUVs on the one hand (Figure 2.5), and the use of high N.A. immersion objectives on the other hand.

50 µm
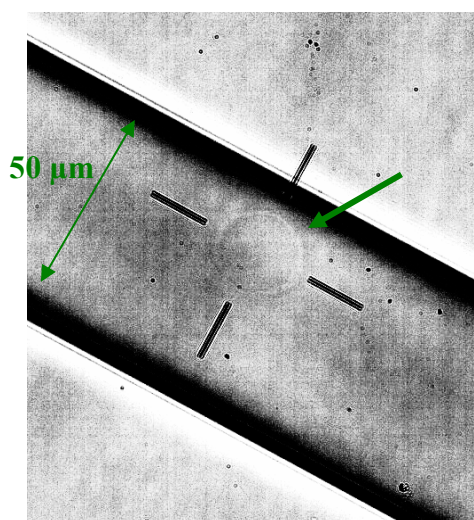
Figure 2.5 Thin fused silica capillary with a GUV inside. The capillary has an inner diameter of 50 µm and a wall thickness of 155 µm.

2.1.5   Fluorescent dyes

Laurdan and Prodan These naphthalene derivates belong to the family of polarity-sensitive fluorescent probes. Their chemical structures are depicted in Figures 2.6(A) and 2.6(B). In polar solvents, a reorientation of solvent dipoles around the probe may occur. The energy required for this reorientation results in a continuous red shift of the fluorescence emission spectrum. The dipolar relaxation is due to the water molecules present in the bilayer at the level of the polar head group/hydrophobic chain region where the Laurdan resides. The concentration and the molecular dynamics of water molecules change in the different lipid phase states. As a consequence, the gel and fluid lipid phases are characterized by blue (~440 nm) and green (~490 nm) emission, respectively. To quantify the emission spectral changes, the excitation generalized polarization (*GP*) function was defined analogously to the fluorescence polarization function as:

$$GP = \frac{I_\text{B} - I_R}{I_\text{B} + I_R} \tag{2.2}$$

where I_B and I_R correspond to the intensities at the blue and red edges of the emission spectrum, respectively, for a given excitation wavelength (PARASASSI, 1990; PARASASSI, 1991).

By detecting Laurdan's excited-state in the lipid membranes is possible, through the photoselection effect, to discriminate between ordered and disordered lipid domains. The photoselection effect is due to the fluorophores that are aligned parallel, or nearly so, to the plane of polarization. If different regions of a vesicle are considered, strong excitation occurs in the direction parallel to the excitation polarization (hence, the strongest excitation will be in the equatorial region of the vesicle), whereas poor or no excitation will occur in regions perpendicular to the excitation polarization, i.e. in the polar region of the spherical vesicle.

Another important aspect, which should be considered is the relationship between the pixel and the lipid domain size. When the lipid domains are smaller or comparable to the pixel size, then the *GP* value of the image corresponds to an average *GP* value, only, whereas by lipid domains bigger than the pixel size, the *GP* regions will be clearly separated (PARASASSI, 1997).

Prodan shows the same photoselection effect as Laurdan. This fluorescent molecule, however, due to its partition coefficient which is 35 times higher in the fluid phase with

respect to the gel phase, partitions preferentially into the fluid phase (KRASNOWSKA, 1998). Prodan as also Laurdan shows a lipid-phase-dependent spectral shift and the *GP* function can be computed from the GUV centre cross-section images.

N-Rhodamin Differently to the fluorophores mentioned above, *N*-Rh-DPPE does not display the photoselection effect, because the excited-state dipole of this probe is aligned parallel to the surface of the GUVs (BAGATOLLI, 2000). Therefore, the discrimination between gel and fluid lipid domains depends on the changes in the probe concentration in the coexisting lipid phases. In addition, the effective concentration of *N*-Rh-DPPE in the gel and fluid lipid domains depends on the nature of the lipid systems (BAGATOLLI, 2000). In this case, it will not be judicious to generalize the fluorescent molecule's affinity of *N*-Rh-DPPE for the different lipid phases without a careful probe characterization. Its chemical structure is given in Figure 2.6(C).

Bodipy (4,4'-difluor-4-bora-3a,4a-diaza-*s*-indacen) was chosen as marker of N-Ras protein because of its features. Its most important characteristics are: a good photostability, a lack of ionic charge, a high fluorescent quantum yield, and at the same time a small sensibility towards photobleaching. Its spectral properties are insensitive to solvent polarity and pH and its little or no spectral overlap with longer wavelength dyes such as tetramethyl-rhodamine and Texas Red make it useful for multicolour applications. The binding of this small molecule to the protein does not influence the biological activity of the protein. Figure 2.6(D) shows its chemical structure.
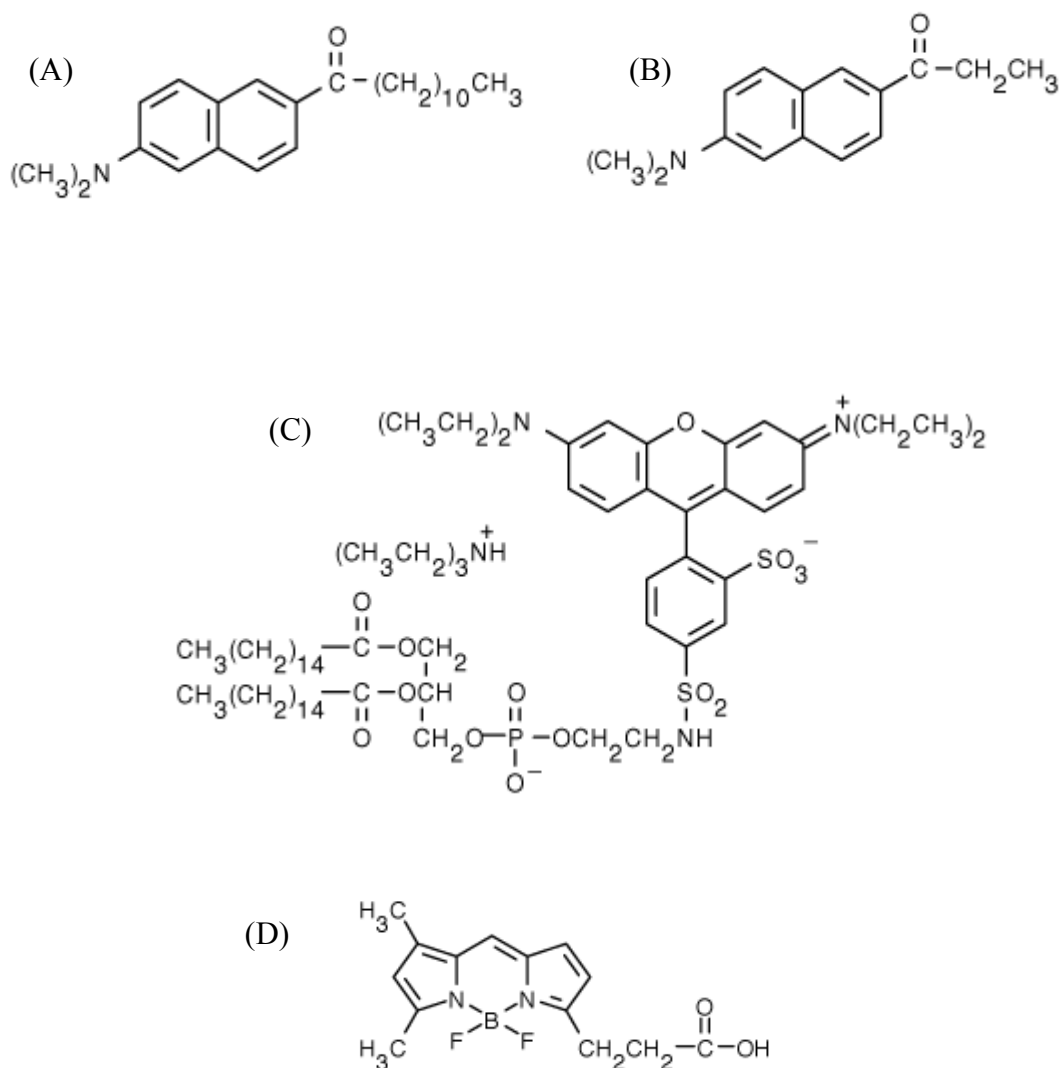
Figure 2.6 Chemical structures of (A) 1-dodecanone, 1-(6-(dimethylamino)-2-naphthalenyl) (Laurdan); (B) 1-propanone, 1-(6-(dimethylamino)-2-naphthalenyl) (Prodan); (C) lissamine rhodamine B, 1,2-dihexadecanoyl-*sn*-glycero-3-phosphoethanolamine (*N*-Rh-DPPE); (D) 4,4'-difluor-4-bora-3a,4a-diaza-*s*-indacen (Bodipy).

2.2   Circular Dichroism (CD)

Circular Dichroism spectroscopy is used to measure the interaction of polarized light with optical active (i.e., asymmetric) molecules. The symmetry present in many individual chromophores of proteins prohibits the optical activity. However, the optical activity of these chromophores may be induced by their interaction with an asymmetric environment provided by the rest of the protein molecule. As a consequence, CD spectroscopy provides a sensitive tool to probe conformational properties of proteins and polypeptides, thanks to the spatial asymmetry of the constituent amino acids.

CD spectra of proteins and peptides are usually measured in two spectral regions. In the far-UV region (approximately 180-250 nm) the measured bands represent the electronic transitions of the amid groups of the protein backbone. The sign, magnitude, and position of these bands are strongly dependent on the φ and ψ angles of the peptide bond. From this region of the spectrum it is possible to obtain information about the secondary structure of the protein. The analysis of the bands in near UV region (approximately 250-350 nm) are influenced by the side chains of aromatic amino acids and by disulfide bonds. The CD-spectra depending on the local environment of the aromatic amino acids and on their orientation with respect to the backbone provide a fingerprint of the tertiary structure of the protein molecule.

Circular dichroism is defined as the difference between the extinction coefficients for left and right circular polarized light:

$$\Delta \varepsilon(\lambda) = \varepsilon_L(\lambda) - \varepsilon_R(\lambda) \tag{2.3}$$

where $\varepsilon_L(\lambda)$ and $\varepsilon_R(\lambda)$ represent the extinction coefficients for left and right polarized light, respectively, at wavelength λ. Since, according to the Beer-Lambert law extinction coefficient, $\varepsilon_{L,R}$, are related to the ordinary absorption $A_{L,R}$ by the formula:

$$\varepsilon_{L,R} = A_{L,R}(\lambda)/lc \tag{2.4}$$

where l is the pathlength of the cell (in cm) and c is the concentration (mol/l), one can express circular dichroism as:

$$\Delta\varepsilon(\lambda) = \Delta A_{L,R}(\lambda)/lc \tag{2.5}$$

where $\Delta A_{L,R} = A_L(\lambda) - A_R(\lambda)$.

For most historical and instrument reasons, the CD data are often expressed not as $\Delta\varepsilon(\lambda)$ but in terms of molar ellipticity, $\theta(\lambda)$, which has units of deg cm^2 dmol^{-1}. In the far UV region, the principal chromophore of interest is the peptide bond and the molar unit is based on the mean residue weight, i.e. the molecular weight of the protein divided by the number of amino acids in the protein molecule. On the other hand, near UV spectra measure the signal from specific chromophoric groups, and the molar unit used in this case is often based on the concentration of the whole macromolecule.

2.2.1   Far UV CD spectra and protein secondary structure

CD spectra consist of electronic transitions between a ground and an excited state of a molecule. Early measurements of CD spectra were focused on simple homopolypeptides, which are known to adopt well-defined secondary structures (GREENFIELD, 1969). These spectra are representative of three common elements of the secondary structure, i.e. α-helix, β-sheet and random structure. The spectrum of α-helices shows an n $\rightarrow \pi^*$ transition coupled with a negative CD band at ~222 nm, whereas the perpendicular and the parallel exciton peaks resulting from an $\pi \rightarrow \pi^*$ transition show a positive band at ~190 nm and a negative one at ~208 nm. In contrast, β-sheets exhibit a negative band at ~215 nm due to an n $\rightarrow \pi^*$ transition and a positive band at ~198 nm due to $\pi \rightarrow \pi^*$ transitions (WALLACE, 2000). CD spectra of many β-turns are still not well-characterised. Furthermore, there is a substantial controversy regarding suitable peptide models for various types of β-turns and random structures. However, the best known structure for a β-turn gives rise to a positive band at ~205 nm, a negative below 190 nm, and a weak one at ~225 nm. In contrast, a random structure shows a strong negative peak at ~220 nm (WU, 1992).

Many methods have been developed for quantitative analyses of CD spectra. Most of these approaches assume that the secondary structure of the measured protein can be obtained by fitting the experimental spectrum with reference spectra believed to represent pure components of the secondary structure. However, the analyses of CD data based on the use of reference spectra of model polypeptides, when applied to proteins may present disadvantages. The spectra of long polypeptides may provide a good model for infinitely long α-helices or β-

sheets, for example, but these structure segments in proteins could be very short and their spectral properties may differ from those infinitely long. In contrast, the convex constraint analyses is based on a deconvolution method, i.e. this algorithm uses only experimental CD curves, without any reference spectra originating from model peptides or proteins of known secondary structure. The CD spectra are decomposed into at least four pure components, which have to be chosen *a priori*. Importantly, these components show remarkable resemblance to the CD spectra of known secondary structure (PERCZEL, 1991; PERCZEL, 1992).

2.2.2   Experimental part

The CD spetra were recorded between 2 and 95 °C in a cylindrical thermo-cell (1 cm path length) from 190 to 260 nm on a JASCO J-715 spectropolarimeter under constant nitrogen flush (Table 2.1). An external water thermostat was used for temperature-dependent measurements to control the temperature within 0.1 °C. Temperature dependent CD scans were carried out by first cooling the sample to 2 °C and then stepwise increasing the temperature from 2 to 95 °C, and allowing the samples to equilibrate at each temperature for 15 min. CD data are expressed as the mean residual ellipticity (MRE) $[\theta]$ in ° cm^2 $dmol^{-1}$. The secondary structure content of the peptide in solution was determined using the Convex Constraint Analysis (PERCZEL, 1991; PERCZEL, 1992) with two conformational states (turns/strands and unordered conformations).

Table 2.1 Instrumentation parameters for CD-spectrometers J-715.

Parameter	Adjustment
Wavelength λ / nm	190-260
Increment $\Delta\lambda$ /nm	1
Scan velocity $\Delta\lambda/\Delta t$ / nm/min	100
Band width λ_{FWHM} / nm	1.0
Response time t / s	0.5
Sensitivity ψ_{max} / m°	100
Scans n	20

2.3   Fourier transform infrared (FTIR) spectroscopy

In IR spectroscopy the absorption of the infrared light obeys the Bouger-Lambert-Beer's rule. IR spectroscopy has become a standard method to investigate lipid model membranes, peptides and proteins (REIS, 1996; SIMINOVITCH, 1987; TAMM, 1997). With this method it is possible to identify in dependence of frequencies, widths, intensities, shapes and splitting of the IR absorption bands the structure of the measured molecules, and their interactions with the surroundings. In studies of lipid model membranes, for example, qualitative information about conformations and phase transitions are achievable. At the same time the different behaviours of the hydrophobic acyl chains or of the hydrophilic head groups are detectable. In studies of proteins the analysis of the amid band I deliver qualitative and quantitative information about their secondary structure.

The carbon hydrogen stretching vibrations appear in the spectral region between 3000 and 2800 cm^{-1}, where the CH_2 antisymmetric stretching mode is observed at ~2920 cm^{-1} and the CH_2 symmetric stretching mode at ~2850 cm^{-1}. These bands give rise to very strong signals and they are very important in the analysis of lipid model membranes, because their position is conformation sensitive, i.e. the *trans/gauche* ratio in the lipid acyl chains varies in dependence of temperature and pressure (REIS, 1996). At low temperatures (gel-phase) the methyl groups have an *all-trans* conformation and the CH_2-stretching mode occurs at ~2849 cm^{-1}. Upon increasing the temperature, there is a shift to higher wavelengths indicating a phase transition from a gel to a fluid phase. Through the melting of the acyl chains the number of the gauche-conforms increase drastically. The symmetric and antisymmetric absorption bands of CH_3-groups appear at ~2871 cm^{-1} and ~2956 cm^{-1} and show weak intensities.

The most important band in the head group region of the lipids is the C=O stretching mode (at 1800-1700 cm^{-1}). The analysis of this band gives information about the level of hydration of the lipid carbonyl group at the polar/apolar interface. The study of the position of the antisymmetric PO_2^--band is also used as indicator for hydrogen bonds as well as the amid-I band of the amid group in ceramide, sphingolipid, and glycolipid.

2.3.1   Experimental part

The FTIR spectra in this work were recorded with a Nicolet MAGNA 550 spectrometer equipped with a liquid nitrogen cooled MCT (HgCdTe) detector. For the pressure dependent measurements, the infrared light was focussed by a spectral-bench into the pin-hole of a diamond anvil cell (DAC) with type IIa diamonds (REIS, 1996; PANICK, 1998; SIMINOVITCH,1987; HERBERHOLD, 2003). Each spectrum was obtained by co-adding 512 scans at a spectral resolution of 2 cm^{-1} and was apodized with a Happ-Genzel function (Table 2.2). The sample chamber was purged with dry and carbon dioxide free air. Powered α-quartz was placed in the hole of the steel gasket of the DAC and changes in pressure were quantified by the shift of the phonon band of quartz appearing at 695 cm^{-1} (SIMONOVITCH, 1987). The temperature dependent measurements were carried out using a cell with CaF_2 windows separated by 50 μm Teflon spacers (Table 2.3). An external water thermostat was used for the pressure- and temperature-dependent measurements to control the temperature within 0.1 °C. The equilibration time before recording spectra at each temperature and pressure was 15 min.

Table 2.2 Instrumentation parameters for the pressure dependence FTIR measurements.

Detector	MCT/A
Scans	512
Focal aperture	68
Apodisation function	Happ-Genzel
Zero-Filling	nein
Resolution	2 cm^{-1}

Table 2.3 Instrumentation parameters for the temperature dependence FTIR measurements.

Detector	MCT/A
Scans	256
Focal aperture	9
Apodisation function	Happ-Genzel
Zero-Filling	nein
Resolution	2 cm^{-1}

2.4   Infrared reflection absorption spectroscopy (IRRAS)

Infrared spectroscopy is usually performed in transmission mode. However, next to the transmission method other techniques were developed like, for example, reflection methods. The reflection techniques are classified into two main categories: internal and external reflection. The physical principles of the internal reflection spectrometry or attenuated total reflectance infrared (ATR/IR) spectrometry are based on the different refraction indices between the sample and a medium with a higher index of refraction at the interface. The infrared beam passes through an infrared transmitting crystal with a high refractive index like Ge or ZnSe, which is in direct optical contact with the sample. The beam enters the crystal and penetrates "into" the sample with each reflection via a so-called "evanescent" wave. At the end of the crystal, the beam is directed to the detector.

An example of an external reflection method is given by the infrared reflection absorption spectroscopy (IRRAS). In this technique, the resulting spectrum depends on the film thickness of the substrate, the absorption coefficient, the reflectivity, and the molecular orientation of the sample, the angle of incidence and the polarization of the incident radiation. Figure 2.7 shows the incident and reflected electric field vectors (E_p and E_s) of the so-called p and s components of radiation of the three phase system air, substrate, and water in a schematic representation. With respect to the plane of incident, p represents the parallel polarized radiation and s refers to the perpendicular one. Being the phase shift of the perpendicular component, s, nearly 180° for all angles of incident is the pure amplitude of the IR radiation parallel to the substrate surface zero. Consequently, s exhibits no significant dependence upon the variation of the angle of incidence. On the contrary, the phase shift of p strongly depends upon the angle of incidence. At its maximum (88°), the p-polarized radiation sums up of the incident and reflected electric field vectors of p, leading to a net combined amplitude that is almost twice that of the incident radiation. Thus, the obtained differential reflectance spectrum of the absorbed surface species, $\Delta R / R$, is expressed as follows:

$$\Delta R / R = \left(I_p - I_s \right) / \left(I_p + I_s \right), \tag{2.6}$$

where I_p is the intensity of the p-polarized component of radiation, and I_s the intensity of the s-polarized component of radiation.

Only *p*-component radiation interacts with the surface of the sample. Therefore, it is possible to do measurements in IRRAS only if the active vibrations have a component of the dynamic dipole polarized in the direction normal to the surface of the sample.
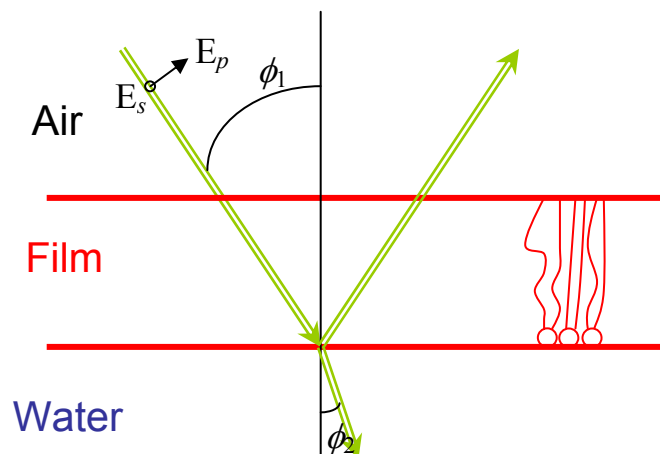
Figure 2.7 Optical constants of the three-phase-system air, film, and water (KERTH, 2003).

The IRRAS instrument used in this work is located at the Martin-Luther-Universität Halle-Wittenber, Germany (department of Physical Chemistry) and consists of a reflection device (Brucker, Karlsruhe), which is under a Plexiglas cover, in order to minimize evaporation of D_2O, a FTIR spectrometer (Equinox 55, Brucker) with a high sensible MCT-detector, and a KRS-5-polarisator (Figure 2.8). The IR-radiation from the spectrometer is first split up into different beams which pass through different planar mirrors. The last mirror having a focal width of 250 mm increases the reflection intensity and decreases the error of the incident angle. The incoming beam is injected into a polarisator, which in this position also avoids possible depolarisation of the electromagnetic radiation due to the mirrors. A computer controls the adjustment of the polarisator as well as the position of the mobile equipment, which regulates the incident angle (between 20° and 80°). After the reflection at the water/air interface the reflected beams are guided through mirrors first into a second mobile arm with the same characteristic and alignment like the first one and then into an external detector. The trough system was positioned on a moveable platform to be able to shuttle between the sample and the reference trough. This shuttle technique diminishes the spectral interferences due to the water vapour absorption in the light beam.

All spectra were recorded at a spectral resolution of 8 cm^{-1} using a Blackman-Harris-4-Term apodisation and a zero filling factor of 2. For each spectrum 1000 or 2000 scans were co-added over a total acquisition time of about 4.5 min, respectively (Table 2.4). Spectral calculations were performed using a Visual Basic program with an implementation of the formalism published by Mendelsohn *et al*. and Flach *et al*. (MENDELSOHN, 1995; FLACH, 1997).
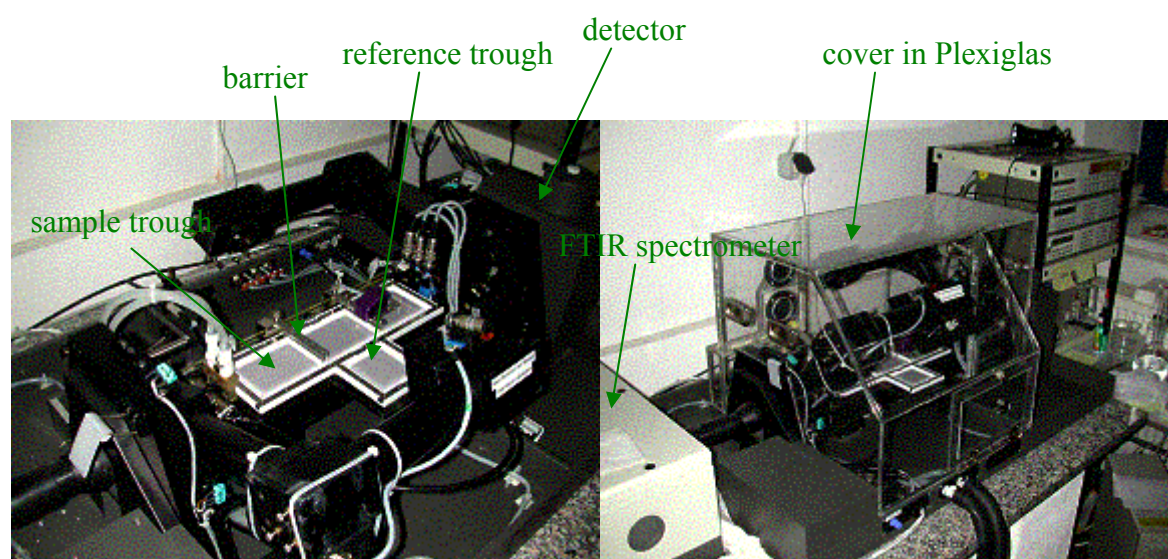
Figure 2.8 IRRAS-instrument.

Table 2.4 Instrumentation parameters for the IRRAS measurements.

Detector	MCT
Scans	1000 or 2000
Acquisition time	~4.5 min
Apodisation function	Blackman-Harris 4 Term
Zero-Filling	2
Resolution	8 cm^{-1}

All the experiments were conducted in a Langmuir trough, which consists of a thermostated sample trough, made of Teflon ($300 \times 60 \times 3$ mm^3), barriers which are mechanically moved by a computer to control the trough area and a force measuring device (Wilhelmy-plate) to determine the surface pressure (surface tension). A second smaller Teflon trough ($60 \times 60 \times 3$ mm^3), the reference trough, is connected with the first one through three bores that permit to maintain the same fluid level in both troughs.

The Wilhelmy-plate made of filter paper partially immersed in the subphase determines the force due to the surface tension on the plate suspended. This force is then converted into surface tension (mN/m or dynes/cm) with the help of the dimensions of the plate.
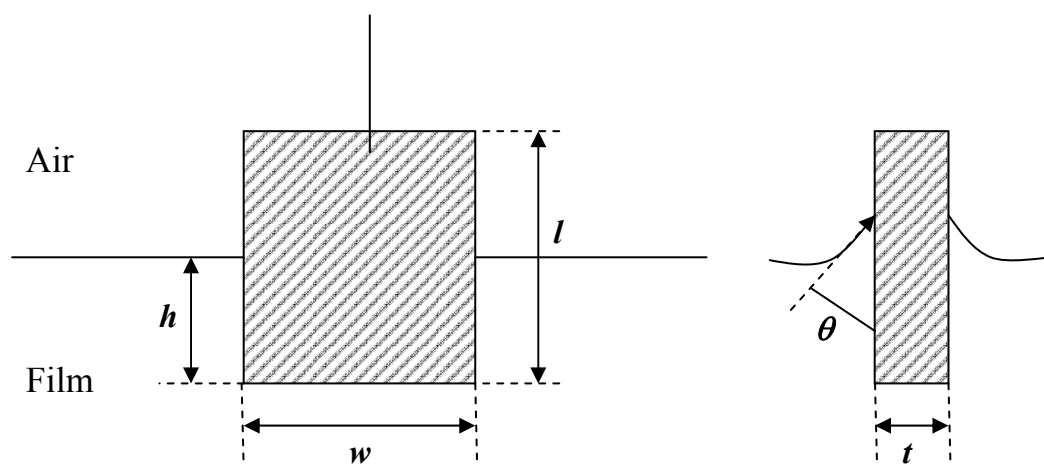
Figure 2.9 Schematic representation of a Wilhelmy-plate.

Figure 2.9 represents schematically a rectangular plate (index p) of dimensions l_p, w_p, t_p of material having a density of p_p immersed to a depth h_l in a liquid (index l) of density ρ_l, in this case the net downward force is given by the following equation:

$$F = p_p g l_p w_p t_p + 2\gamma(t_p + w_p)(\cos\theta) - \rho_l t_l w_l h_l g \qquad (2.7)$$

where γ is the liquid surface tension, θ is the contact angle of the liquid on the solid plate, and g is the gravitational constant. The surface pressure is calculated by measuring the change in F for a stationary plate between a reference surface and a surface containing the sample. If the

plate is completed wetted by the liquid (i.e. $\cos\theta = 1$) the surface pressure is then obtained from the following equation:

$$\Pi = -\Delta\gamma = -[\,\Delta F\,/\,2\,(t_\mathrm{p} + w_\mathrm{p})] = -\Delta F\,/\,2\,w_\mathrm{p}, \quad \text{if } w_\mathrm{p} \gg t_\mathrm{p} \tag{2.8}$$

2.5 Small-angle x-ray scattering (SAXS) and neutron scattering (SANS)

2.5.1 SAXS

In this work the SAXS and SANS methods were used to perform studies of multilamellar lipid systems. The diffraction patterns resulting from the SAXS and SANS measurements are investigated considering the lipid-water dispersion equivalent to powder samples composed of many randomly oriented microcrystals. According to Bragg' s law, the position of the diffraction peaks are related to periodic distances within the lyotropic lipid mesophase, whereas their width gives information about the extent of this periodicity. The measured reciprocal spacings are obtained from the following equation:

$$s = \frac{2}{\lambda}\sin\theta \tag{2.9}$$

where 2θ is the scattering angle and λ is the wavelength of radiation. Lamellar lipid-water mesophases consist of alternating layers of lipid and water molecules, denoted as L or P, which form a quasi one-dimensional periodic structure. The mesophase structure and the corresponding lattice constants were determined from the positions of the low-angle Bragg reflections. The lattice constant a_lam of the lamellar phases was calculated from the measured reciprocal spacings:

$$s_\mathrm{lam} = \frac{n}{a_\mathrm{lam}} \quad (\text{order of reflection } n = 1,2\ \ldots). \tag{2.10}$$

Besides the lamellar structure lipids might assume other configurations, which are also identified by their characteristic small-angle diffraction pattern. For example, in an inverse

hexagonal lipid-water mesophase (H_{II}), consisting in cylindrical water rods surrounded by lipid monolayers, the peak positions are described by the following equation:

$$s = \frac{2}{\sqrt{3}a}\sqrt{h^2 + k^2 + hk} \qquad (2.11)$$

where a, the lattice constant, in this case represents the distance between the centres of two neighbouring rods and h, k are the Miller indices. Moreover, Bragg peaks of cubic lipid structures may be observed at:

$$s = \frac{1}{a}\sqrt{h^2 + k^2 + l^2} \qquad (2.12)$$

a is the cubic lattice constant and h, k, and l the Millar indices, which depend on the lattice type (primitive, body-centred, face-centred).

2.5.2   Experimental part

The SAXS data were collected at the Soft Condensed Matter Beamline (A2) of the DORIS storage ring, Deutsches Elektronen-Synchrotron (DESY), Hamburg, Germany. The SAXS measurements were performed using x-rays of 8.27 keV energy (wavelength, λ, of 1.5 Å), a 1 m sample-detector distance, and a charge-couple device (MarCCD) based detector. Typical exposure time was 60 s. For the pressure dependent SAXS experiments, a high-pressure x-ray sample cell was used suitable for studies up to about 7 kbar at temperatures up to 80 °C, which is described by Kraineva *et al*. (KRAINEVA, 2005). Diffraction intensity versus reciprocal spacing, s, plots were obtained by radial integration of the 2D CCD images using the software FIT2D by A. Hammersley. The incident and transmitted beam intensities were recorded and used to normalize the data.

2.5.3   SANS

The scattering length (b_x) of atoms for x-rays are given approximately by:

$$b_x = \frac{e^2}{mc^2} Z \qquad (2.13)$$

where Z is the number of electrons in the atom, m the mass of the electron, c the light velocity e the electron charge. In x-rays scattering hydrogen has a very small value for b_x, whereas C, N, and O are roughly the same in scattering power. Considering the most common elements in biopolymers, for neutrons the most interesting observation is the negative value for hydrogen. Physically, this means that the neutron scattering from a hydrogen atom will be 180° out of phase with that from other atoms in the molecule having a positive neutron scattering length. In particular, it means that the scattering from H_2O is very different from that from D_2O. This important feature allows matching of the solvent background to the scattering from a macromolecule. Thus, in studying complex macromolecules and particles, it is possible, choosing a suitable H_2O/D_2O mixture, to produce matching selectively. If we consider lipid mixtures, under these so-called matching conditions, no SANS signal is obtained for homogeneously mixed lipids in the all-gel or all-fluid phases. We would detect a SANS signal in the case of phase heterogeneities (gel-fluid phase) due to the different compositions and scattering length densities of the two phases (WINTER, 2002).

2.5.4   Experimental part

SANS experiments were performed on the SAND diffractometer ($\lambda = 6$ Å) at the IPNS spallation source at the Argonne National Laboratory (USA). This instrument provides data in the range of momentum transfer $Q = (4\pi/\lambda)\sin\Theta$ (scattering angle 2Θ, wavelength of radiation λ) of $4.0\cdot10^{-3}$ to 1 Å^{-1} (length ($2\pi/Q$) scale range of about 2000 to 10 Å) in a single measurement. Standard treatment of isotropic SANS data was performed (WINTER, 1999).

The scattering length density is given as the sum of all atom scattering lengths per volume:

$$\rho = \sum_i b_i / V \qquad (2.14)$$

The differential coherent scattering cross-section as a function of momentum transfer Q can be written as

$$\frac{d\Sigma}{d\Omega} = n_p (\Delta\rho)^2 V_p^2 P(Q) S(Q), \qquad (2.15)$$

where n_p denotes the number density of particles, V_p the particle volume, $\Delta\rho = \rho_p - \rho_s$ is the contrast, i.e., the difference in mean scattering length density of the particles (ρ_p) and the solvent (ρ_s). $P(Q)$ is the square modulus of the form factor of the molecules describing the shape of the particles ($P(Q) \approx 1$ at $Q < 0.03$ Å^{-1}), and $S(Q)$ is the structure factor describing the spatial distribution of the particles. The SANS intensity within the coexistence region may be analysed by plotting $\ln(d\Sigma/d\Omega)$ vs. $\ln Q$. The obtained straight lines over the whole Q-range studied are indicative of a fractal-like structure of the sample. Fractals are disordered systems whose disorder can be described in terms of a non-linear dimension, the fractal dimension, D. In general, a disordered system may be allowed to consist of mass, surface and pore space, and may be classified according to the scaling behaviour of these three subsets. If mass and surface scale alike, the system is called a mass fractal (Figure 2.10(B)); if pore space and surface scale alike, it is called a pore fractal, and if only the surface is fractal, the system has irregularities that fill the entire surface and is called a surface fractal (Figure 2.10(A)). In the case of surface fractals, which are scatterers having a surface fractal only, the scattering law is given by:

$$\frac{d\Sigma}{d\Omega} \propto Q^{Ds-6} \tag{2.16}$$

with D_s being the surface-fractal dimension ($2 < D_s < 3$). If the scatterers in the sample are mass fractals, the SANS intensity is described by:

$$\frac{d\Sigma}{d\Omega} \propto Q^{-Dm} \tag{2.17}$$

with D_m being the mass-fractal dimension ($0 < D_m < 3$).

Considering equations (2.15) and (2.16), for $D_m = 3$, the domains are compact cluster whose surface scales independently of the mass are marginally space-filling when $D_s = 3$ (maximally convoluted surface), and are maximally space filling when $D_s = 2$ (smooth surface).
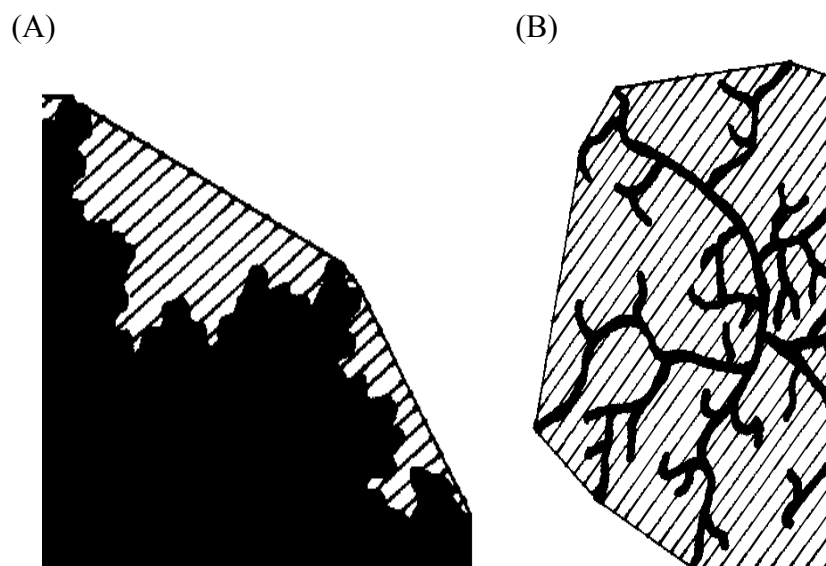
Figure 2.10 Schematic representation of (A) a surface fractal and (B) a mass fractal. Mass sites are shown in black, pore sites are shaded and surface sites are the boundary between the two (PFEIFER, 1989).

2.6 Materials

2.6.1 Lipids

POPC	1-palmitoyl-2-oleoyl-*sn*-glycero-3-phosphocholine	Avanti Polar Lipids
DOPC	1,2-dioleoyl-*sn*-glycero-3-phosphocholine	Avanti Polar Lipids
SM	sphingomyelin, brain porcine	Avanti Polar Lipids
DLPC	1,2-dilauroyl-*sn*-glycero-3-phosphocholine	Avanti Polar Lipids
Chol	cholesterol	Sigma-Aldrich

The lipids were used without further purification.

2.6.2   Fluorescence markers

Laurdan	1-dodecanone, 1-(6-(dimethylamino)-2-naphthalenyl)	Molecular Probes
Prodan	1-propanone, 1-(6-(dimethylamino)-2-naphthalenyl)	Molecular Probes
N-Rh-DPPE	lissamine rhodamine B, 1,2-dihexadecanoyl-*sn*-glycero-3-phosphoethanolamine	Molecular Probes

2.6.3   Peptide

GVG(VPGVG)   synthesised by Dr. B. Ludolph and Dr. G. Kragol from MPI Dortmund

2.6.4   Proteins

N-Ras wt 1-181 Bodipy MIC7 HDFarOMe

N-Ras wt 1-181 MIC7 HDFarBodipy

N-Ras wt 1-181 MIC7 HDHDOMe

all the proteins were synthesised by Dr. S. Schlummer, Dr. M. Lumbierres-Burgues, Dr. J. Palomo (Prof. Dr. H. Waldmann group), Dr. M. Kahms, and C. Nowak (PD Dr. J. Kuhlmann group) from MPI Dortmund.

2.6.5   Buffers and solvents

di-natriumhydrogenphosphate	Merck (Darmstadt)
LiI	Fluka (Taufenkirchen)
GuHCl	Sigma-Aldrich (Deisenhofen)
Urea	Fluka (Taufenkirchen)
TFE	Fluka (Taufenkirchen)
glycerol	Fluka (Taufenkirchen)
NaCl	Sigma-Aldrich (Deisenhofen)
D_2O	Sigma-Aldrich (Deisenhofen)

2.6.6   Softwares

Excel	Microsoft Inc. (Seattle, USA)
Origin 6.0	Microcal (Northhampton, USA)
Igor Pro V4.02A and V4.06A	Wave Metrics (Oregon, USA)
fit 2D V10.3	AP Hammersley/ESRF
SimFCS	Global for Images (by Enrico Gratton)
Jasco	Jasco Instruments
CCA	Convex Constraint Algorithm (by Perczel *et al.*)
Omnic V6.2	Thermo Nicolet Corporation
Spectra Calc Arithmetic A2.22	Galactic Industries Corp. (Texas Christian Uniuversity, Tadensz Zerda)

2.7   Sample preparation

2.7.1   FTIR, SANS, SAXS (lipid measurements)

The different lipid mixtures were prepared by first dissolving the required amounts of lipids in chloroform/methanol (4:1 v/v). The solvent was then completely removed under vacuum using a Speed Vac Sc 110 (Savant, Farmingdale, NY, USA) before adding D_2O to give dispersions. Homogeneous samples consisting of multilamellar vesicles were obtained after five freeze-thaw-vortex cycles.

2.7.2   Microscopy

Two-channels experiments Stock solutions of the lipids POPC/SM/Chol in mol% 50:25:25, 43:43:14 and 25:65:10 were mixed in 0.2 mg/mL chloroform/methanol (4:1 v/v). The fluorescent probe in chloroform already premixed with the lipids (*N*-Rh-DPPE:lipid) had a ratio of 1:400 (mol/mol).

The following steps were used to prepare the GUVs: 1) 5 µL of the lipid solution was spread on each platinum (Pt) wire under a stream of N_2. To remove residues of the organic solvent, the samples were dried at least 1 h under high vacuum. 2) To add the aqueous solvent into the chamber, the bottom part of the chamber was sealed with a coverslip. 2 mL of previously heated ($T = 61$ °C) 1 mM phosphate buffer (pH = 7) was added to cover the Pt wires. After this step, the Pt wires were connected to a function generator (Hewlett-Packard, Santa Clara, CA), and a low frequency AC field (sinusoidal wave function with a frequency of 10 Hz and an amplitude of 2 V) was applied for ~90 min. After vesicles formation, the AC field was turned off and the temperature scan (from high to low temperatures) was initiated. The temperature was measured inside the sample chamber with a digital thermocouple (model 400B; Omega, Stamford, CT) with a precision of 0.1 °C. A 7 mol% solution of the hexadecylated and farnesylated N-Ras in 1 mM phosphate buffer (pH 7) was added to the solution containing GUVs at ~30 °C.

High pressure experiments Stock solutions of phospholipids, cholesterol and Laurdan in DMSO (4 mol%) were prepared in a solution of chloroform/methanol (4:1 v/v) or only chloroform. The concentration of the different lipid stock solutions was 0.2 mg/mL. For preparing giant unilamellar vesicles (GUVs) from lipid stocks containing DOPC/SM(DPPC)/Chol, a chamber with Pt wires was used and a similar protocol was followed, as described above. The preparation of the GUVs for lipid stocks containing DLPC/POPC takes place in the ITO cell at room temperature. Ca. 10 µL of the lipid solution was spread homogenously on the gold wires. To remove residues of the organic solvent, the chamber was positioned under a stream of N_2 for ~1 h. Then sufficient water (~300 µL of Millipore water, 17.5 MΩ cm) was added to cover the wires. After this step, the wires were connected to a function generator (Hewlett-Packard, Santa Clara, CA), and a low frequency AC field (sinusoidal wave function with a frequency of 10 Hz and an amplitude of 3 V) was applied for 90 min. After vesicles formation, the AC field was turned off and the sample was loaded into a fused silica microcapillary.

2.7.3   IRRAS

Before each experiment, the troughs were cleaned with a diluted Hellmanex solution and rinsed thoroughly with pure water. After that they were filled with a buffer solution (100 mM NaCl in D_2O); the temperature of the subphase was maintained at 20 ± 0.5 °C. Three types of

experiments were performed. First, 50 µL of the respective N-Ras isoform (278 µM) were injected into the subphase and the time-dependent surface pressure increase, due to the adsorption at the air/water interface, was recorded. Second, the lipid mixture was dissolved in chloroform/methanol (4:1 v/v) and 19.8 µL of a 1 mM solution was then spread with a microsyringe at the air/water interface. After an equilibration time of 15 min the surface pressure area isotherms (Π / A isotherms) were detected. In the last kind of experiments, after preparation of the lipid monolayer, which occurred in a similar manner as described above, 50 µL of the respective proteins (278 µM) were injected into the subphase and the surface pressure increase was monitored maintaining a constant pressure (at 30, 20 and 10 mN m^{-1}) in one case and retaining a constant area in the other.

2.7.4   CD and FTIR spectroscopy (peptide measurements)

For the CD spectroscopy experiments solutions of the GVG(VPGVG) peptide in 0.5 M TFE, glycerol, urea and GuHCl, and in 2 M TFE and glycerol, were dissolved at concentrations of 0.5 mg/mL in 10 mM phosphate buffer at pH 7. The concentrations were determined spectrophotometrically using the absorption coefficient at 225 nm.

For the FTIR temperature-dependent experiments solutions of the peptide in 0.5 and 2 M LiI, were dissolved at a concentration of 5% (w/w) in 10 mM phosphate buffer. The pD of the solutions was adjust to 7.0 using DCl.

3   Results

3.1 *Pressure and temperature effects on conformational and hydrational properties of lamellar POPC/SM/Chol*

3.1.1   Introduction

In this chapter a ternary mixture was studied composed of cholesterol and two lipids, such as sphingomyelin (SM) (high T_m lipid) and POPC (1-palmitoyl-2-oleoyl-sn-glycero-3-phosphocholine) (low T_m lipid) (33:33:33, mol%), which is often used in studies of model raft mixtures. The scope of this section is to detect different phase behaviour of this model membrane, and to determine a p, T-phase diagram in a temperature range from ~1.3 to 66 °C and in a pressure range from 1 bar up to 9 kbar. To decipher the conformational differences of the various phases of POPC/SM/Chol (33:33:33) in excess water, different methods were applied like Fourier transform infrared (FTIR) spectroscopy, and small-angle x-ray scattering (SAXS). The data obtained are discussed in the following parts.

3.1.2   Temperature - and pressure - dependent FTIR spectroscopic measurements

As already discussed in chapter 2, FTIR spectroscopy is an effective method to obtain information on the conformation and molecular order of the acyl chains as well as structural changes at the interfacial region. The lipid system POPC/SM/Chol (33:33:33) was studied in excess D_2O analysing positions, and intensities of IR absorption bands.

Figure 3.1(A) shows the symmetric CH_2 stretching frequency as a function of temperature. As the temperature increases, the wavenumber of the symmetric CH_2 vibration at ~2849 cm^{-1} increases gradually by ~2 cm^{-1}, and a transition from an ordered to a disordered phase occurs due to increased elastical repulsive interactions between the lipid chains. The C=O stretching mode bands were fitted with three Gauss-Lorentz functions and the peak areas can be evaluated to determine hydration changes at the interface region of the lipid bilayer. Analyses of the band by Fourier self-deconvolution gives rise to three overlapping bands centred at ~1744, ~1730 and ~1712 cm^{-1}, which can be assigned to stretching vibrations of free carbonyl groups, that are not involved in hydrogen bonding, and to simple and multi-hydrogen-bonded C=O groups whose vibrations are red-shifted to lower wavenumbers, respectively (SYMONS, 1985). The C=O stretching mode in Figure 3.1(B) and the corresponding relative intensities shown in Figure 3.1(C) present two abrupt drops of the

wavenumbers. The first one at ~6 °C which indicates a transition to a disordered phase, probably from $l_o + s_o$ to the three-phase region $l_o + l_d + s_o$, and the second at ~27 °C which might indicate the disappearance of the solid phase. At higher temperatures it would be expected to detect another transition to an all l_d-phase, however differences in the hydration level between fluid like phases cannot be detected with sufficient accuracy with this method (REIS, 1996).

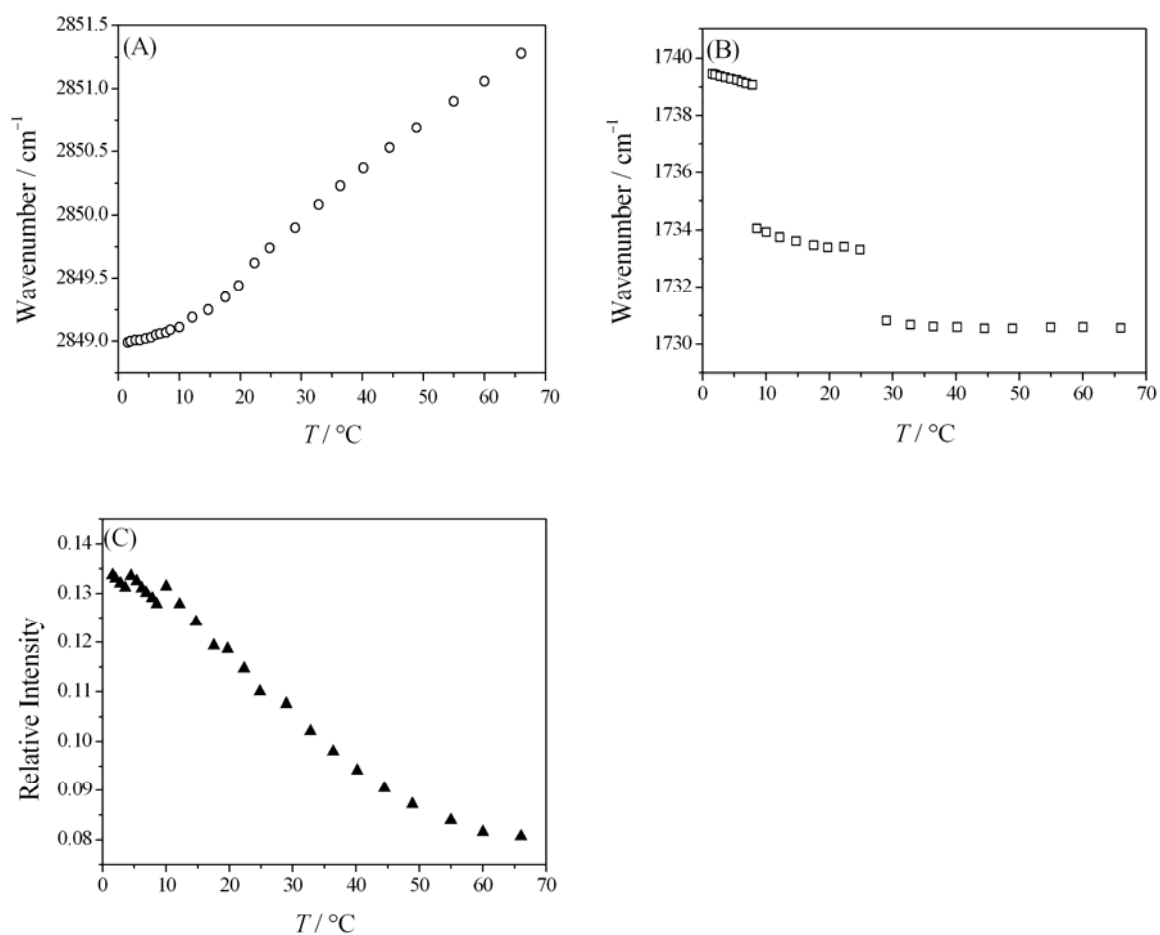Figure 3.1 Temperature dependence of (A) the CH_2 symmetric stretching mode wavenumber (at ~2850 cm^{-1}) and (B) the C=O stretching mode wavenumber (at ~1740 cm^{-1}) of POPC/SM/Chol (33:33:33) in excess D_2O. (C) Temperature dependence of the relative intensities of the band at 1744 cm^{-1}. This band represents the population of water-free carbonyl groups in the lipid head-group region.

The pressure dependence of the symmetric CH_2 stretching band at ~2851 cm^{-1} and of the C=O stretching mode at ~1740 cm^{-1} at different temperatures (15, 25, 45 and 66 °C) are shown in Figure 3.2. The frequency of the CH_2 stretching wavenumber varies linearly upon increasing pressure within experimental error over most of the pressure range studied. A pressure-induced linear blue shift is generally observed when elastic repulsive forces dominate the system. Most of the measurements at different temperatures show a broad transition that is expected for any three-component mixtures.

At 15 °C, an increase of the wavenumbers by ~6 cm^{-1} is detected with increasing pressure up to 8 kbar. At ~900 bar, the curve shows a kink in the wavenumber of the symmetric stretching mode, being probably indicative of the pressure-induced $l_o + l_d + s_o$ / $l_o + s_o$ transition. The C=O stretching vibrations at 15 °C only show a small change in the position of the wavenumber at ~3500 bar, the transition to the gel-phase. At higher temperatures $T =$ 25 and 45 °C, two and three phase changes are observed, respectively. For the lower temperature, the first transition is from a $l_o + l_d + s_o$ to $l_o + s_o$, which occurs at ~1100 bar, and at 45 °C a transition from $l_o + l_d$ to a $l_o + l_d + s_o$ at ~1000 bar, as can be inferred from drastical changes in the C=O stretching mode, only. The second transition is detected by the CH_2 stretching vibration. Figure 3.2 also shows transitions at 25 °C from the two-phase region $l_o + s_o$ to the gel-phase at ~4.2 kbar and one at 45 °C to a $l_o + s_o$ phase at ~3000 bar. A third transition to an all solid-phase occurs for the 45 °C measurement at ~4.8 kbar. At 66 °C, two-phase transitions occur. The first one detected by the CH_2 stretching mode at ~2.1 kbar points out the shift of the l_d to the two phase region $l_o + l_d$, whereas the second occurs at 2.8 kbar, as shown by the change of the C=O bands. The shift of the wavelengths by ~4 cm^{-1} depicts the formation of the gel phase.

However, because conformational changes of this kind could be very small and not always detectable with sufficient accuracy in the high-pressure sample environment of the diamond anvil cell, the results obtained by FTIR spectroscopy are combined with x-ray scattering data to help building the p, T-phase diagram of the system.
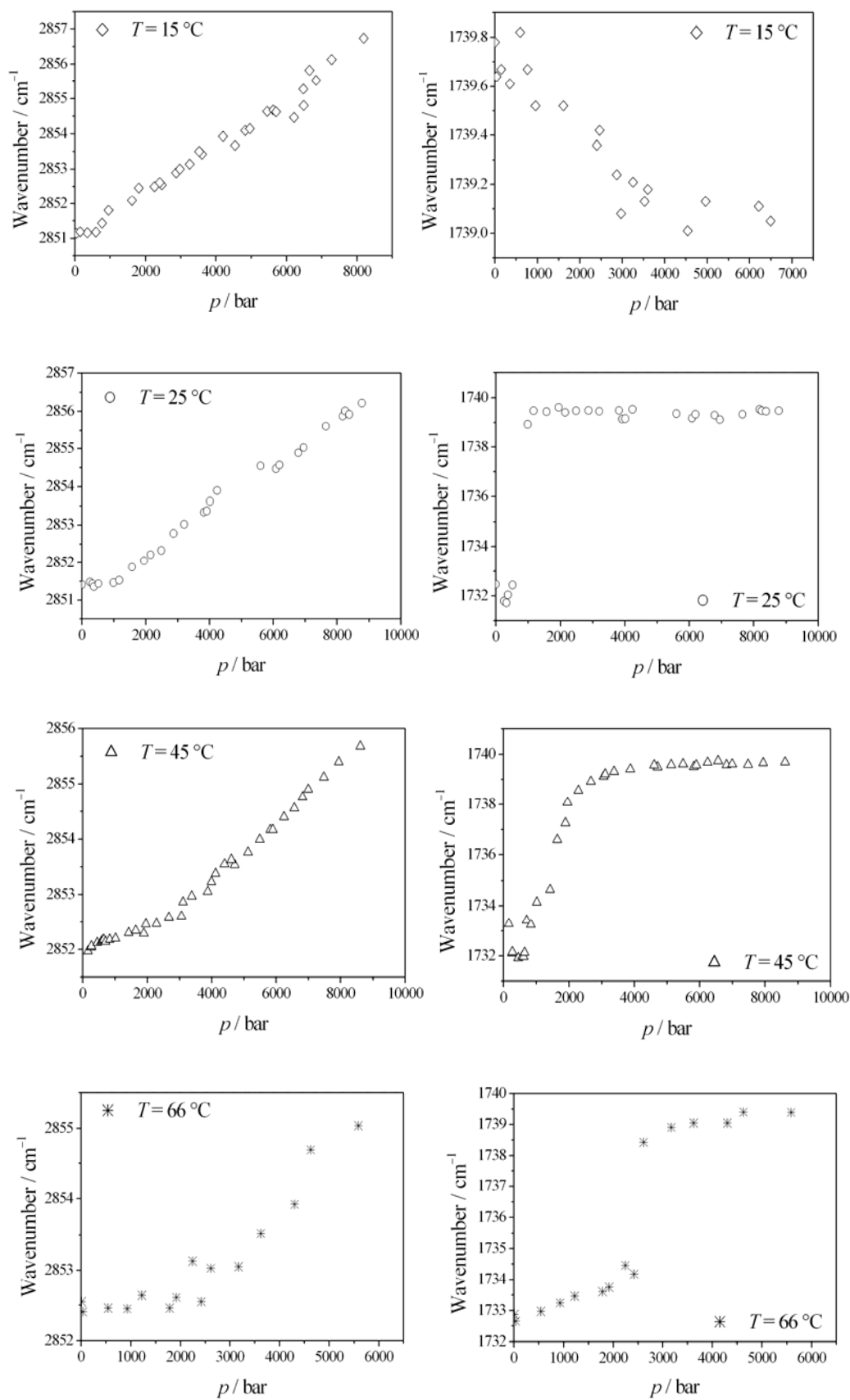
Figure 3.2 Pressure dependence of the CH_2 symmetric stretching mode and C=O stretching mode wavenumber at 2851 and at 1740 cm^{-1}, respectively of POPC/SM/Chol (33:33:33) in excess D_2O at different temperatures (15, 25, 45 and 66 °C).

3.1.3   Temperature- and pressure-dependent synchrotron small-angle x-ray scattering experiments

The positions of Bragg reflections in the small-angle x-ray scattering region were analysed to determine the topology of the lipid mesophases and the mean value of the lattice constants of the corresponding structures.

SAXS diffraction patterns of the three component system POPC/SM/Chol (33:33:33) in D_2O at different temperatures from 1.3 °C up to 63 °C are depicted in Figure 3.3(A). The lamellar lattice constant a of the second order Bragg reflections and half-widths δ are plotted as a function of temperature in Figures 3.3(B) and 3.3(C), respectively. The Bragg reflections display ratios of diffraction spacing of 1:2, which are typical of lamellar phases. The lattice constant of the lamellar phase decreases with increasing temperature by 2.8 Å. At ~2 °C, a has a value of 71.5 ± 0.8 Å, which corresponds to an ordered-phase $l_o + s_o$. Upon increasing the temperature, a decreases and in an all l_d-phase has a value of ~68.5 ± 0.8 Å. The behaviour of the half-width δ highlights two phase transitions: the first, which reveals the loss of the solid-phase when entering the $l_o + l_d$ region at ~23 °C, and the second one from the $l_o + l_d$ phase to an all l_d-phase at ~43 °C. No significant changes in small-angle diffraction pattern are observed at the $l_o + s_o$ / $l_o + l_d + s_o$ transition, which, however, was detected in the FTIR measurements (see above).

SAXS diffraction patterns at different temperatures (15, 25, 45 and 65 °C) of the same lipid mixture from 1 bar up to 5500 bar, at 300-400 bar intervals, are shown in Figure 3.4. The lamellar lattice constant a of the second order Bragg reflections and the respective half-widths δ are plotted for these temperatures as a function of pressure in Figure 3.5. The Bragg reflections at all pressures display ratios of diffraction spacing of 1:2, as already seen in the case of the temperature-dependence measurements. Again, as in the case of the temperature-dependence measurements, more precise information about phase transitions is obtained by considering the lattice constant a and the half-widths δ concomitantly. At 15 °C, a kink of the half-widths δ appears at ~1000 bar, and then δ increases up to ~3.1 kbar. The two transitions might correspond to a $l_o + l_d + s_o$ / $l_o + s_o$ and $l_o + s_o$ / s_o phases. The lamellar lattice constant a increases up to ~5 kbar by ~1.4 Å, and reaches a plateau at ~3.1 kbar indicating the presence of a gel-phase. At 25 °C, one main transition to an ordered phase is detected; a changes by ~2.5 Å upon increasing pressure up to ~3500 bar and the half-widths δ kinks at ~1.5 kbar. The transition indicating the formation of a solid-phase takes place at ~2.3 kbar for 45 °C, the lamellar lattice constant a increases by ~3 Å at this temperature upon increasing the pressure.

At higher temperature (65 °C) two changes in the half-widths δ, at ~1.2 and ~2.7 kbar, respectively, are depicted; the lattice constant shows an s-shape progression and reaches a value of ~71 ± 0.8 Å. The changes observed probably correspond to the phase transitions l_d / $l_o + l_d$ and $l_o + l_d$ / $l_o + l_d + s_o$, respectively.
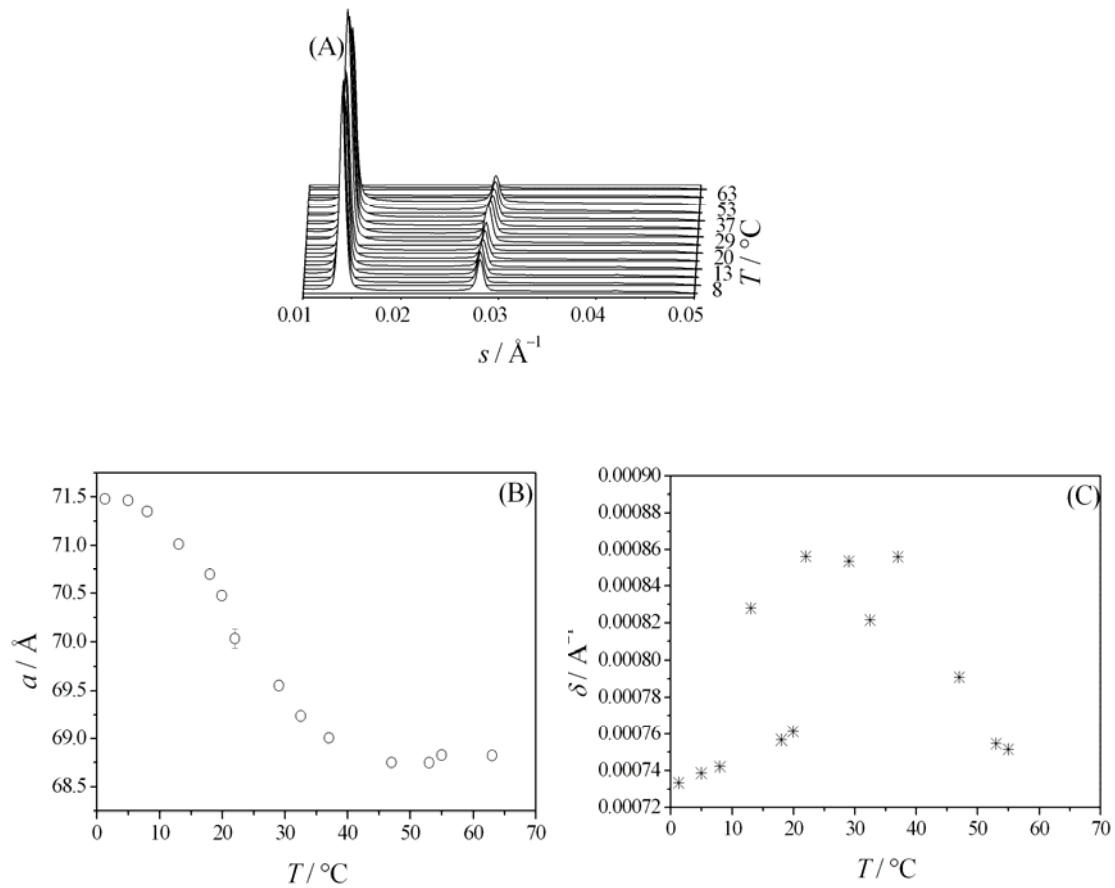
Figure 3.3 (A) Diffraction patterns of POPC/SM/Chol (33:33:33) 20% (w/w) in D_2O during a heating scan from 1.3 to 63 °C. (B) and (C) Lattice constant a and half-widths δ of second-order Bragg reflections of the same lipid mixture as a function of temperature.
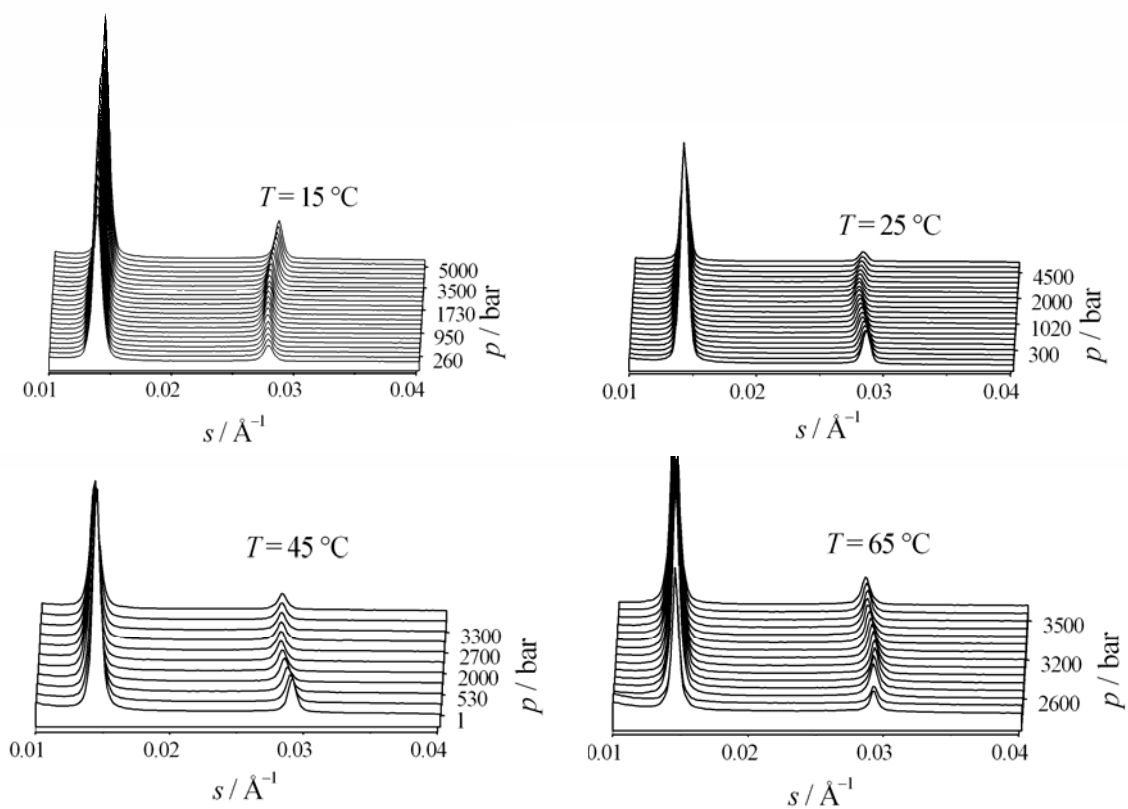
Figure 3.4 Diffraction patterns of POPC/SM/Chol (33:33:33) 20% (w/w) in D_2O during pressure scans from 1 to ~5000 bar at different temperatures (15, 25, 45 and 65 °C).
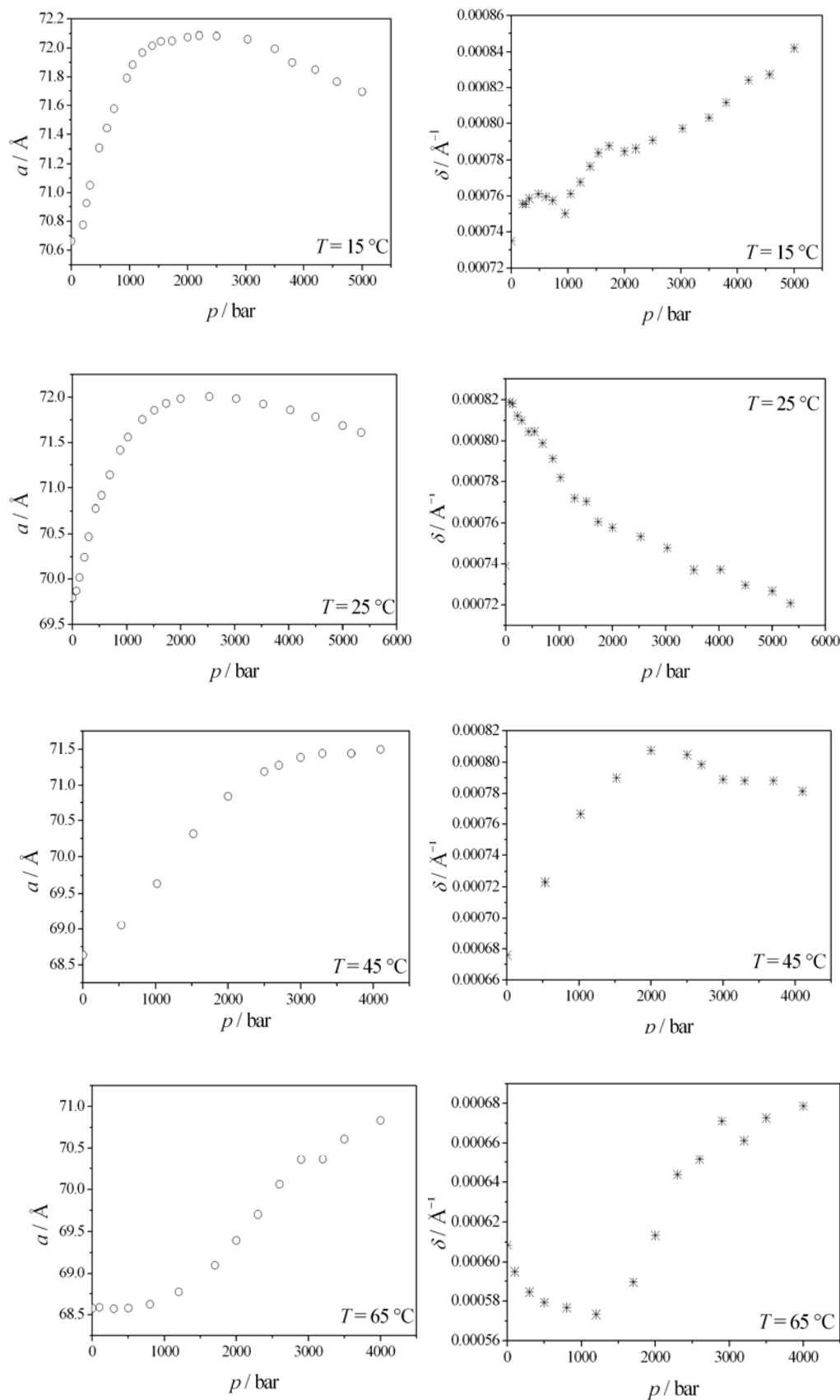
Figure 3.5 Lattice constants a and half-widths δ of second-order Bragg reflections of POPC/SM/Chol (33:33:33) 20% (w/w) in D_2O as a function of pressure, measured at different temperatures (15, 25, 45 and 65 °C).
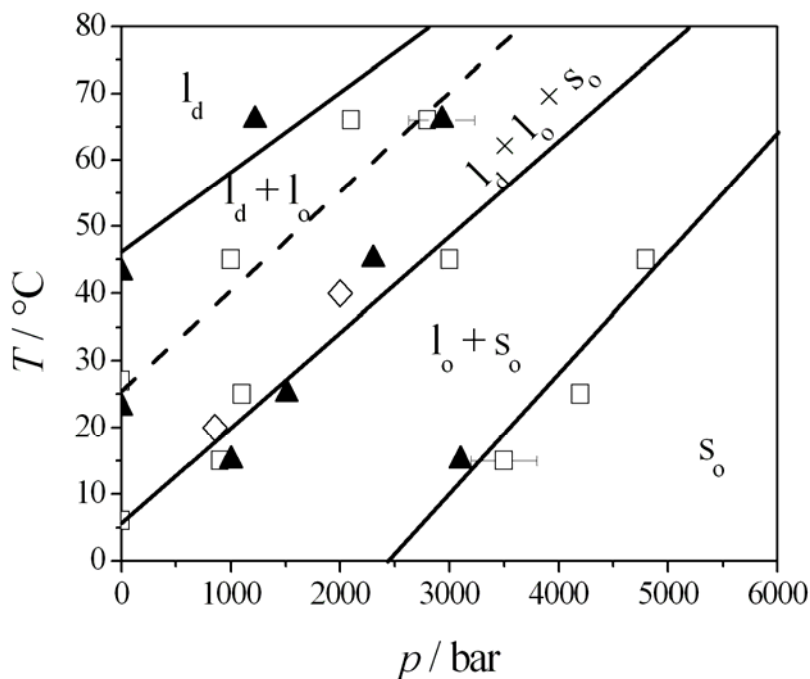
Figure 3.6 p, T-phase diagram of POPC/SM/Chol (33:33:33) in D_2O as obtained from FTIR (□), SAXS (▲) and in H_2O from the fluorescence spectroscopy (◊) data.

3.1.4   Conclusions

Figure 3.6 shows the p, T-phase diagram of the canonical raft mixture POPC/SM/Chol (33:33:33) over an extended temperature and pressure range, as obtained by the FTIR spectroscopy and SAXS data. At ambient pressure, FTIR spectroscopy, and SAXS detect a main transition at ~25 °C. It represents the passage from a region containing a gel phase into one which is completely fluid. This result is likewise supported by the peak at ~20 °C resulting from DSC and PPC data (Monika Khurana). The SAXS patterns indicate an additional transition at higher temperatures (~47 °C) probably into an all-l_d region. Besides, the CH_2 stretching frequency and the C=O stretching mode from the FTIR data depict a transition at ambient pressure and lower temperatures (~6 °C) pointing to the possible existence of a l_o + l_d + s_o-three phase region. The hypothesis of the existence of a three-component region, for such lipid raft mixtures, between the solid-liquid and the liquid-liquid phases is an important issue, which was already mentioned by many authors (DE ALMEIDA, 2003; SILVIUS, 1996; VEATCH, 2003). The existence of a three-phase region is strong supported in this study by the additional transitions, which are detected at different

temperatures upon increasing pressure. At 15 and 25 °C, the FTIR and SAXS measurements of the POPC/SM/Chol (33:33:33) mixture show two phase transitions one at lower and one at higher pressure, from $l_d + l_o + s_o$ to $l_o + s_o$ and to s_o, respectively. Moreover, at 45 °C the existence of further transitions is suggested by the FTIR data, from $l_d + l_o$ to the $l_o + l_d + s_o$ three-phase region to $l_o + s_o$. Finally, at ~5 kbar the system reaches the solid state. The complementary SAXS measurements from 1 bar up to 4 kbar , however, depict only one transition from $l_d + l_o + s_o$ to $l_o + s_o$ at this temperature. The transition expected at lower pressures from $l_o + l_d$ to the $l_o + l_d + s_o$ three-phase region was not clearly detectable. At 66 °C, both methods depict two transitions: the first one from l_d to $l_d + l_o$, and a second one from $l_d + l_o$ to the $l_o + l_d + s_o$ phase.

As expected, all phase transition lines are shifted to higher temperatures with increasing pressure. Within the experimental error, the corresponding slopes do not differ markedly.

3.2 Small-scale composition fluctuations and microdomain formation in lipid mixtures as revealed by small-angle neutron scattering

3.2.1 Introduction

In this part, different lipid mixtures are studied, using small-angle neutron scattering in combination with the H/D contrast variation as method. The aim is to observe heterogeneous membrane structure composed of sphingomyelin ($\rho \approx 0.3 \times 10^{10}$ cm^{-2}), cholesterol ($\rho \approx 0.2 \times 10^{10}$ cm^{-2}), and DOPC or POPC ($\rho \approx 0.3 \times 10^{10}$ cm^{-2}), in different amounts, and lipid composition fluctuations on a length scale from 1 to 200 nm. The composition of the H$_2$O/D$_2$O mixture for the dispersion of the vesicles, with a lipid mass fraction of about 15%, was adjusted so that the scattering length density of the solvent H$_2$O/D$_2$O was equal to that of a, hypothetical, homogeneous mixture of the lipid components.

Firstly, DOPC/SM/Chol (50:50) was studied at different cholesterol levels. As already depicted in chapter 1, lipid rafts are defined as distinct membrane domains which are resistant to detergent solubilisation. Thus, two different concentrations of the detergent Triton X-100 was added to examine this effect on the system DOPC/SM/Chol (33:33:33).

Secondly, the lipid mixture POPC/SM/Chol was chosen as a second system. In order to compare the different phases: all-fluid, fluid-fluid, and gel-fluid, different lipid ratios are measured. Recently, de Almeida *et al*. (DE ALMEIDA, 2003) applied fluorescence techniques to mixtures of PSM (palmitoylsphingomyelin), POPC, and cholesterol in different proportions. They determined partial binary phase diagrams for PSM/POPC ($s_o + l_o$ phase separation), POPC/Chol ($l_d + l_o$ phase separation), and PSM/Chol ($l_d + l_o$ and $s_o + l_o$ phase separation) by use of FRET. The ternary phase diagrams PSM/POPC/Chol ($l_d + l_o$, $l_d + s_o$, $l_o + s_o$, and $l_d + l_o$ + s_o phase separation) were also obtained at room temperature (23 °C) and 37 °C (physiological temperature). In this work, five concentrations of this mixture representing different phases were examined (Figure 3.11).

3.2.2   The system DOPC/SM/Chol

The lipid system DOPC/SM/Chol (50:50) was measured as a function of temperature at different levels of cholesterol. Figures 3.7(A) and 3.7(B) present the SANS data at 15 °C for DOPC/SM (50:50) , DOPC/SM/10 mol% Chol, and DOPC/SM/Chol (33:33:33) (~25 vol% D_2O). All the systems show strong scattering intensity in a Q range below ~0.1 $Å^{-1}$, corresponding to a real space dimension in the range from ~60 to ~2000 Å. The small-angle scattering pattern may also be analysed using fractal terminology. The concept of fractal geometry is often applied to describe systems showing irregular structures (WINTER, 1999). More details about fractals are given in chapter 2. The DOPC/SM (50:50) mixture exhibits a power-law slope of -2.7 ± 0.05 at low Q, which corresponds to a mass fractal dimension of $D_m = 2.7$. The slope decreases within the error upon addition to an DOPC/SM (50:50) solution of 10 and 33 mol% cholesterol, respectively. Figure 3.7(A) shows the log-log plot and the derived power-law exponent for the raft model mixture (-3.0 ± 0.05). The scattering intensity for the 10 mol% cholesterol containing lipid mixture is about twice as high as of the 33 mol% Chol mixture at low Q-values, indicating a higher concentration of fluctuating scattering centres. At 33 mol% the scattering intensity still presents composition fluctuations below 200 Å. At $Q = 9 \times 10^{-2}$ a Bragg reflection is observed, that corresponds to a mean lamellar d-spacing of 70 Å.

Figure 3.8 depicts the double logarithmic and the linear plot of the small angle scattering intensity $I(Q)$ for DOPC/SM/Chol (33:33:33) at selected temperatures (under H/D contrast matching conditions). The curves present similar scattering intensities at 15 and 25 °C, which decrease by about 20% at 45 °C and by 50% at higher temperatures (60 °C). At 60 °C the membrane is arranged in an almost completely fluid phase and, consequently, the scattering pattern has changed pointing to a different lateral organisation of the membrane at higher temperature. It is notable that the composition fluctuations of the raft-like lipid mixture exhibit an enormous stability over a temperature range of more than 40 °C.

Figure 3.9 shows an example of Ornstein-Zernike plot ($I(Q)^{-1}$ *vs.* Q^2) of the data. This plot is necessary to prove if critical fluctuations are present at the temperatures and concentrations measured. If critical fluctuations are present, then an extrapolation of the curve in the Ornstein-Zernike plot to $I(Q)^{-1} = 0$ on the $-Q^2$ axis will yield the correlation length of critical-like composition fluctuations. Over the temperatures and concentration conditions range covered no such critical-like spatial composition fluctuations were detected.

Figure 3.7 (A) Double-logarithmic plot and (B) linear plot of the small-angle scattering intensity *I(Q)* of the three systems DOPC/SM (50:50), DOPC/SM/10 mol% Chol, and DOPC/SM/Chol (33:33:33) at 15 °C (15 wt.% lipid aqueous dispersion, under H/D contrast matching conditions).
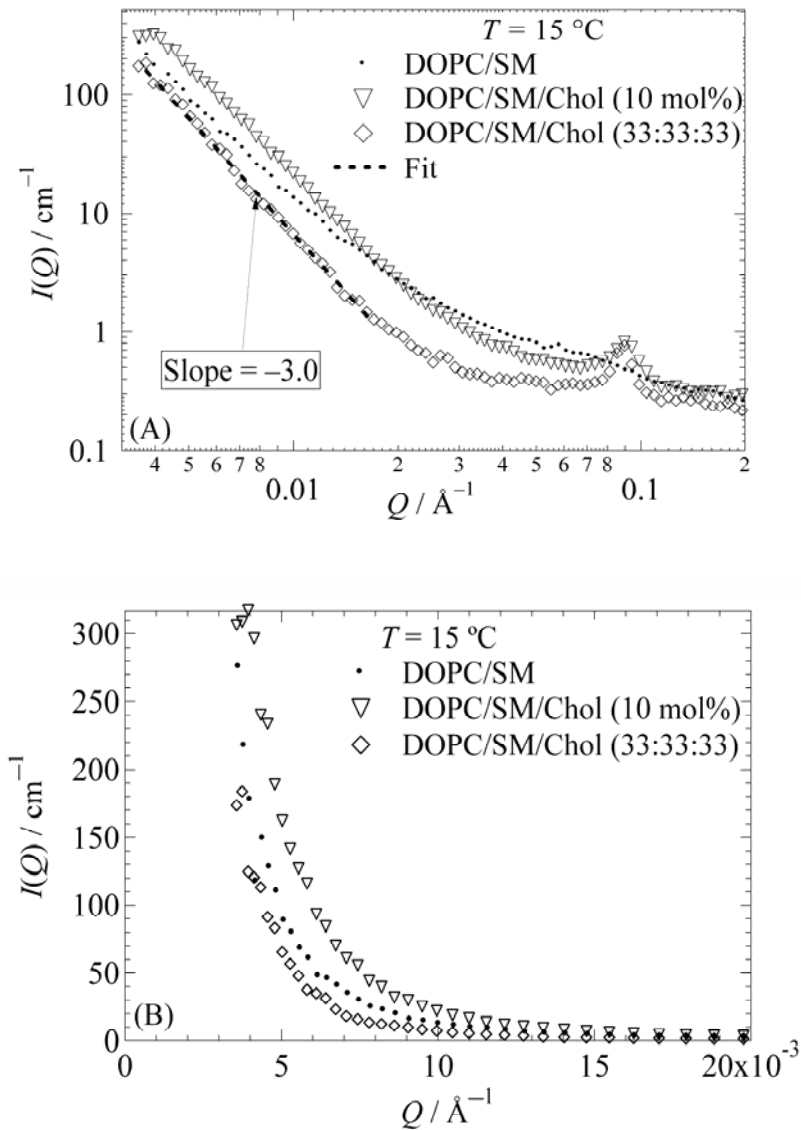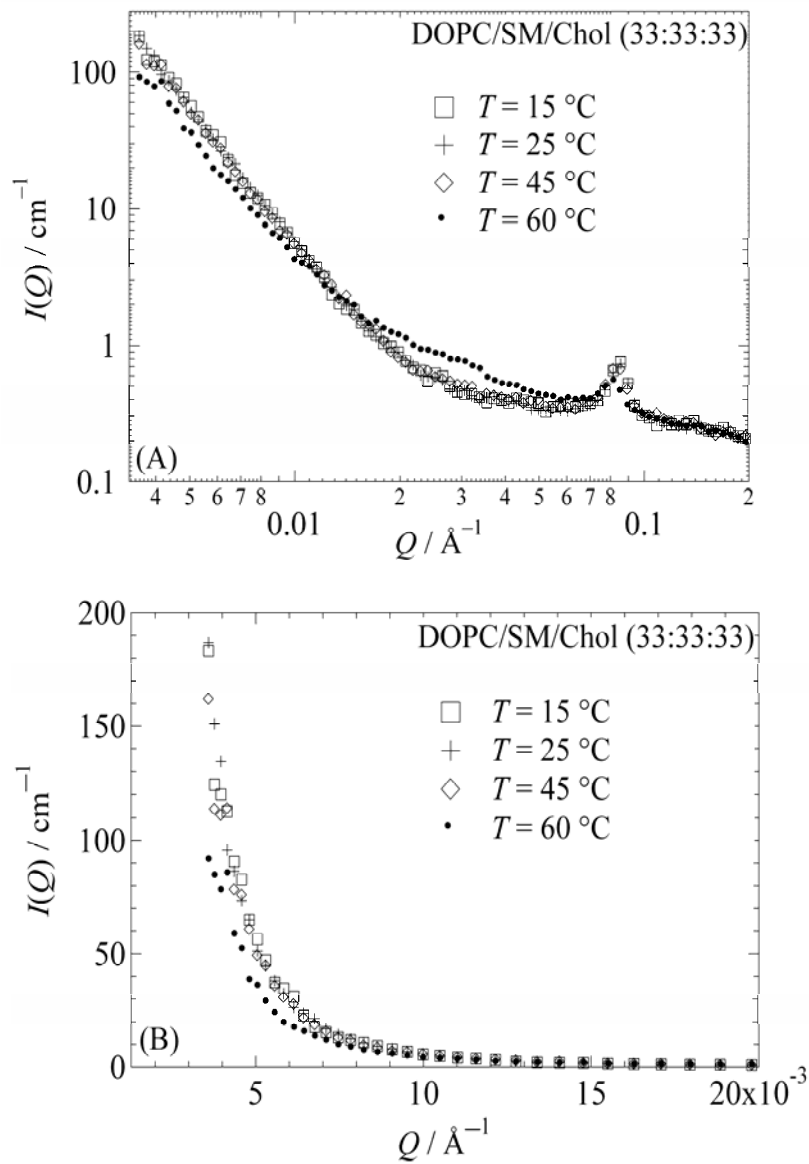
Figure 3.8 (A) Double-logarithmic plot and (B) linear plot of the small-angle scattering intensity $I(Q)$ of DOPC/SM/Chol (33:33:33) at selected temperatures (15 wt.% lipid aqueous dispersions, under H/D contrast matching conditions).
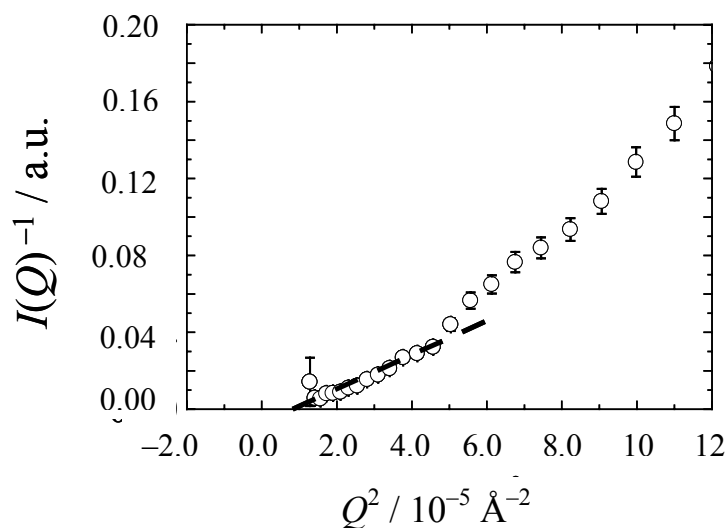
Figure 3.9 Ornstein-Zernike plot of the SANS curve of DOPC/SM/Chol (33:33:33) at 15 °C (15 wt.% lipid aqueous dispersion, under H/D contrast matching conditions).

Insolubility of lipid mixture like rafts is observed in detergents like Triton X-100. The effect of two different concentrations of this detergent (0.035 M (~2%) and 0.175 M (~5%)) on the lipid system DOPC/SM/Chol (33:33:33) was detected at room temperature. Figure 3.10 represents the data comparing the power-law scattering of the lipid mixture with and without the added detergent. The scattering intensity is largely hold adding 2% Triton X-100, whereas $I(Q)$ decreases by a factor of 2 adding 5% detergent. That might suggest that the population of smaller domains shrink, thus the upper Q-limit (Q ~$1.5 \cdot 10^{-2}$ Å^{-1}) shifts to lower values. Hence, the addition of Triton X-100 leads to a depletion of smaller domains, probably owing to a reduction in the interphase boundary line energy density, i.e., the line tension between domains. This might mean that the small - possibly ordered - domains are disintegrated but the large ones remain, or that the small domains grow or coalesce to large domains.

Figure 3.10 Small-angle scattering intensity of the DOPC/SM/Chol (33:33:33) mixture (15 wt.% lipid aqueous dispersions, under H/D contrast matching conditions), and the lipid mixture with 0.035 M and 0.175 M of the detergent Triton X-100.
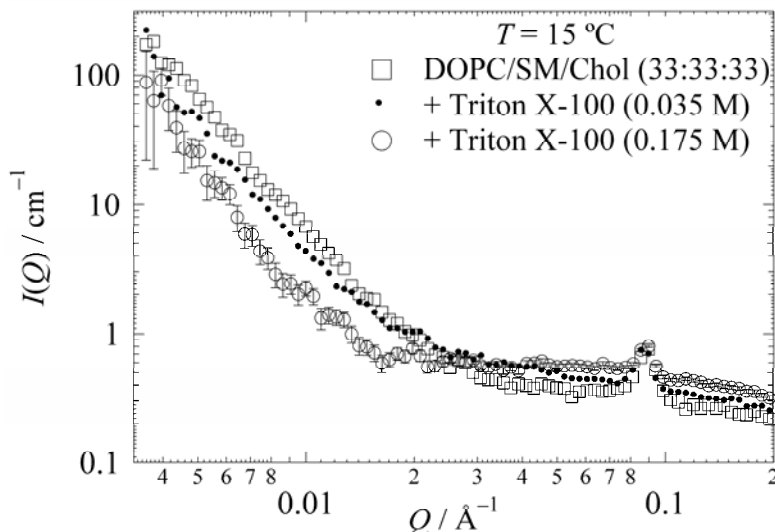
3.2.3   The system POPC/SM/Chol

The system POPC/SM/Chol was measured at $T \approx 25$ °C at five different lipid ratios corresponding to four different regions ($l_d + l_o$, $l_o + s_o$, all-l_d, all-l_o) of the phase diagram shown in Figure 3.11.

Figure 3.12 presents the linear plot of the SANS data of the POPC/SM/Chol mixture in different proportions in a contrast matched H_2O/D_2O solvent mixture. For the systems POPC/SM/Chol (35:5:60) (~12 vol% D_2O) and POPC/SM/Chol (90:5:5) (~13 vol% D_2O), corresponding to an all-l_o, and all-l_d phases, respectively, zero scattering intensity is almost observed at Q below ~0.1 Å^{-1} corresponding to real space dimension of ~60 to ~2000 Å, and the log-log plot of the scattering intensity does not exhibit power-law slope. A small increase of $I(Q)$, though, is detected at the lowest momentum transfer, probably due to the scattering of multilamellar vesicles, which cannot be fully contrast-matched. In contrast to this, POPC/SM/Chol (80:5:15) (~13 vol% D_2O) and POPC/SM/Chol (33:33:33), both in the $l_o + l_d$ phase, show a higher scattering, intensity which increases by 30 cm^{-1} for the mixture indicated as (c) in Figure 3.11, which is close to the line to the all-disordered liquid phase, and by ~110 cm^{-1} in the case of the equimolar POPC/SM/Chol mixture (Figure 3.12). The latter presents a higher fraction of fluctuating scattering centres. In this case, concentration fluctuations give rise to a power-law scattering over a wide Q-range extending down to ~3·10^{-2} Å^{-1}, i.e., over a length scale of 200 – 1800 Å. The power-law exponent derived from

the log-log plot (Figure 3.13) is −2.8 ± 0.3, which corresponds to a mass fractal dimension of D_m = 2.8. The scattering intensity at low Q-values of POPC/SM/Chol (25:65:10) (~15 vol% D_2O), corresponding to a l_o + s_o lipid mixture, is about 4 times the value of the equimolar mixture, pointing to a different lateral organisation of the membrane. The power-law exponent is in this case −3.0 ± 0.1. At Q = 8·10^{-2} Å^{-1}, a Bragg reflection is observed, which corresponds to a lamellar d-spacing of the multilamellar lipid vesicles of 70 Å.

Figure 3.14 shows an example of an Ornstein-Zernike plot ($I(Q)^{-1}$ $vs.$ Q^2) of the system POPC/SM/Chol (33:33:33). The data obtained from this method reveal the absence of critical-like concentration fluctuations for the chosen lipid ratios. Through extrapolation of the curve to zero on the $-Q^2$ axis the correlation length, may be obtained, which gives information about critical-like spatial composition fluctuations. At the temperature and concentrations used conditions, no critical-like spatial composition fluctuations are detected.
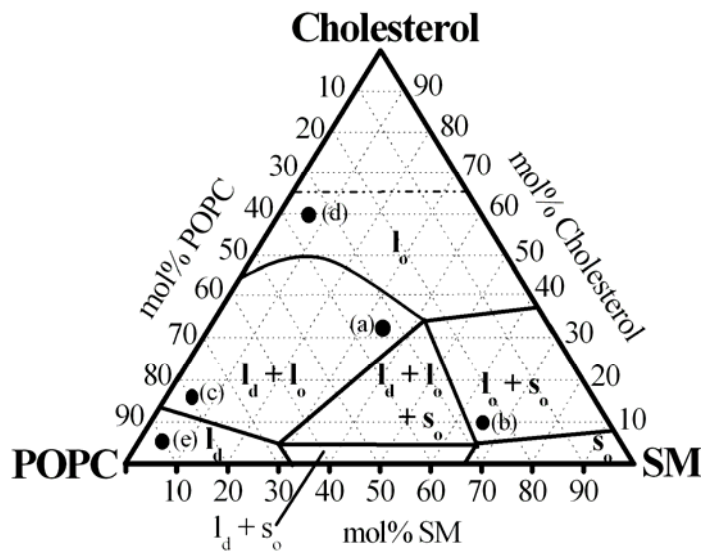
Figure 3.11 POPC/SM/Chol phase diagram at 23 °C. The circles are experimental points. Each vertex represents a pure component. The dash horizontal line for χ_{chol} = 0.66 represents the cholesterol solubility limit of the lipid bilayer. The value was chosen as the limit determined for several phosphocholin at room temperature, but it should be noted that the value can be different for a lipid mixture, i.e. the line may not be horizontal, there can be temperature variations, and it was not determined for SM. The labelled regions of the diagram are: l_d (liquid disordered), l_o (liquid ordered), s_o (solid ordered) (adopted from DE ALMEIDA, 2003).
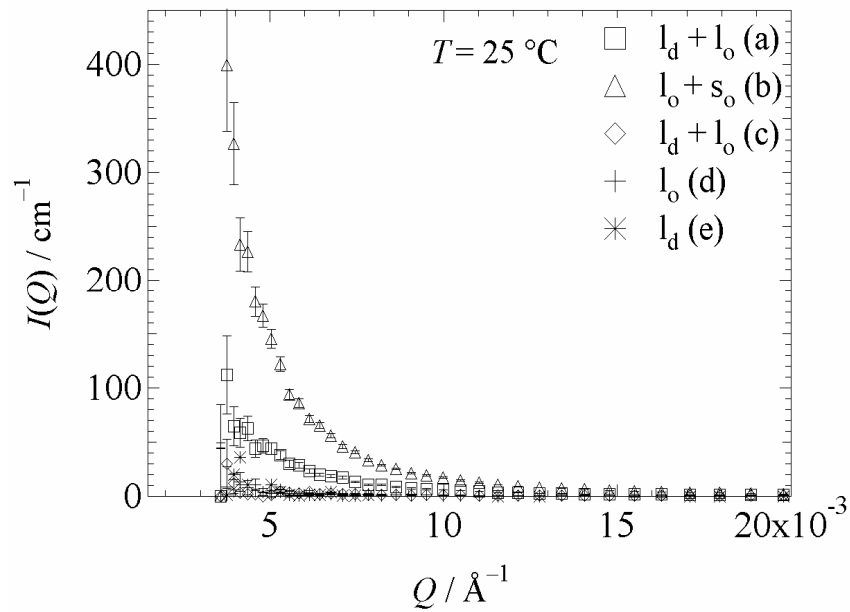
Figure 3.12. Linear plot of the small-angle scattering intensity $I(Q)$ of the lipid mixture POPC/SM/Chol at various lipid concentrations at 25 ^{o}C (15 wt.% lipid aqueous dispersions, under H/D contrast matching conditions).

Figure 3.13 Double-logarithmic plot of the small-angle scattering intensity $I(Q)$ of the lipid mixture POPC/SM/Chol at various lipid concentrations at 25 °C (15 wt.% lipid aqueous dispersions, under H/D contrast matching conditions).
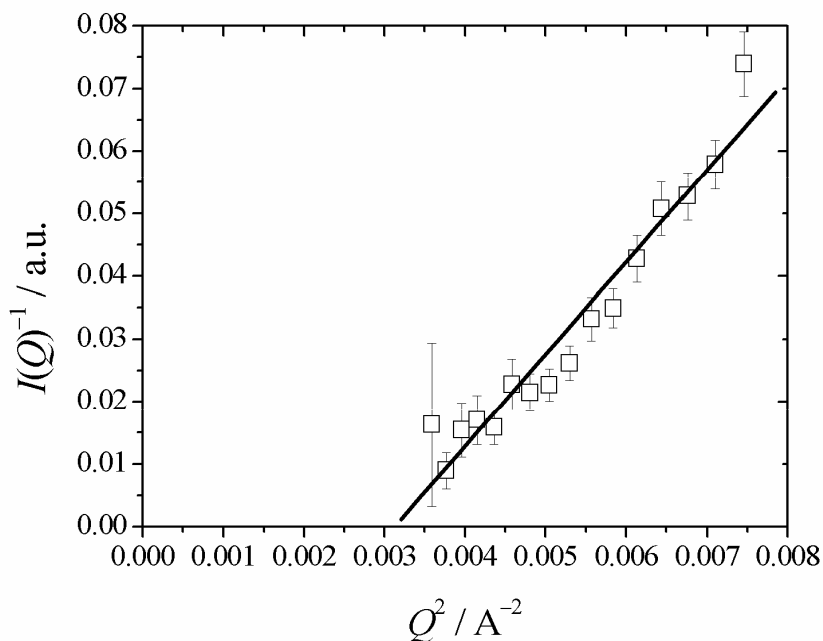
Figure 3.14 Ornstein-Zernike plot (plot of $I(Q)^{-1}$ *vs.* Q^2) of the SANS curve of POPC/SM/Chol (33:33:33) at 15 °C (15 wt.% aqueous lipid dispersion, under H/D contrast matching conditions).

3.2.4   Conclusions

In summary, two different lipid systems were investigated: DOPC/SM (50:50) with different levels of cholesterol and the effect of adding the detergent Triton X-100, and POPC/SM/Chol at different lipid ratios. The mixtures reveal large-scale composition fluctuations with irregular shapes, which may be described taking in consideration concepts of fractal geometry. The typical model-like raft mixture consisting of DOPC(POPC)/SM/Chol (33:33:33) shows a power-law scattering behaviour of its scattering intensity with an exponent of ~3.0. The data indicate the existence of composition fluctuations over a wide range of momentum transfer which correspond to a distribution of independent droplets of one phase in the other with droplet sizes ranging from 200 to 2000 Å. These results demonstrate the existence of microdomains of the size of several tens of nanometres.

3.3   Effects of pressure on the lateral organization and topology of lipid vesicles – a two-photon excitation fluorescence microscopy and SAXS study –

3.3.1   Introduction

In this chapter, structure, lateral organization and changes in morphology of GUVs composed of different lipid mixtures are studied using the following methods: two-photon excitation fluorescence microscopy and small-angle x-ray scattering. The pressure dependent experiments were carried out in the two-photon microscopy using a sample cell made from a thin fused silica capillary. The use of Laurdan as fluorescence label permits to follow the lipid phase state by calculating the *GP* histograms of the single vesicles and extracting their average values. Upon increasing pressure, the phase transitions are accompanied by characteristic changes in vesicle size, budding and fission of lipid material. Particularly for the lipid mixture POPC/DLPC (50:50), the decompression cycle shows a variety of shape transitions of the vesicles from spherical to ellipsoidal to polygonal, accompanied by strong fluctuations of the membrane surfaces. On the contrary, in the lipid systems containing 31 and 33 mol% cholesterol, like the model lipid rafts DOPC/DPPC/Chol (34.5:34.5:31) and DOPC/SM/Chol (33:33:33), due to the presence of cholesterol, shape transitions of the GUVs are drastically stabilized, though they continue to show budding and fission.

The changes in *GP* average values are compared to pressure dependent SAXS data on the same lipid mixtures in multilamellar vesicles.

3.3.2   Fluorescence microscopy

POPC/DLPC During the compression cycle from 1 up to 2000 bar at 50-100 bar intervals (*T* ≈ 20 °C) the GUVs composed of POPC/DLPC (50:50) maintain their spherical shape. By increasing the pressure, the average *GP* values increase continuously indicating a tighter packing of the lipid chains, which are fluid-like state at ambient pressure conditions. At 2000 bar the *GP* reaches the value of 0.55 (Figure 3.15), a plateau, however, is not reached, i.e. the system is not completely in the gel phase yet, as it is also shown by the SAXS measurements described later.
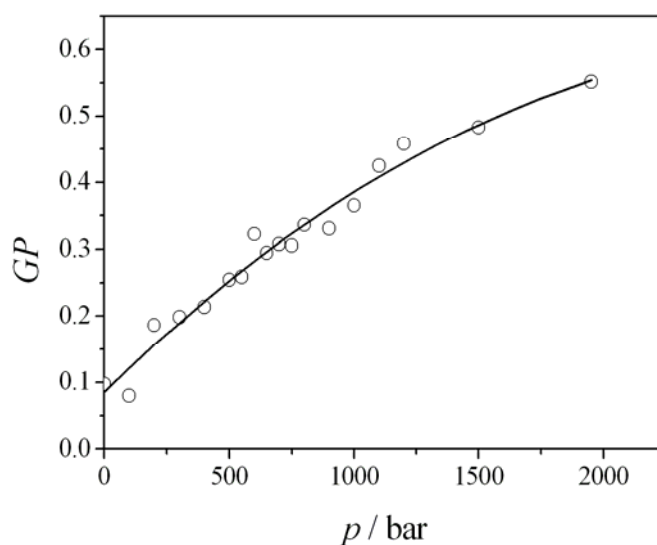
Figure 3.15 *GP* average value of the lipid mixture POPC/DLPC (50:50) as a function of pressure during a compression cycle (*T* = 20 °C). Upon increasing pressure, an increase in *GP* value is detected (by about 0.5 units), reaching the value of 0.55, indicating the transition to a more ordered structure.

The vesicles show a decrease of radius, area, and volume during the compression process by ~19%, 28% and 56%, respectively. Figure 3.16 depicts an example of these changes for one vesicle. The changes of the vesicle diameters are probably primarily due to the leakage of water, which can pass the membrane. During the decompression cycle it was not possible to conduct quantitative analysis of changes in diameter of the GUVs anymore, because of the continuously changes in the shape of the vesicles. In this case, although water will slowly permeate across the membrane, rapid changes in volume cannot be rapidly compensated and changes in shape are needed to account for the difference in volume-surface area caused by the change in pressure.

The main focus of interest in studying this system is the phenomenon of budding followed by fission and the changes in morphology of the GUVs, the latter process mostly taking place upon decreasing the pressure. During the compression cycle spherical-polygonal-ellipsoidal shape changes in the vesicles are not observed. However, upon increasing pressure budding is initiated. Figure 3.17 depicts an example of budding which is observed upon pressurization. Until 200 bar, the GUV retains its spherical shape. Increasing pressure by ~50

bar leads to the growth of a bud, which develops upon further pressurization, becoming a vesicle and disconnects from the parent vesicle at ~400 bar.

As soon as the pressure is reduced again from 2000 to 1 bar, the vesicle follows a sequence of different shapes: spherical-ellipsoidal-polygonal (Figure 3.18). This observation is accompanied by permanent fluctuations of the membrane surfaces. The shape transition from a spherical to an ellipsoidal shape occurs at ~1400 bar. At that pressure, pronounced regions with different *GP* values are induced. In particular at the edges of the vesicle surfaces, higher *GP* values are observed. At ~1100 bar the vesicle shape becomes completely instable and the membrane surface fluctuates steadily. This phenomenon is accompanied by fission.

During the decompression cycle, water flows across the bilayer outwards and this water flow can drag some lipid molecules from the inner to the outer monolayer. An increased number of lipid molecules in the outer monolayer could lead to a tendency of the bilayer to bend and to form a bud. In these experiments budding induced by a redistribution of lipids across the bilayer cannot be distinguished from budding induced by intramembrane domains (JÜLICHER, 1996). As soon as budding occurs, the original vesicle will loose area. If many buds are formed, this loss of area can be detected even if the buds themselves are invisible in fluorescence microscopy.
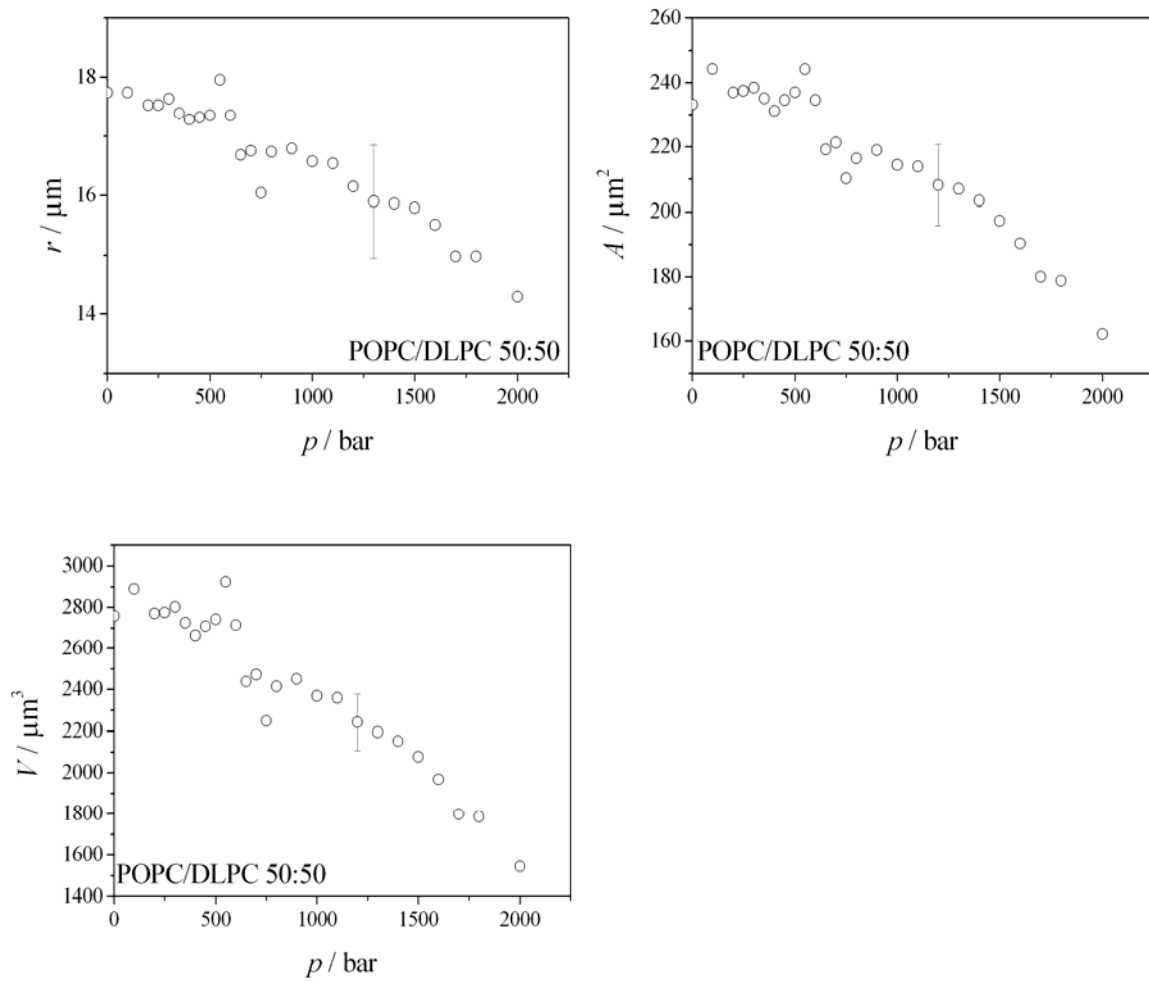
Figure 3.16 The approximate mean vesicle radii of the lipid mixture POPC/DLPC (50:50) ($T = 20$ °C) as determined from the vesicle cross-sections. The surface areas and volumes were calculated assuming ellipsoidal shapes of revolution.
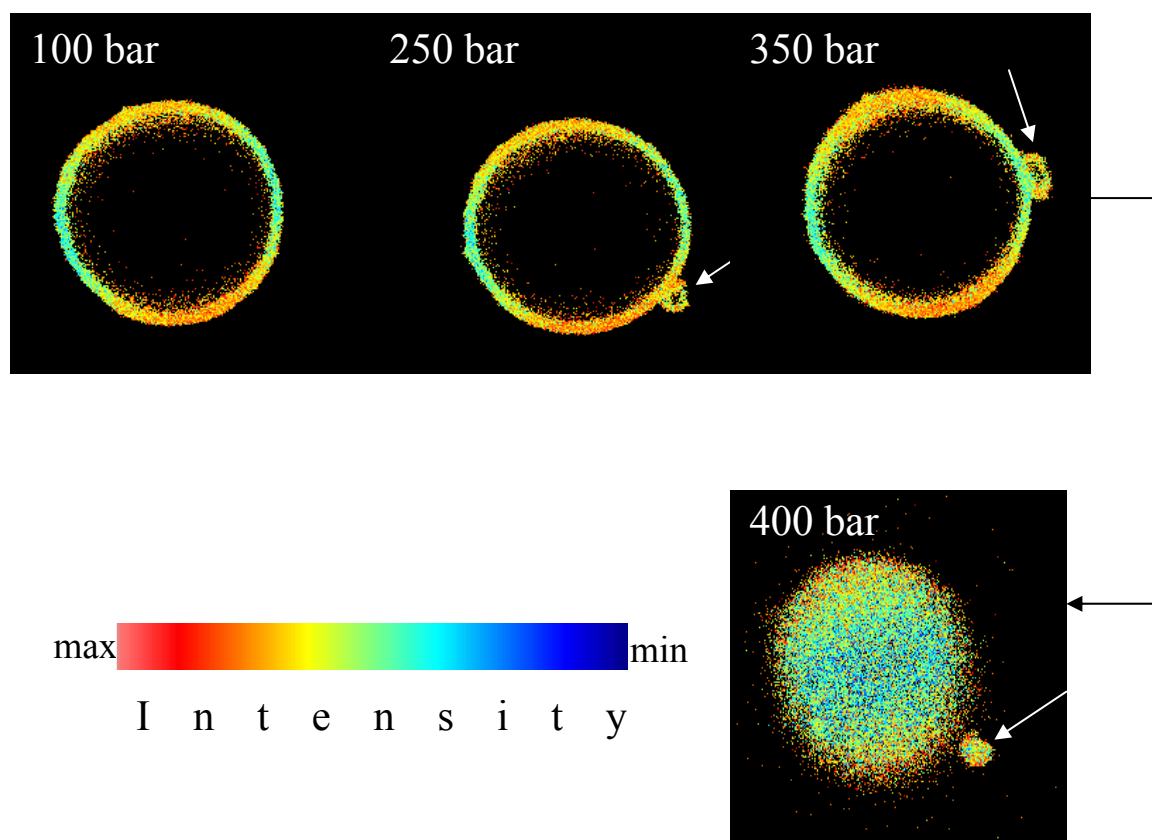
Figure 3.17 Two-photon excitation fluorescence intensity images of Laurdan-labelled GUVs of the system POPC/DLPC (50:50) at 20 °C taken during the compression cycle. At 250 bar, a bud develops, which grows upon further pressurization. At ~400 bar fission occurs. The white arrows indicate budding and fission processes.
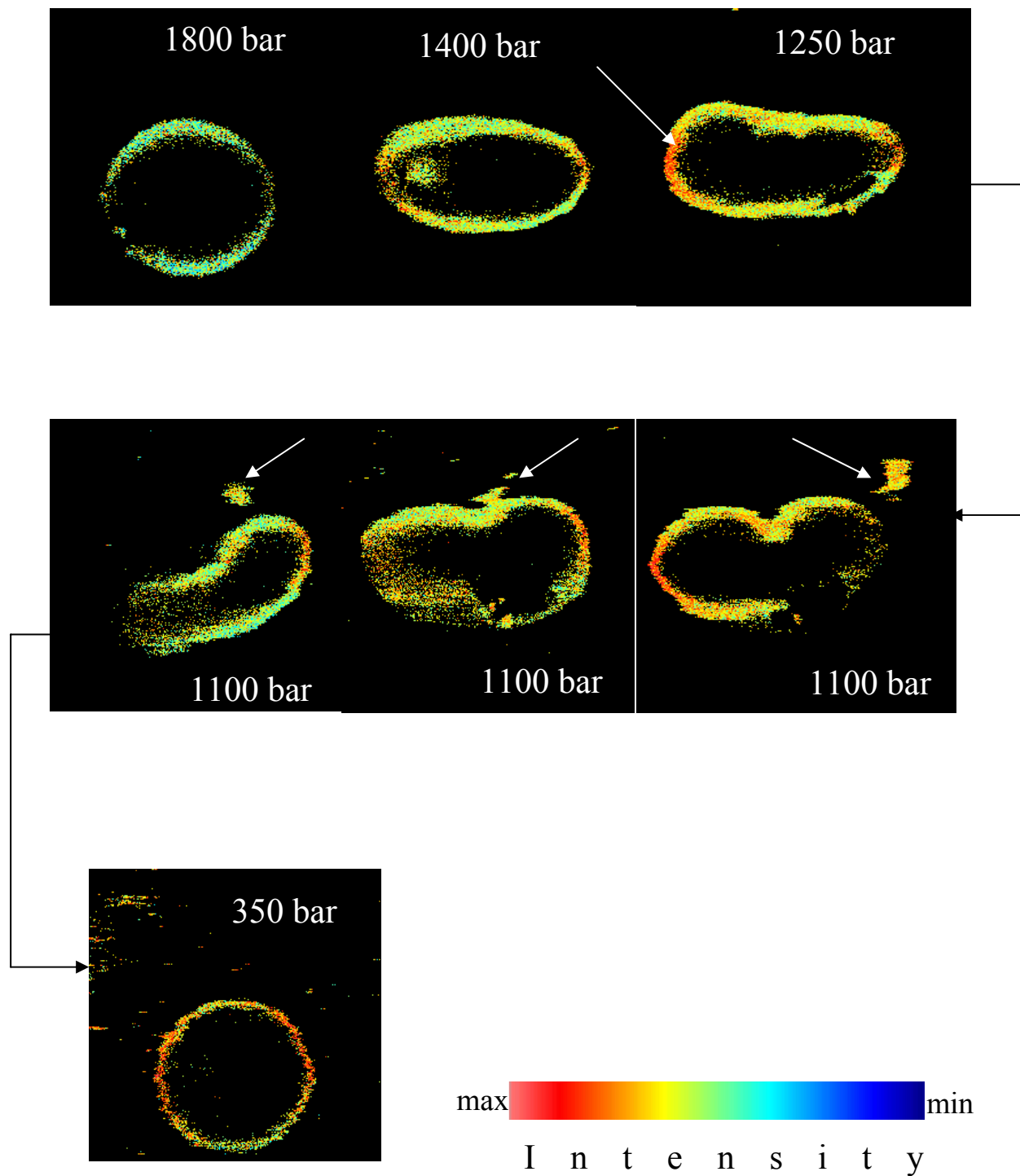
Figure 3.18 Two-photon excitation fluorescence intensity images of Laurdan-labelled GUVs of the system POPC/DLPC (50:50) at 20 °C taken during the decompression cycle. The white arrow at 1250 bar shows a high *GP* intensity (gel) region. The white arrows at 1100 bar indicate conditions where budding of small vesicles and pinching-off of lipid material occur.

Raft systems Pressure experiments with GUVs containing DOPC, SM (DPPC) and cholesterol in levels of 31 and 33 mol%, also visualized by the membrane fluorophore Laurdan, were carried out from 1 to 2700 bar. Figures 3.19 and 3.20 show vesicles of DOPC/DPPC/Chol (34.5:34.5:31) lipid mixture at selected pressures. Images of GUVs composed of DOPC/SM/Chol (33:33:33) are depicted in Figure. 3.21. *GP* images of the GUVs having the same lipid composition may look different. In the system DOPC/DPPC/Chol (34.5:34.5:31) the first vesicle (Figure 3.19) shows homogeneity on the µm spatial resolution, while the second one in Figure 3.20 clearly suggests the coexistence of two phases. However, since the average *GP* values of both vesicles are similar (Figure 3.22 (A)) and knowing that if in the case that the lipid domain and the pixels are of similar size, or the size of the domains are smaller, the vesicles will show a homogeneous fluorophore distribution only, one might conclude that in both vesicles domains may be present of different sizes, however. (PARASASSI, 1995; PARASASSI, 1998). All the vesicles studied show a decrease in the diameter with increasing pressure (Figure 3.23). The decrease of cross-sectional area and volume of the vesicles with the same lipid composition during the compression cycle are quite different from each other. For example, the two GUVs, composed of DOPC/DPPC/Chol (34.5:34.5:31) show a decrease by 34% and 12% in area and by 47% and 18% in volume, respectively, if compressed from 1 bar up to 2000 bar. Instead, upon pressurization for GUVs composed of DOPC/SM/Chol (33:33:33), we determine a decrease by 12% and 18% in area and volume, respectively. All the changes are irreversible, i.e., upon decompression the original values are not retained, which is due to the irreversible loss of lipid material upon pressurization.
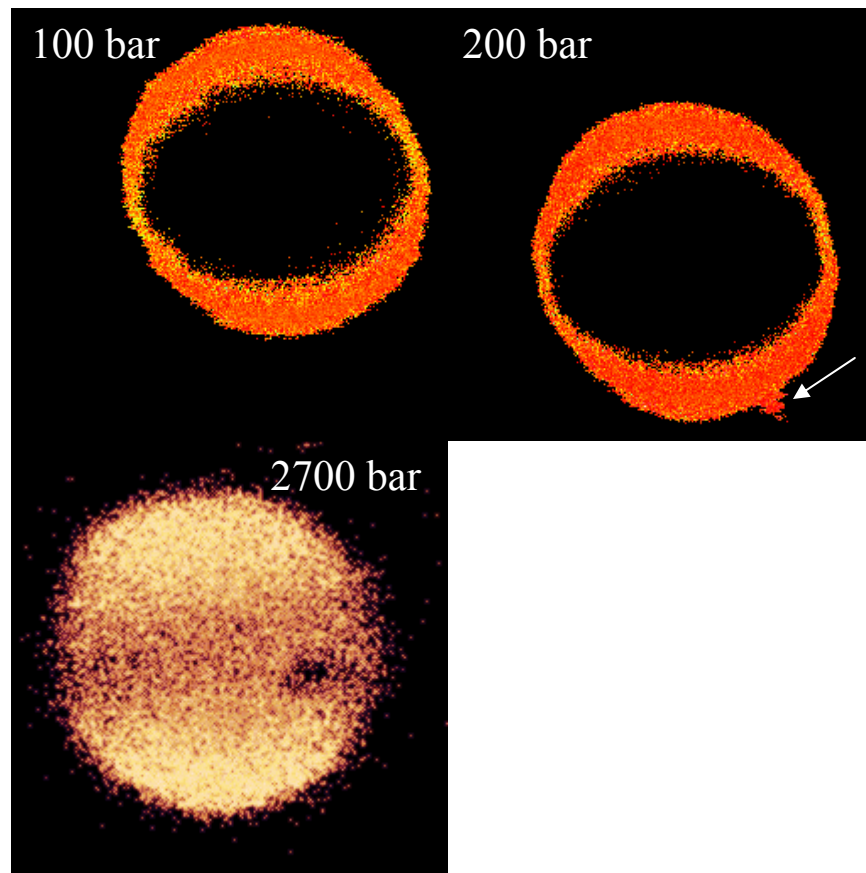
Figure 3.19 *GP* images of the equatorial section of a GUV (vesicle I) composed of DOPC/DPPC/Chol (34.5:34.5:31) at 100, and 200 bar (*T* = 20 °C). The two-photon excited fluorescence intensity image of the Laurdan-labelled GUV at 2700 bar reveals that domains exist even at these high pressure conditions.
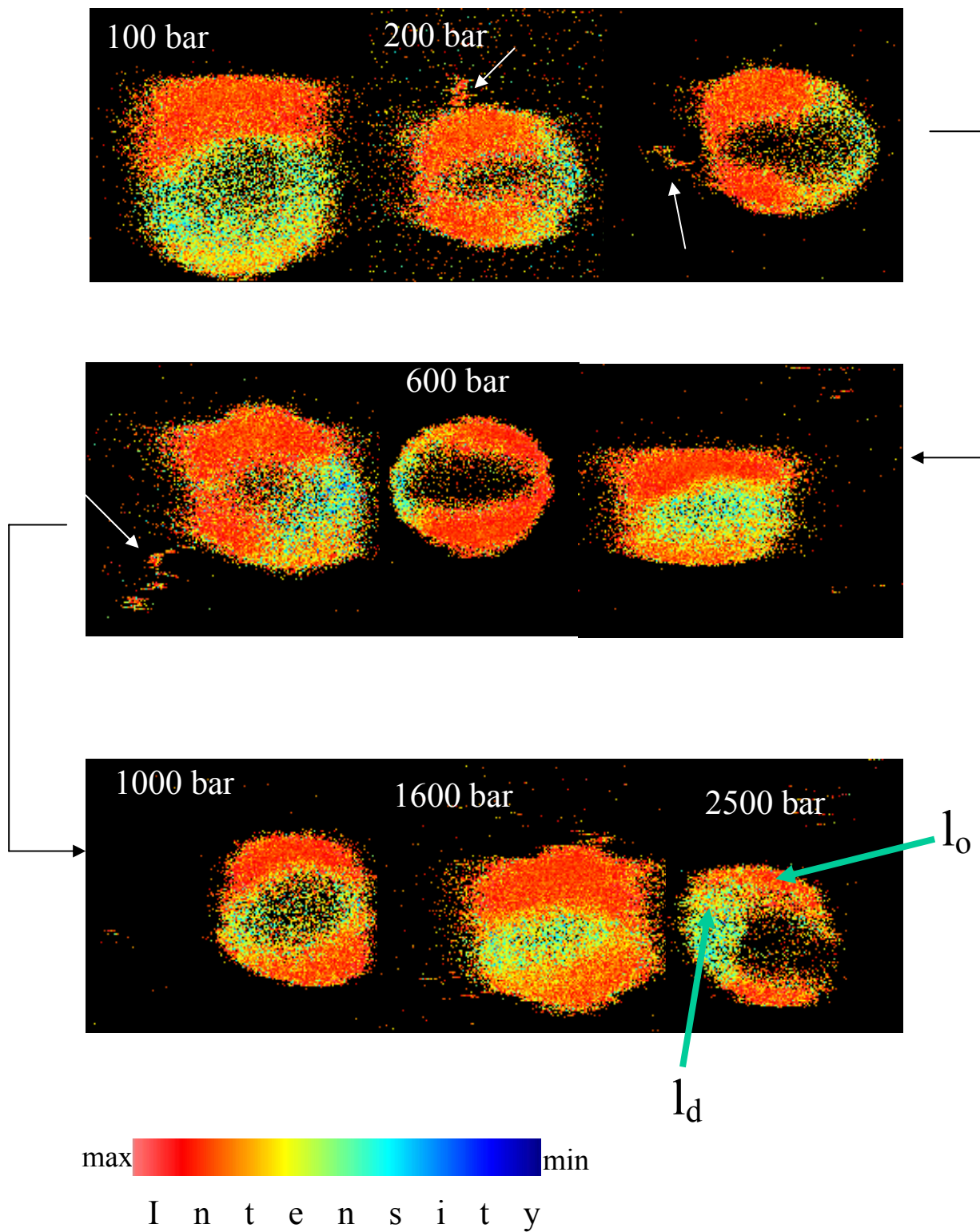
Figure 3.20 *GP* images of another GUV (vesicle II) composed of DOPC/DPPC/Chol (34.5:34.5:31) at selected pressures (*T* = 20 °C). The *GP* images are taken at the equatorial section for the pressures at 200, 600 and 2500 bar and at the top of the GUV for the other pressures. The white arrows indicate conditions where budding of small vesicles and loss of lipid material occur.
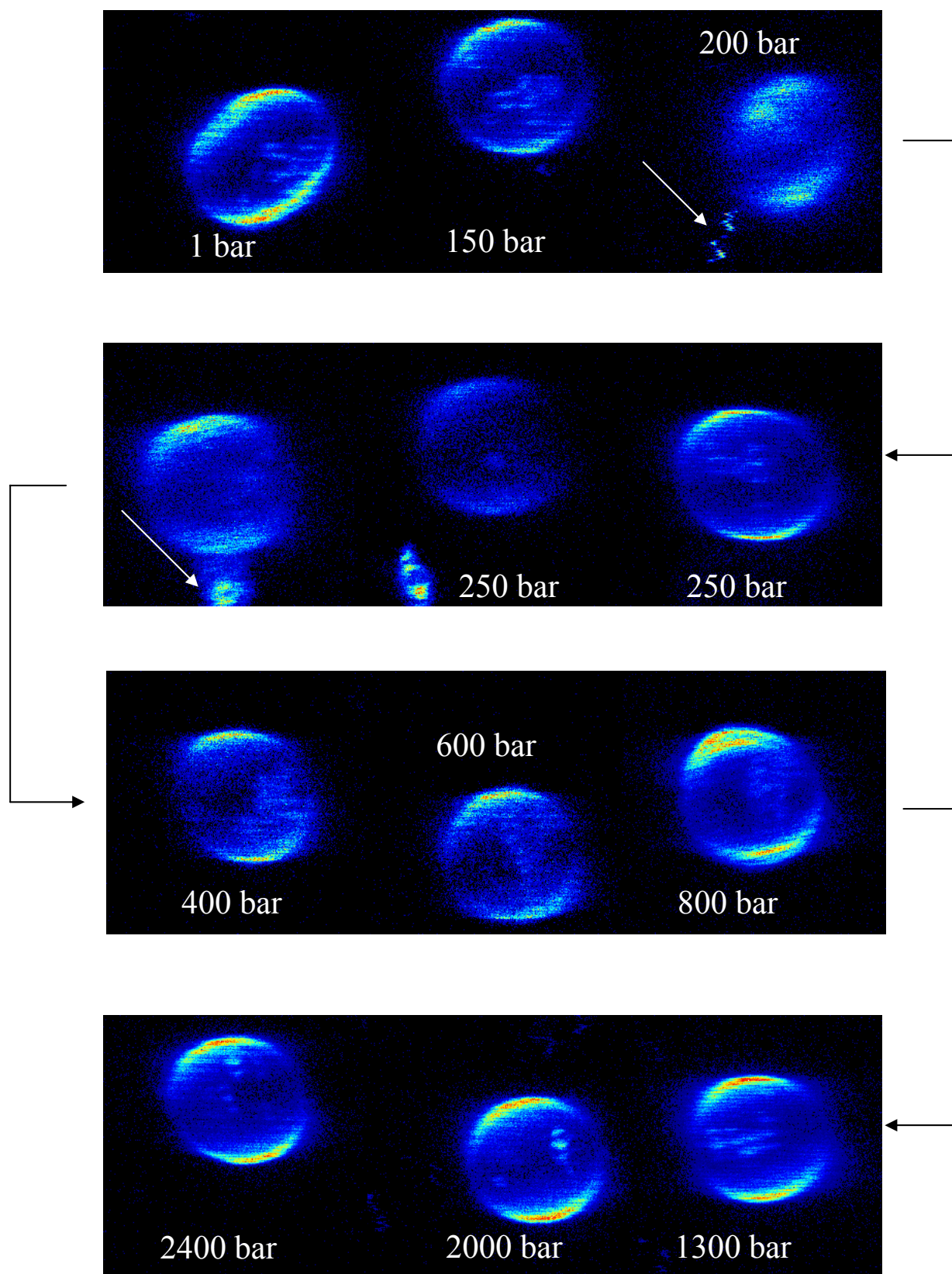
Figure 3.21 Two-photon excitation fluorescence intensity images of a Laurdan-labelled GUV composed of DOPC/SM/Chol (33:33:33) at selected pressures (T = 20 °C). The images are taken at the equatorial section. The white arrows indicate conditions where budding of small vesicles and loss of lipid material occur.
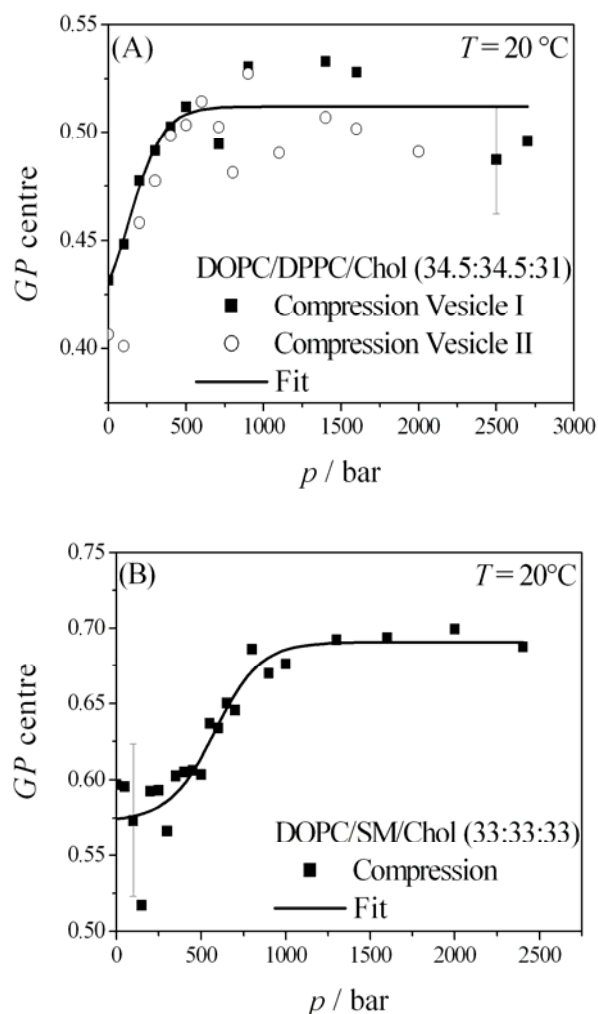
Figure 3.22 Average *GP* value of the lipid mixture (A) DOPC/DPPC/Chol (34.5:34.5:31) and (B) DOPC/SM/Chol (33:33:33) as a function of pressure during a compression cycle (*T* = 20 °C). Upon increasing the pressure, an increase in *GP* value was detected (by about 0.1 units for both systems), which levels off around 1 kbar, indicating the transition to a more ordered structure.

The white arrows in Figures 3.20 and 3.21 indicate conditions for budding of small vesicles and fission of lipid material. The detached lipid material always presents high *GP* values, which suggests that the daughter vesicles are essentially made of liquid-ordered, raft-like domains. Budding phenomenon is mostly observed at pressure conditions of about 200-300 bar, in the range in which the lipid system reaches a slightly more ordered structure. Upon increasing the pressure 1 up to ~2500 bar an increase by ~0.1 units in *GP* value is

detected, which levels off around 1 kbar (Figure 3.22). The *GP* histograms are fitted with a bandfitting procedure using two Gaussian lineshape functions. Figures 3.24(A) and 3.24(B) depict the corresponding *GP* distributions. Note that the *GP* values of the two bimodal distributions fall between *GP* values typical of ordered (l_o) and liquid-crystalline phases (DIETRICH, 2001). Upon increasing the pressure, the *GP* histogram fit remains bimodal and at high pressure (~2.7 kbar) the GUVs still exhibit coexisting domains (Figure 3.20). As shown in Figure 3.24(C), the amount of l_d-phase for GUVs composed of DOPC/DPPC/Chol (34.5:34.5:31) decreases by ~60% over the whole pressure range covered, whereas the amount of l_o-phase increases concomitantly. The amount of more ordered phase in the system DOPC/SM/Chol (33:33:33) is larger by only 23% at 1 bar and at 20 °C, i.e. the system has already a more ordered structure as we can see from the *GP* values (Figure 3.24(D)).

Flabbiness of the vesicles, as observed in GUVs composed of POPC/DLPC (50:50), is not noticed anymore in the typical lipid rafts model. The high level of cholesterol (>30 mol%) increases the conformation order of the lipid membranes and decreasing pressure only leads to fast spherical-ellipsoidal shape transition.
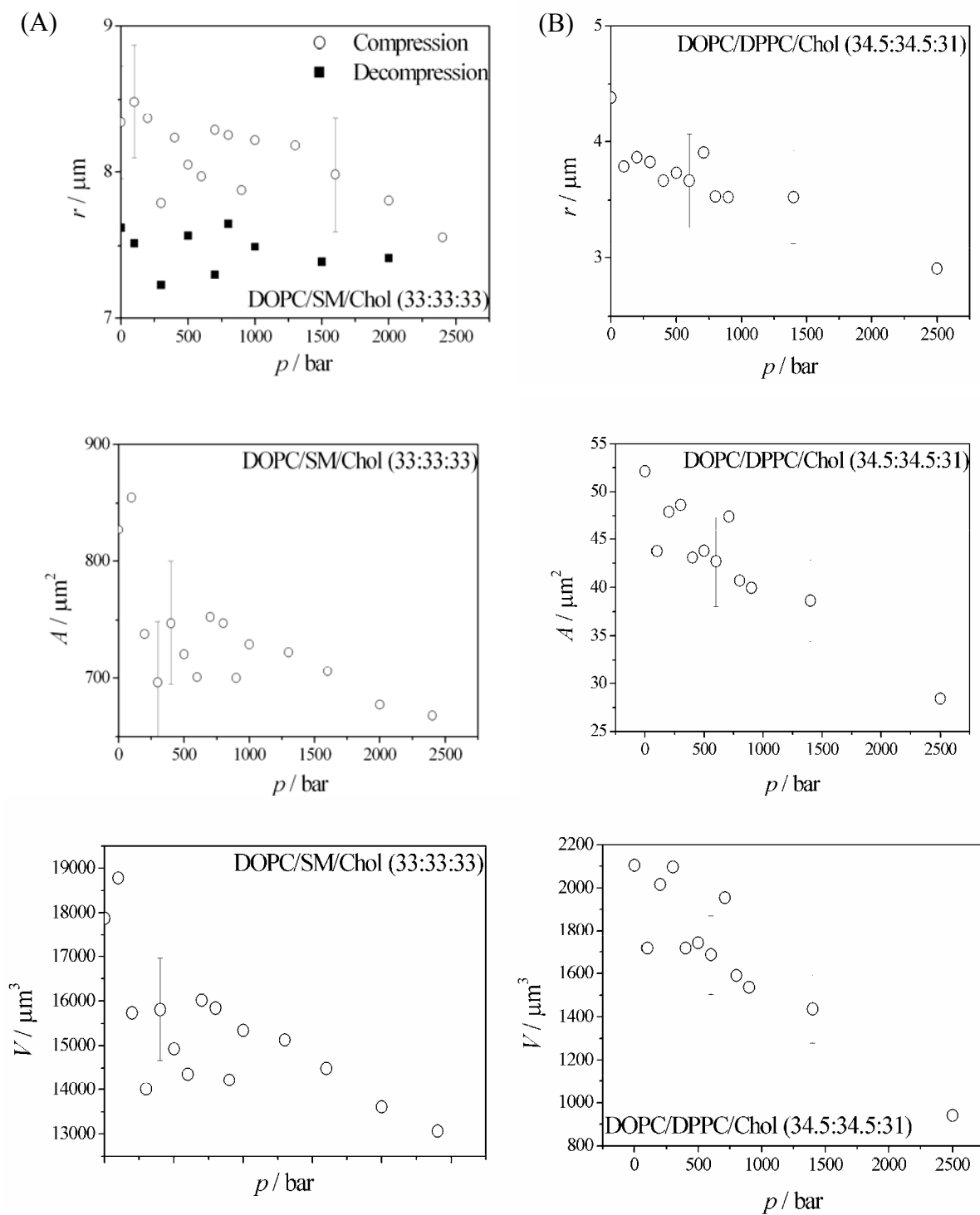
Figure 3.23 The approximate mean vesicle radii of the lipid mixture DOPC/SM/Chol (33:33:33) (A) and DOPC/DPPC/Chol (34.5:34.5:31) (B) as determined from the vesicle cross-sections. The surface areas and volumes were calculated assuming ellipsoidal shapes of revolution.
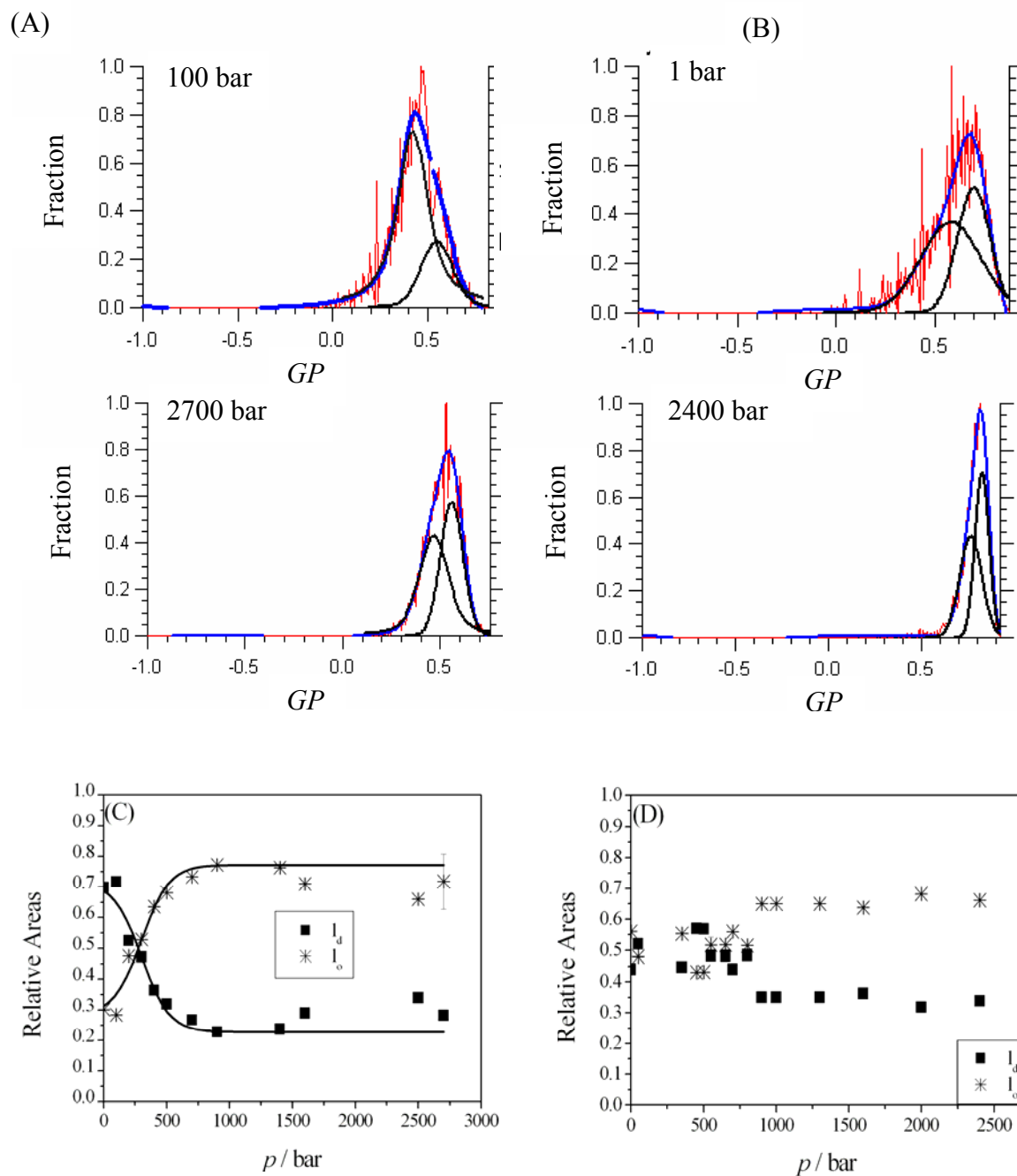
Figure 3.24 *GP* histograms of the lipid mixture (A) DOPC/DPPC/Chol (34.5:34.5:31) and (B) DOPC/SM/Chol (33:33:33) and the corresponding relative areas of l_o and l_d phases ((C) and (D)) as a function of pressure. The *GP* histograms were fitted with a bandfitting procedure using Gaussian lineshape functions. Figures 3.24(A) and 3.24(B) show the *GP* distribution with the two bands chosen. Note that the values in the two bimodal distributions fall between *GP* values typical for ordered (l_o) and liquid-crystalline (l_d) phases (DIETRICH, 2000).

3.3.3 Synchrotron small-angle x-ray scattering

DOPC/DPPC/Chol   The positions of Bragg reflections in the small-angle scattering region were analyzed to determine the topology of the lipid mesophases and the lattice constants of the corresponding structures. SAXS diffraction patterns at 20 °C from 1 bar up to 3000 bar at 300-400 bar intervals are depicted in Figure 3.25(A). The lamellar lattice constant *a* of the second order Bragg reflections is plotted for this temperature as a function of pressure in Figure 3.25(B). At all pressures, the Bragg reflections display ratios of diffraction spacing of 1:2, which are typical of lamellar phases. Two lipid structures are observed at 20 °C between 1 bar and 3000 bar: two Bragg peaks are visible at $s = 0.0149$ Å^{-1} and 0.02985 Å^{-1}, which can be assigned to the lamellar liquid-crystalline phase or l_d. The Bragg reflection of the second phase at $s = 0.0143$ Å^{-1} and 0.02864 Å^{-1} can be also attributed to a lamellar phase, but more ordered that probably represents a l_o-phase. The lamellar lattice parameter for the first phase is $a = 67 \pm 0.8$ Å, whereas the second more ordered (l_o) is $a = 70 \pm 0.8$ Å. Both lamellar spacing *a* increase continuously with increasing pressure, probably due to a decrease of *trans-gauche* isomers and kinks of the acyl chains and/or a redistribution of the amount of phases, i.e., a continuous increase of the l_o phase at the expense of disordered phase. The lattice constant of the both phases increases by about 4 Å up to 3000 bar, possibly owing to an increase in l_o content.

DOPC/SM/Chol   The pressure-dependent SAXS diffraction patterns at 20 °C from 1 bar up to 3000 bar are shown in Figure 3.25(C). The lattice constant *a* and half-width δ of the first order Bragg reflections for this temperature as a function of pressure are presented in Figures 3.25(D) and 3.25(E). At all pressures the Bragg reflections display ratios of diffraction spacing of 1:2, which are typical of lamellar phases. The lattice constant increases continuously by ~3 Å with increasing pressure. A slight increase of the half-width δ of the lamellar reflection is also observed up to 700 bar.

Unexpectedly, the SAXS diffraction patterns of the DOPC/SM/Chol (33:33:33) mixture do not clearly show the existence of two coexisting phases like in the lipid mixture DOPC/DPPC/Chol (34.5:34.5:31). Literature data show that the interfacial region of saturated phospholipids significantly differs from that of SM, mainly because the amide group present in SM can act as hydrogen-bond acceptor, a feature absent in phospholipids (BROWN, 1998; RAMSTEDT,1999; RAMSTEDT, 2002). The "fluidizing" effect of cholesterol is based on the balance between lipid/cholesterol and lipid/lipid interactions. Mostly, intermolecular interactions of phospholipids are due to van der Waals forces and hydrophobic effects.

However, in the case of sphingolipids, it has been suggested that the hydrogen bonds induced by the amide group at the polar-apolar interface, which can act both as hydrogen bond-donating and -accepting group, are responsible for these intermolecular interactions (OHVO-REKILÄ, 2002). As seen in FCS experiments, in the case of SM, the lipid mobility was always found lower than that of PC with comparable saturated chain length, i.e., DPPC and DSPC (SCHERFELD, 2003). It is probably likely that a rather strong hydrogen bond network is responsible for the larger stiffness of SM membranes with respect to PC bilayers, which may be reflected in a shift of the lattice constant of one phase closer to the other, i.e., the whole system achieves a more ordered state.

POPC/DLPC Figure 3.26(A) depicts the diffraction patterns of POPC/DLPC (50:50) from 1 up to 3000 bar at 300-400 bar intervals at $T = 20$ °C as a function of pressure. SAXS experiments of this lipid composition show a phase transition at ~2300 bar, probably from a fluid to a gel-fluid phase coexistence region. At 1 bar, two Bragg peaks are recorded at $s = 0.0161$ and $s = 0.0322$ Å^{-1}, respectively, which are spaced in the ratio 1:2 indicating a lamellar phase. At 1 bar, the lamellar lattice parameter a has a value of 62 ± 0.7 Å, and increases by increasing pressure. As shown in Figure 3.26(B), at ~2 kbar the Bragg reflections abruptly shift to lower s-values, leading to a superposition of two broad Bragg peaks corresponding to a-spacing of about 76 ± 0.8 Å and 80 ± 0.9 Å, which probably correspond to fluid and gel like domains, respectively.
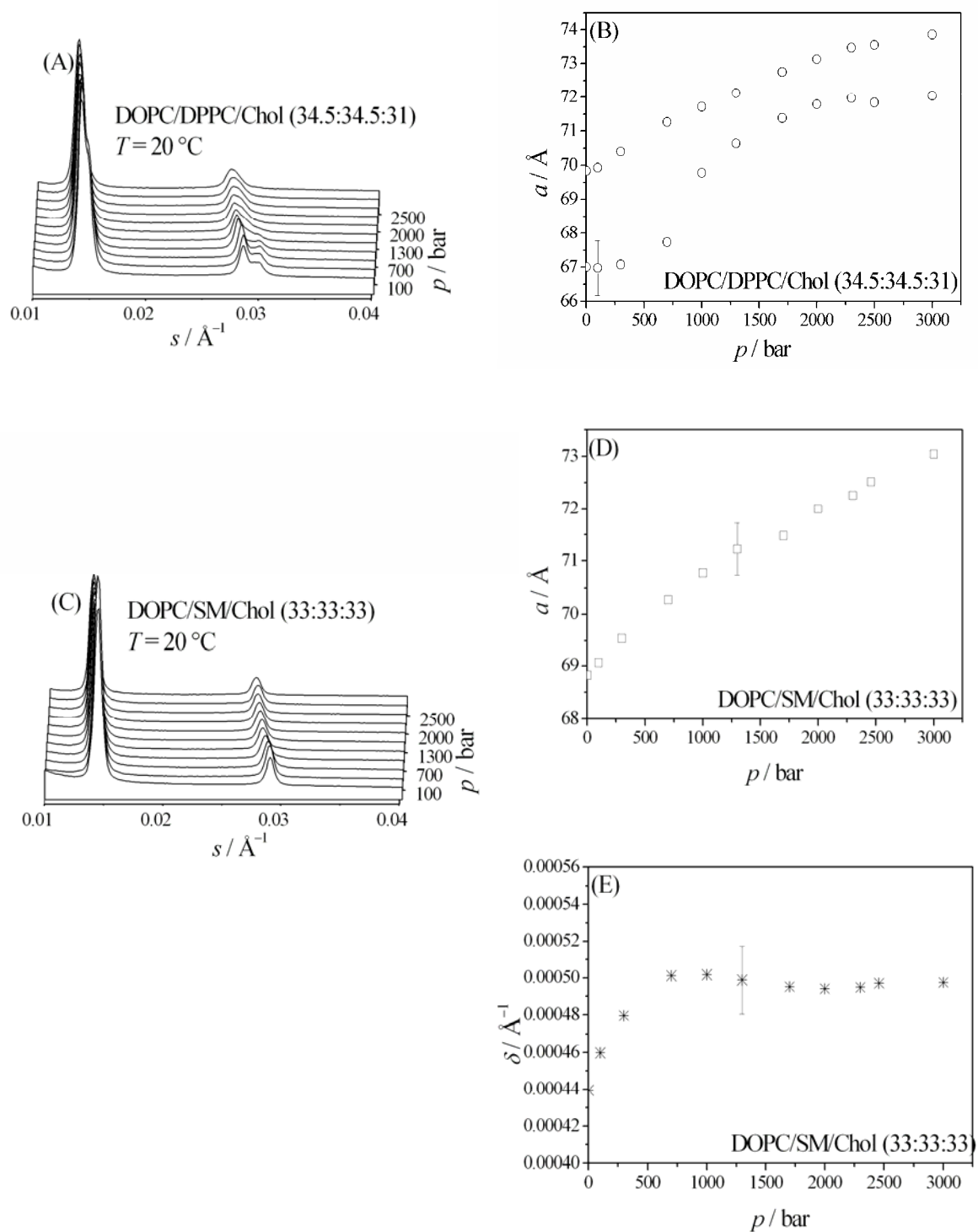
Figure 3.25 (A) and (C) Selected diffraction patterns of DOPC/SM/Chol (33:33:33) and DOPC/DPPC/Chol (34.5:34.5:31), respectively, at $T = 20$ °C as a function of pressure. (B) Lattice constants a of the Bragg reflections of the l_o and l_d phase of DOPC/DPPC/Chol (34.5:34.5:31) at $T = 20$ °C as a function of pressure. (D) Lattice constant a and (E) half-widths δ of the Bragg reflections of DOPC/SM/Chol (33:33:33) at $T = 20$ °C as a function of pressure.
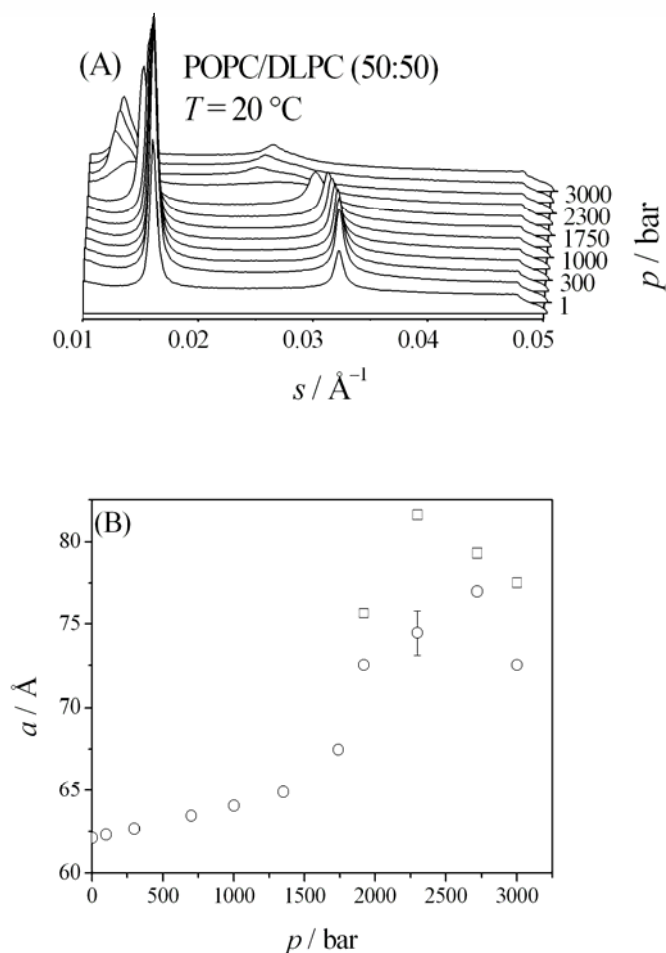
Figure 3.26 (A) Selected diffraction patterns of POPC/DLPC (50:50) in excess water at $T = 20$ °C as a function of pressure. (B) Lattice constants a of the Bragg reflections of POPC/DLPC (50:50) at $T = 20$ °C as a function of pressure.

3.3.4   Conclusions

Pressure dependent experiments on the model biomembranes POPC/DLPC (50:50), DOPC/DPPC/Chol (34.5:34.5:31), and DOPC/SM/Chol (33:33:33) are carried out from 1 bar up to ~3000 bar using two-photon excitation fluorescence microscopy and small angle x-ray scattering. As far as the GUVs in the two-photon excitation fluorescence microscopy experiments are concerned, information about the packing of the lipid upon pressurization and

the topology changes of the single vesicles can be obtained. Generally, the shape of a vesicle is largely determined by the minimum bending energy (JÜLICHER, 1993). As a consequence, the shape is determined by the area and volume ratio of the vesicle, the spontaneous curvature, and the area difference of the two opposing monolayers, which is expected to be sensitively temperature and pressure dependent. In addition, temperature- and pressure-induced changes in phase state and domain coexistence are expected to affect the local bending energy and hence shape of the lipid vesicle (BAUMGART, 2003). Both factors seem to be highly correlated in multiple component lipid vesicles. In our systems, budding or even multiple budding and pinching-off of small vesicles have been observed upon pressurization up to pressures of about 200-300 bar. Such budding generally occurs in order to decrease the line tension between domains on the one hand, and it occurs when the outer monolayer expands more or is less compressible than the inner one, on the other hand.

During the compression cycle, a reduction in the volume of the vesicles is observed accompanied by an increase of the *GP* value, indicating an increasingly tighter packing of the lipids. At a pressure of ~2500 bar, however, the raft lipid mixtures DOPC/SM/Chol (33:33:33), and DOPC/DPPC/Chol (34.1:34.1:31), still show the existence of two coexisting phases (l_o and l_d). Upon decreasing the pressure, the lipid mixture POPC/DLPC (50:50) shows changes in morphology of the GUVs. Spherical-ellipsoidal-polygonal shape transitions occur accompanied by fluctuations of the membrane surfaces and fission of lipid material. Whereas, the raft lipid mixtures containing more than 30 mol% cholesterol maintain mostly a spherical-ellipsoidal shape.

The changes in *GP* value mostly occur in the same pressure range where SAXS data on the lipid bilayer structure and phase state exhibit characteristic changes.

3.4   Partitioning of a dually lipidated N-Ras protein into raft model systems studied by two-photon excitation fluorescence microscopy

3.4.1   Introduction

In this part of the work two-photon fluorescence microscopy on giant unilamellar vesicles is applied to follow the insertion of a fluorescently labelled and completed lipidated N-Ras protein (N-Ras wt 1-181 MIC7 HDFarOMe) (Figure 3.27) into heterogeneous lipid bilayer systems. The bilayers consist of the canonical raft mixture POPC/SM/Chol, which depending on the concentrations of the constituents separate into liquid disordered (l_d), liquid ordered (l_o), and solid ordered phases (s_o).

At first two different lipid compositions were chosen (from the de Almeida three phase diagram), one in the l_o + l_d range and one in the l_o + s_o region. Laurdan was used as fluorophore label, to have a quantitative proof through the *GP* average value of the observed phases while cooling down the temperature.

The second part of the measurements was carried out with GUVs composed by POPC/SM/Chol (50:25:25, mol%), and POPC/SM/Chol (25:65:10) , which were labelled with Lissamine Rhodamine and by adding the N-Ras protein labelled with a Bodipy to the solution at ~30 °C. Through the simultaneous comparison of the images shown in the Rhodamin and Bodipy channels will be directly followed how the protein binds to the lipid microdomains.
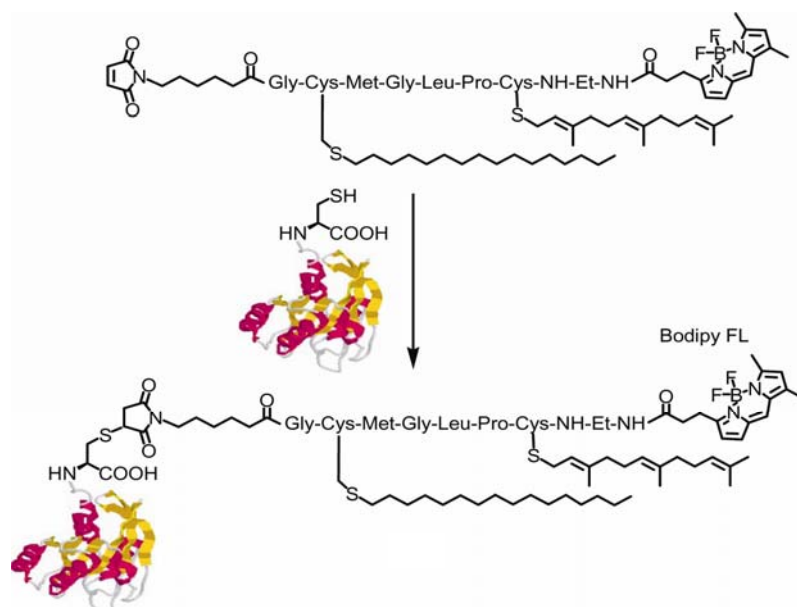
Figure 3.27 Schematical synthesis of the semisynthetic N-Ras wt 1-181 MIC7 HDFarBodipy protein.

3.4.2   POPC/SM/Chol at different lipid ratios

The phase diagram of the lipid mixture POPC/SM/Chol at physiologically relevant temperatures shows a large binary coexistence region of liquid-disordered and liquid-ordered domains, such as for the composition POPC/SM/Chol (50:25:25). By varying the lipid ratio, further phase coexistence regions can be prepared, such as $l_o + s_o$ phase coexistence region from POPC/SM/Chol (25:65:10). The phase transitions of single GUVs formed by the typical raft mixture POPC/SM/Chol (50:25:25) are followed by cooling using the Laurdan GP function. Figure 3.28(A) presents GP average values resulting from the GP histograms. Between 61 and 45 °C the vesicles show homogeneity and low GP values ($\sim\!-0.15$). From ~44 °C till the lowest temperature (23 °C) the Laurdan GP images show two regions with different GP intensities. In this case, one histogram is centred at $\sim\!-0.25 \pm 0.05$ and the other one at $\sim\!0.06 \pm 0.01$. The lowest GP value can be assigned to the l_d phase, whereas the highest to a more ordered phase (probably l_o), which still does not assume values typical of a gel phase ($\sim\!0.6\text{-}0.7$), however (BAGATOLLI, 2000). The measurements with POPC/SM/Chol (25:65:10) are shown in Figure 3.28(B). Again, the GP average values exhibit low intensities at high temperatures till ~45 °C; at lower temperature, the images start to show inhomogeneities. Below 40 °C, Laurdan GP histograms are both found at high GP average values ($\sim\!0.56 \pm 0.11$) indicating the presence of a gel phase (s_o) and at lower GP average values ($\sim\!-0.05 \pm 0.01$) which might correspond to a l_o phase.

For the POPC/SM/Chol lipid mixture it was not so easy to obtain unambiguously GP values because of the inhomogeneities present in the different vesicles at the same temperatures. Figure 3.29 shows an example of the mixture POPC/SM/Chol (50:25:25) at $T =$ 25 °C. It is clearly recognizable from the GUVs, that laterally separated domains are observed in some but not in all the vesicles under the same conditions (VEATCH, 2003a).
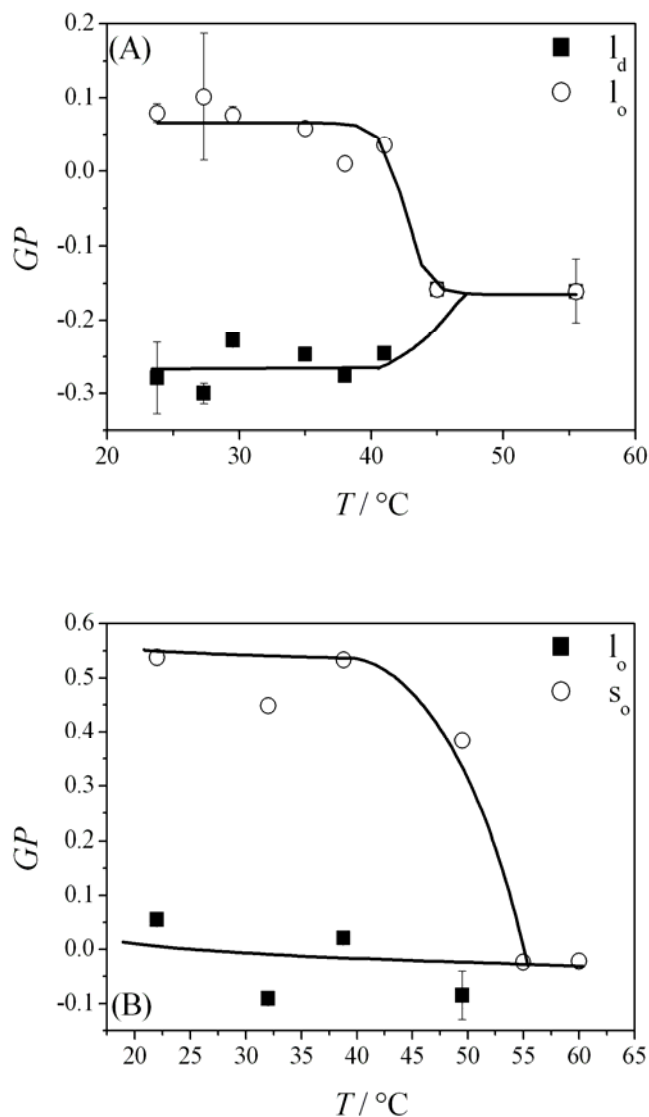
Figure 3.28 (A) *GP* images of the equatorial section of a GUV composed of POPC/SM/Chol (50:25:25) as a function of temperature. Below 45 °C the *GP* histograms are centred at $\sim-0.15 \pm 0.05$, corresponding to a l_d phase and $\sim 0.06 \pm 0.01$, corresponding to a l_o region. (B) *GP* images of a vesicle composed of POPC/SM/Chol (25:65:10) as a function of temperature. Below 40 °C, Laurdan *GP* histograms are found at high *GP* average values ($\sim 0.56 \pm 0.11$) indicating the presence of a gel phase (s_o) and at lower *GP* average values ($\sim-0.05 \pm 0.01$), of a l_o phase.
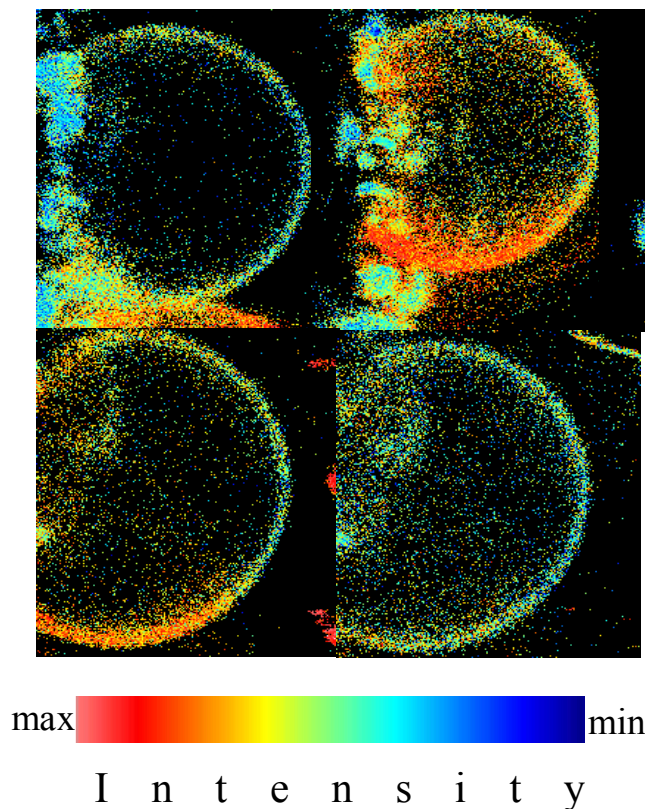
Figure 3.29 Two-photon excitation fluorescence intensity images at the cross-section of Laurdan-labelled GUVs (size ~30μm) composed of POPC/SM/Chol (50:25:25) at 25 °C. Note that laterally separated domains are observed in some but not all vesicles.

3.4.3   Experiments with N-Ras wt 1-181 MIC7 HDFarBodipy

The experiments in two-channels with the farnesylated and hexadecylated N-Ras protein were conducted labelling the lipid membrane with N-Rh-DPPE. At first, it was necessary to verify in which domains this dye partitions. Therefore, an experiment with a known fluorescence probe, Prodan, has been carried out to compare the behaviour of both fluorophores for the same vesicle and under the same conditions. Prodan partitions into the fluid phase 35 times more than that into a gel phase (KRASNOWSKA, 1998). GUVs composed of POPC/SM/Chol (25:65:10), showing a $l_o + s_o$ phase, were prepared with N-Rh-DPPE. Figure 3.30(A) presents a GUV image at $T = 30$ °C showing a dark domain in the middle. Prodan was added and the resulting image is depicted in Figure 3.30(B). N-Rh-DPPE inserts into the same domains as Prodan does, indicating that N-Rh-DPPE is also suitable for detecting l_o domains if no liquid-disordered phase is presented.
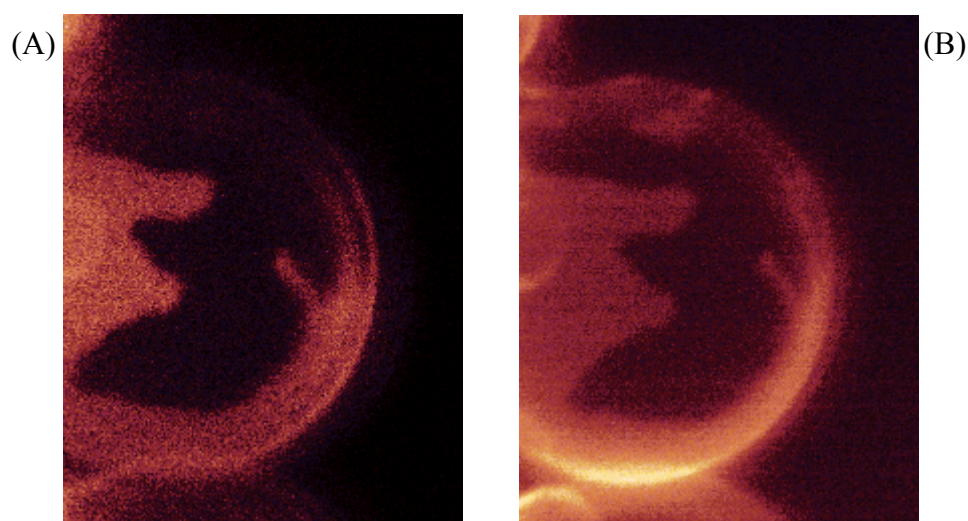
Figure 3.30 Two-photon excitation intensity image (false colour representation) of a GUV (size ~30 μm) consisting of POPC/SM/Chol (25:65:10). (A) shows fluorescence due to *N*-Rh-DPPE and (B) depicts fluorescence of the vesicle after the addition of Prodan.

For the experiments with the N-Ras protein, three systems are chosen: POPC/SM/Chol (50:25:25), due to its broad $l_o + l_d$ phase region, POPC/SM/Chol (25:65:10) showing a $l_o + s_o$ phase and POPC/SM/Chol (43:43:14), a lipid ratio which presents a three phase region $l_o + l_d + s_o$ at ~23 °C, as shown in the three phase diagram taken from de Almeida (Figure 3.31). Vesicles are then prepared mixing the lipids with *N*-Rh-DPPE and adding a 7 mol% (with respect to lipid) solution of the hexadecylated and farnesylated N-Ras in 1 mM phosphate buffer (pH 7) to the solution containing GUVs at ~30 °C. The Ras lipoprotein was prepared with a hexadecylthioether instead of the labile native palmitoyl thioester to prevent hydrolysis of the acyl function during the experiments. The Bodipy-label attached to the protein reports on the location of the protein within the lipid assembly (green channel), whereas *N*-Rh-DPPE, detected in the red channel, is normally used as marker of fluid domains. The GUV images, taken after the protein binding process to the various lipid vesicle systems was completed, are shown in Figure 3.32. Figures 3.32(A) and 3.32(B) depict GUVs composed of POPC/SM/Chol (50:25:25) exhibiting the round-shaped domains typical of coexisting liquid-like phases. Circular domains will result if fluid domains are embedded in a fluid environment. In this case isotropic phases are presented and the line energy (tension), which is associated with the rim of two demixing phases, will be minimized by optimizing the area

to perimeter ratio (DIETRICH, 2001). The bright areas with embedded N-Rh-DPPE correspond to liquid-disordered (l_d) domains, the dark domains mainly consist of l_o lipid. The domain shapes seen in Figures 3.32(C) and 3.32(D), have different patterns, pointing to the presence of some solid-ordered gel phase. It is possible to follow directly how the protein binds to the lipid microdomains through the simultaneous comparison of the images shown in the Rhodamin- and Bodipy-channel. From the GUVs images of both channels, it is clearly seen that the spatial distribution of the inserted N-Ras coincides with that of the N-Rh-DPPE in all cases. Both are preferentially localized in the l_d domains of the mixed $l_d + l_o$ system (Figures 3.32(A) and (B)). The same holds true for the $l_d + l_o + s_o$ phase coexistence region (Figure 3.32(D)). In the mixed-domain $l_o + s_o$ region, however, preferential partitioning occurs in the l_o phase (Figure 3.32(C)).
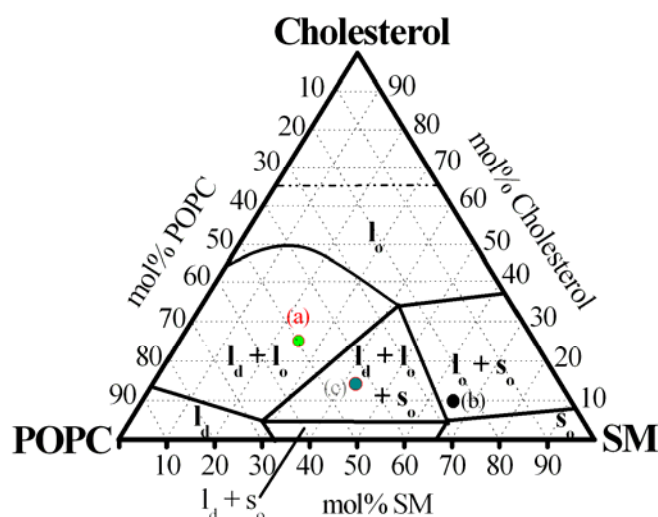
Figure 3.31 POPC/PSM/Chol phase diagram at $T = 23\ °C$ (adopted from de ALMEIDA, 2003). The circles (a), (b), and (c) denote lipid compositions where experimental data have been taken: (a) POPC/SM/Chol (50:25:25), $l_o + l_d$ phase coexistence region; (b) POPC/SM/Chol (25:65:10), $l_o + s_o$ region; (c) POPC/SM/Chol (43:43:14) $l_d + l_o + s_o$ phase region.

During the cooling cycle, the dark domains corresponding to the more ordered phase grow as it is clearly visible in Figure 3.33. Till 25 °C the red channel and the green channel still show the same lipid patterns, but at lower temperatures, when the nonfluorescent areas occupy most of the surface of the vesicle, as shown in the red channel of Figure 3.33, the Bodipy-channel reveals a new scenario: the protein binds in the GUVs homogeneously .

Figure 3.32 Two-photon excitation fluorescence intensity images (false colour representation) of GUVs (size ~ 30 µm) consisting of (A) and (B) POPC/SM/Chol (50:25:25) + 7 mol% N-Ras at $T = 25$ °C ($l_d + l_o$ phase); (C) POPC/SM/Chol (25:65:10) + 7 mol% N-Ras at $T = 30$ °C ($l_o + s_o$ phase); and (D) POPC/SM/Chol (43:43:14) + 7 mol% N-Ras at $T = 29$ °C ($l_d + l_o + s_o$ phase). Fluorescence intensity was collected in two channels: the green channel detects the Bodipy fluorescence intensity and the red channel the N-Rh-DPPE fluorescence intensity, respectively. Images were taken at the top part of the GUVs.

The two-photon fluorescence microscopy can also be applied to yield kinetic data on the insertion process of the protein into GUVs. An example is given in Figure 3.34. It presents

fluorescence microscopy images of the GUVs in the two channels taken after the injection of N-Ras solution into the dispersion of lipid vesicles being in the $l_o + s_o$ mixed-domain region (POPC/SM/Chol (25:65:10)). Before the insertion at time $t = 0$, the green channel detects only few counts leading to a low fluorescent background. After about 7 min, it is possible to detect the spherical form of the vesicle in the Bodipy channel as well. The last image was taken after ~30 min, when the binding process of N-Ras to the lipid vesicle was fully completed. The images in both channels coincide; firstly this indicates, that the protein binds preferentially to the fluid-like domains. However, part of the N-Ras binds - to a much lesser extent - to the s_o domains as well. Secondly, the domain shapes do not alter significantly upon incorporation of the dually lipidated protein.

The rate of the insertion process significantly depends on the type of present domains. The graph, also shown in Figure 3.34, reveals normalized Bodipy fluorescence intensity data taken at 30 °C for lipid systems in the $l_o + l_d$ (POPC/SM/Chol 50:25:25) and in the $l_o + s_o$ (POPC/SM/Chol 25:65:10) phase coexistence region, respectively. The data clearly demonstrate that the binding process is much faster if the farnesylated and hexadecylated N-Ras partitions into liquid-disordered domains. Embedding N-Ras in the $l_o + s_o$ mixed-domain system is six times slower than in $l_d + l_o$ mixed-domain vesicles.

Furthermore, we examined and compared the partitioning of N-Ras into the various domains as a function of time (Figure 3.35). From the equilibrium data, the relative partition coefficient of the dually lipidated protein in the various phases can be determined by measuring the green channel fluorescence intensity values (I) of the different domains and normalize them to the mean intensity value of each phase ($\bar{I}$). As background, the fluorescence intensity of the channel was considered before the protein was added. Hence, $I / \bar{I}$ can be considered a measure of the partition coefficient of the protein between different domains. In the $l_d + l_o$ mixed-domain system, partitioning of N-Ras into l_d domains is 1.3 times larger than into l_o domains, whereas for the mixture POPC/SM/Chol (25:65:10), representing a $l_o + s_o$ mixed-domain system, binding to l_o domains is favoured by a factor of ~2 over solid-like (s_o) domains.

Hence, the phase sequence of preferential binding of N-Ras to mixed-domain lipid vesicles is $l_d > l_o \gg s_o$. The binding kinetic follows a similar order: binding to l_o domains is about 60% slower than to l_d regions, and binding of N-Ras into s_o domains is ~40% slower than into l_o domains.
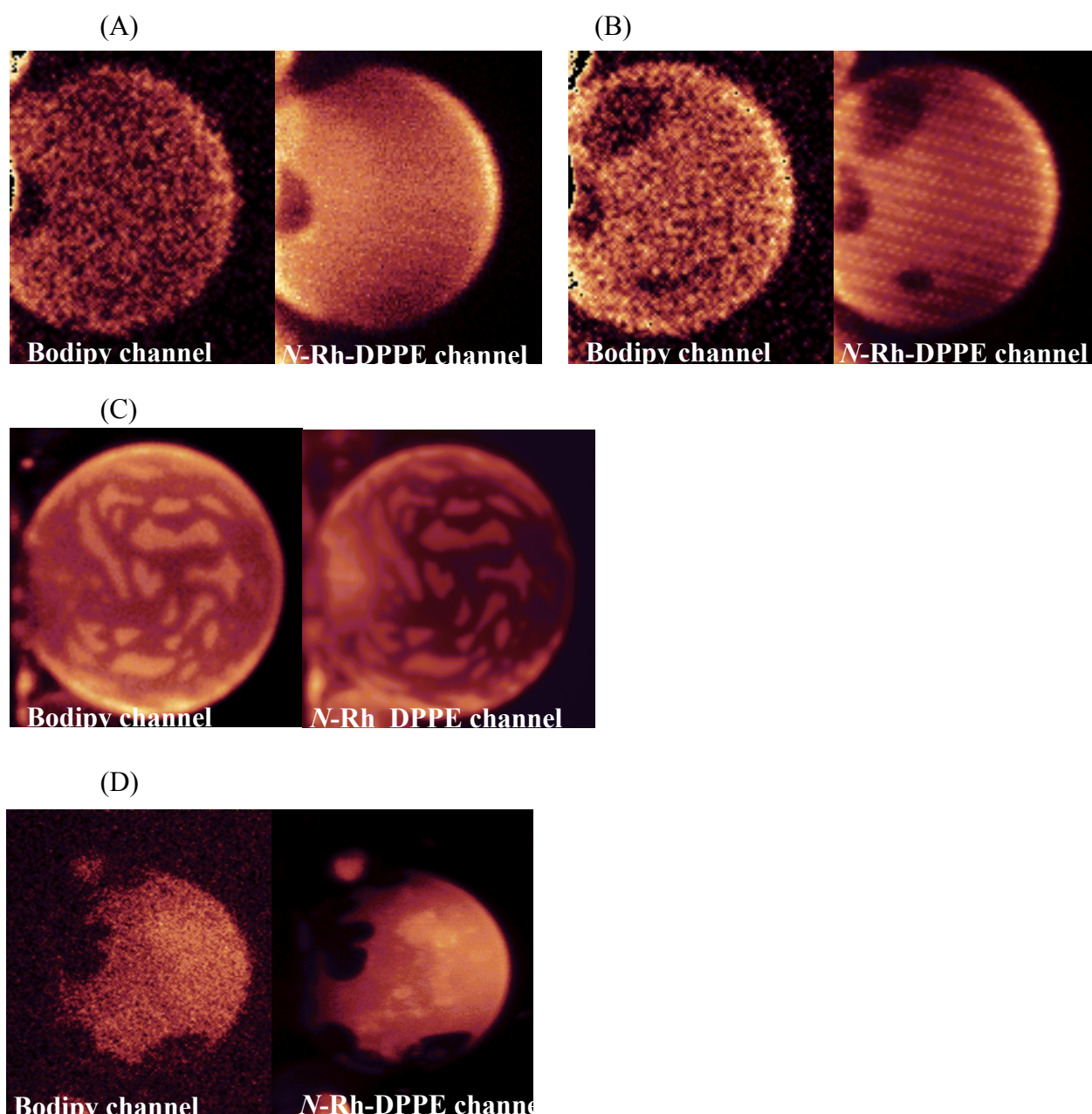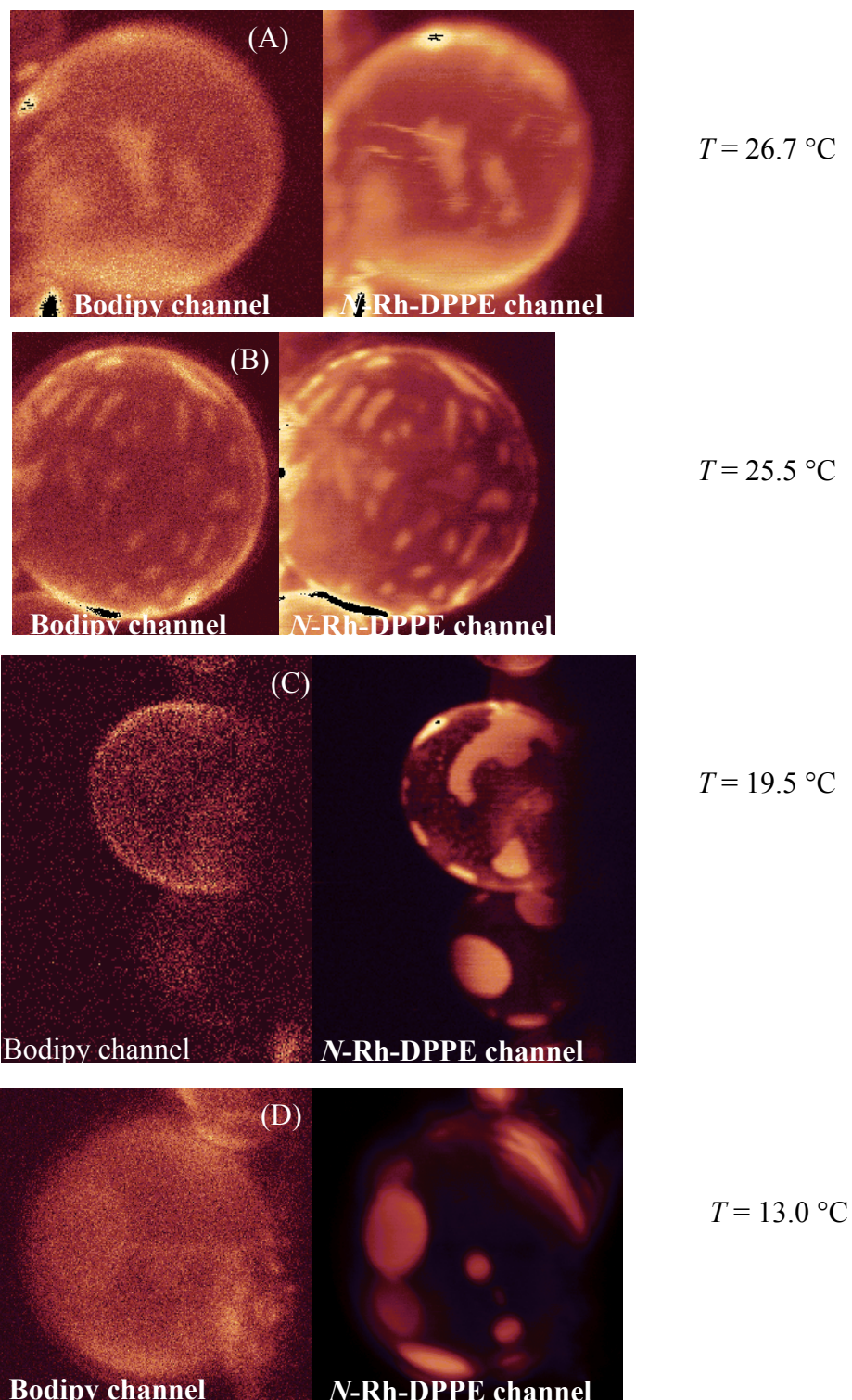
Figure 3.33 Two-photon excitation fluorescence intensity images (false colour representation) of GUVs (size ~ 30 μm) consisting of POPC/SM/Chol (25:65:10) + 7 mol% N-Ras at different temperatures. Fluorescence intensity was collected in two channels: the green channel detects the Bodipy fluorescence intensity and the red channel the *N*-Rh-DPPE fluorescence intensity, respectively. Images were taken at the top part of the GUVs.
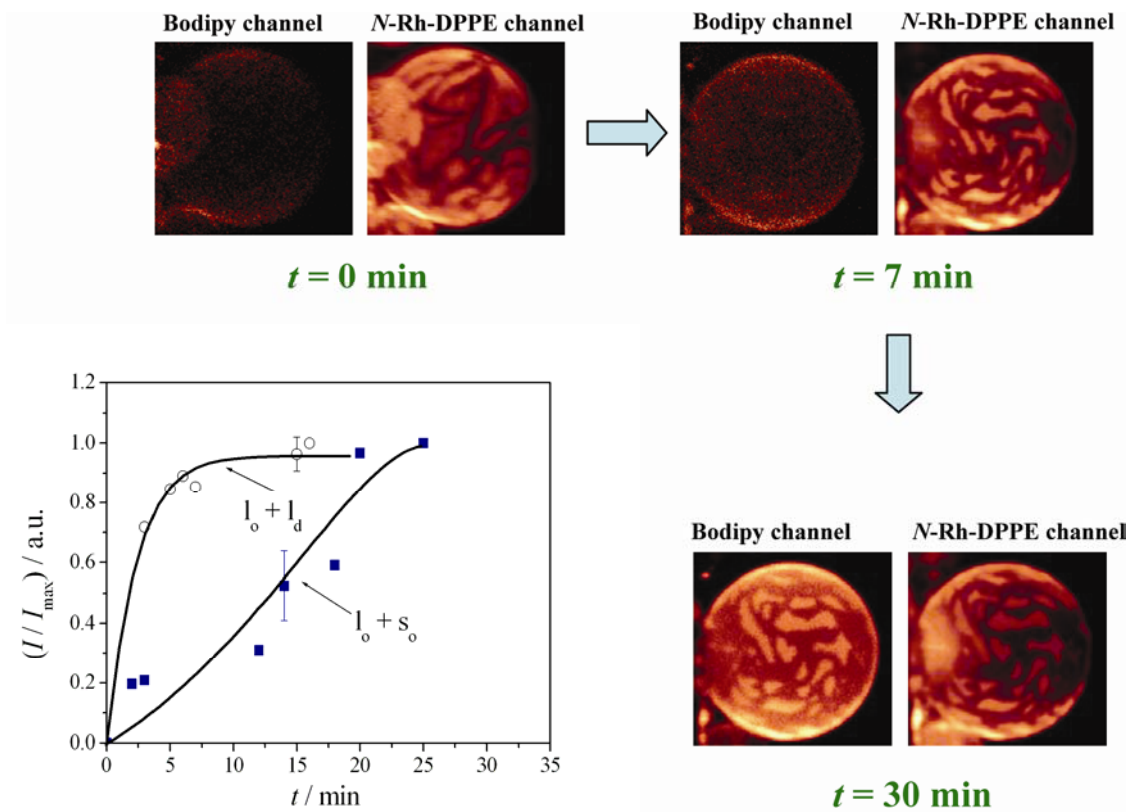
Figure 3.34 Time-dependent fluorescence intensity images of the system POPC/SM/Chol (25:65:10, l_o + s_o region) + *N*-Rh-DPPE with added Bodipy labelled N-Ras protein, collected in two channels (*T* = 30 °C). The Bodipy channel monitors the insertion of N-Ras in the GUV (~ 30 μm). The first image was taken before the injection of the protein, the other two images were taken at 7 and 30 min after the injection of N-Ras to the solution, respectively. The curves shown in the graph represent the kinetic insertion data – in terms of relative changes in Bodipy fluorescence intensity – of N-Ras in different domain coexisting regions: l_o + l_d (POPC/SM/Chol (50:25:25)) and l_o + s_o (POPC/SM/Chol (25:65:10)), respectively.
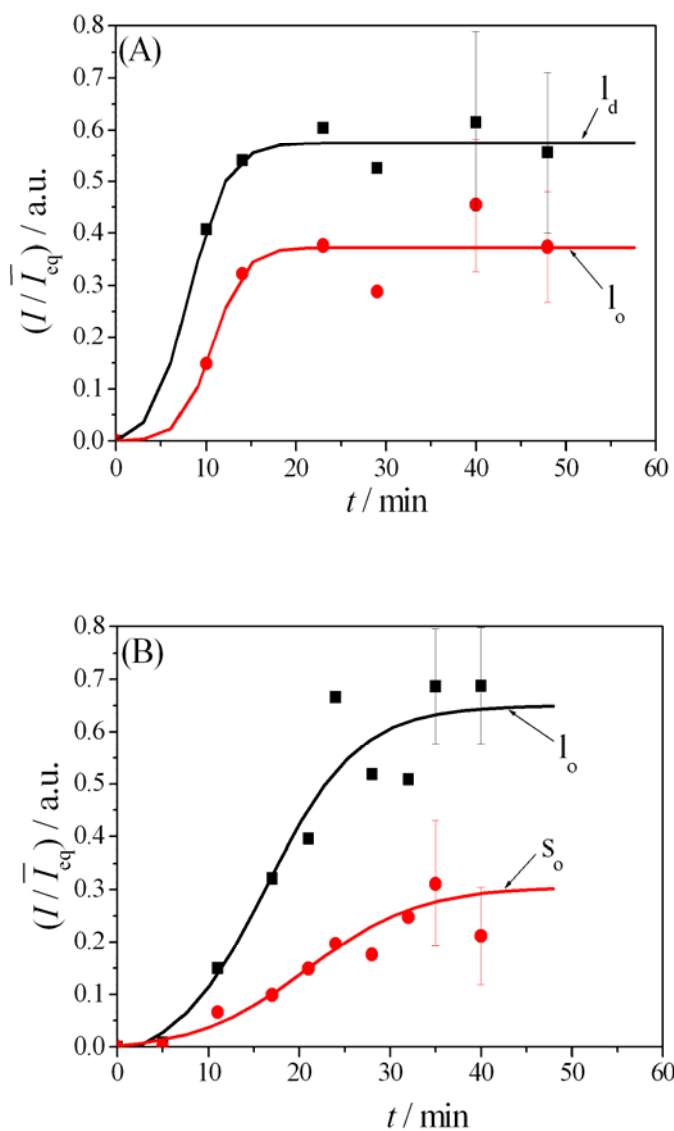
Figure 3.35 Time-dependent partitioning of hexadecylated and farnesylated N-Ras in the different domains of GUVs composed of (A) POPC/SM/Chol (50:25:25) (l_o + l_d phase coexistence region), and (B) POPC/SM/Chol (25:65:10) (l_o + s_o phase coexistence region). The fluorescence intensity of the channel is taken as background before the addition of the protein, and the Bodipy fluorescence intensity values of the different domains were normalized to the mean intensity values of each phase.

3.4.4 Conclusions

By preparing different lipid mixtures of the system palmitoylphosphatidylcholine, sphingomyelin and cholesterol, various coexisting lipid phases ($l_o + l_d$, $l_o + s_o$, and $l_d + l_o + s_o$) could be obtained and studied by two-photon excited fluorescence microscopy. Interestingly, independently of the time of incubation, no significant modifications of the surface and shape of the domains were observed during N-Ras insertion. The results provide direct evidence that partitioning of hexadecylated and farnesylated N-Ras occurs preferentially in fluid-like liquid-disordered lipid domains, which is also reflected by a kinetic of incorporation into the fluid lipid bilayer membrane, which is 60% faster than in l_o regions. To a much lesser extent (~50%), the lipidated protein is also embedded in liquid-ordered, raft-like domains. In an $l_o + s_o$ mixed-domain lipid system, binding to l_o domains takes place as well, and it is favoured by a factor of ~2 over solid-like (s_o) domains. The binding kinetics of N-Ras into s_o domains is ~40% slower than into l_o domains. Hence, the phase sequence of preferential binding of N-Ras to mixed-domain lipid vesicles is $l_d > l_o \gg s_o$.

3.5   Insertion of dually lipidated N-Ras proteins into ternary model raft lipid mixtures studied by IRRAS

3.5.1   Introduction

In this chapter Langmuir monolayers of POPC/SM/Chol (50:25:25), which represents a typical raft mixture, have been used as half of a model membrane to study the insertion of N-Ras proteins with different lipidated anchors (Figure 3.36) by infrared reflection absorption spectroscopy. The proteins adsorb at the air/D_2O interface and insert with their anchors into uncompressed lipid monolayers. The amid I band appears at wavenumbers typical of α-helical and β-sheet secondary structures. At the physiological surface pressure of 30 mN m^{-1}, the two proteins show differences in their behaviour: the farnesylated and hexadecylated protein desorbs completely from the monolayer, whereas the dually hexadecylated N-Ras remains adsorbed.

The aim of this study is to examine the insertion of the proteins into the lipid monolayer to understand the possible role of the farnesyl anchor in N-Ras proteins.

Figure 3.36 (A) Chemical structure of N-Ras wt 1-181 MIC7 HDFarBodipy and (B) chemical structure of N-Ras wt 1-181 MIC7 HDHDOMe.

Figure 3.37 (A) Π / A isotherm of the lipid mixture POPC/SM/Chol (50:25:25). (B) Example of an IRRA curve taken at Π = 30 mN m^{-1} and T = 20 °C in D$_2$O. The spectra are recorded at an angle of incidence of 40° with p-polarized light.

Figure 3.37(A) presents the Langmuir isotherm of the lipid mixture POPC/SM/Chol (50:25:25) in D$_2$O taken at T = 20 °C. At Π = 1 mN m^{-1} the curve profile shows an equilibrium between a liquid expanded state (LE) and a gas phase (G). Upon diminishing the lipid area to ~ 0.9 nm^2 molecule^{-1} the curve starts to increase, indicating a LE phase region. When the surface pressure reaches the value of ~7 mN m^{-1}, the lipid monolayer becomes more ordered, the system, however, remains in a LE phase.

IRRAS measurements at different incident angles (between 32 and 68 °C) are performed at T = 20 °C and at Π = 30 mN m^{-1}, which is comparable to the condition having in a bilayer (BLUME, 1979). Figure 3.37(B) depicts an example of the measurement of the lipid mixture POPC/SM/Chol (50:25:25) taken at the angle of 40° with p-polarized light. The positions of the CH$_2$ peaks at 2924 cm^{-1} (CH$_2$ antisymmetric stretching mode) and at 2854 cm^{-1} (CH$_2$ symmetric stretching mode) point out that under these conditions the overall lipid mixture is still in a fluid-like phase. The band at ~1660 cm^{-1} is characteristic of sphingolipids and the band at 1735 cm^{-1} is due to the C=O groups of the POPC.

3.5.2   Adsorption of N-Ras HDFar protein at the air/water interface

The adsorption of N-Ras HDFarOMe at the air/water interface as a function of protein concentration in 100 mM NaCl and D_2O was studied first. Due to the limited amount of protein material available, all these measurements were performed in a small trough with an area of 7.07 cm^2 and a volume of 11.15 mL. For the lowest concentrations (c = 50 and 100 nM) used the surface pressure starts to increase subsequent to the injection into the subphase, only after a lag time, however, for the higher protein concentrations (200 and 400 nM) immediately. Other proteins like, for instance, the GM2-activator protein at higher concentrations or KLAL was already reported to have a similar behaviour (GIEHL, 1999). A possible explanation of this delay in the adsorption may be the fact that the N-Ras protein bears hydrophobic side chains which can also adsorb to the Teflon surface of the trough. The diffusion of the protein in the subphase depends on the rate of stirring, which was kept constant for all measurements. Figure 3.38 shows the maximal surface pressure as a function of protein concentration in the subphase. For the dually lipidated protein with HD and Far anchors, the maximum value of Π_{max} (saturation value) approaches 24 mN m^{-1} at a protein concentration of 200 nM. The surface activity of proteins, i.e. the pressure value reached at saturation, generally reflects their ability to adsorb at an interface.
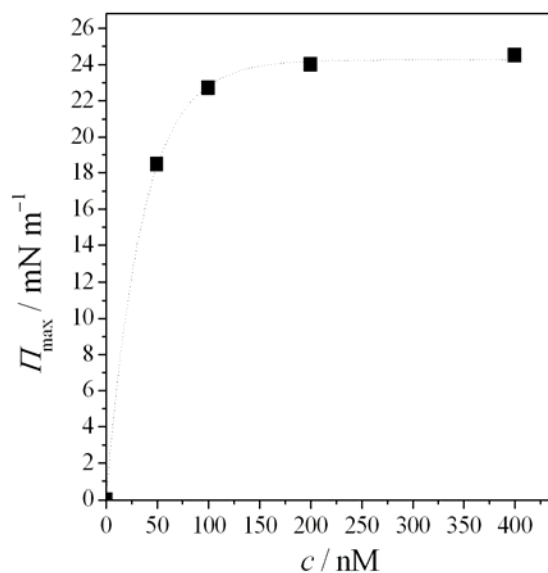
Figure 3.38 Maximal surface pressure Π_{max} as a function of the protein concentration for the dually lipidated N-Ras wt 1-181 MIC7 HDFarBodipy protein (c = 50, 100, 200, 400 nM, T = 20 °C, in 100 mM NaCl, D_2O).

Figure 3.39 (A) Π / t isotherm of an N-Ras MIC7 HDFarBodipy film (c = 200 nM in 100 mM NaCl in D$_2$O, T = 20 °C). (B) IRRA spectra (angle 40°, s-polarized light) of the N-Ras MIC7 HDFarBodipy film at the respective positions 1-4 of the surface pressure time curve shown in Figure 3.39(A).

Figure 3.40 IRRA angle dependence measurements of N-Ras MIC7 HDFarBodipy (c = 200 nM in 100 mM NaCl in D$_2$O, T = 20 °C), performed at Π = 20 mN m^{-1}. The spectra are recorded at different angle of incidence (A) with p- and (B) with s-polarized light.

The surface pressure as a function of time of N-Ras MIC7 HDFar Bodipy is shown in Figure 3.39(A). At a protein concentration of 200 nM, the surface pressure increases immediately after the injection into the subphase, and in the first 3 hours it reaches a surface pressure of 14 mN m^{-1}. After that the curve profile increases further, but slower and after 22 hours it reaches a plateau corresponding to the maximal Π value of 19.5 mN m^{-1}. Figure 3.39(B) depicts the amid I band of the IRRA spectra taken at an angle of 40° and with *s*-polarized light, at the marked positions 1-4 of the respective pressure as a function of time in Figure 3.39(A). Upon increasing pressure, the intensity of this band increases until the maximum of the surface pressure is reached (position 4). The angle dependence measurements performed at Π = 20 mN m^{-1}, displayed in Figure 3.40(A) (*p*-polarized radiation) and 3.40(B) (*s*-polarized radiation), clearly show a band at ~1622 cm^{-1}, which is characteristic of an intramolecular β-sheet secondary structure, and a shoulder at ~1645 cm^{-1}, indicating an α-helical structure.
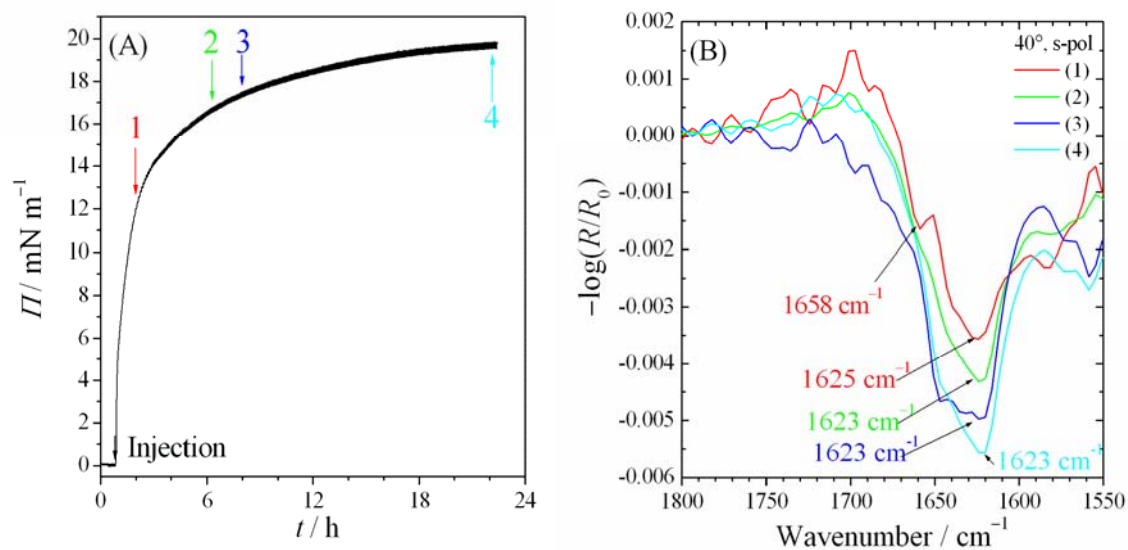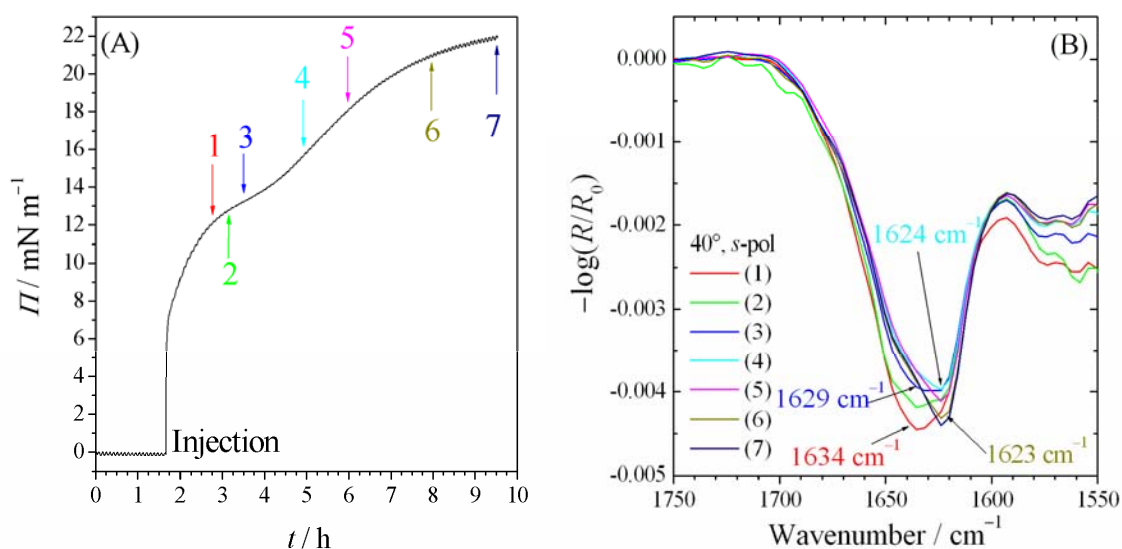

Figure 3.41 (A) Π / *t* isotherm of N-Ras MIC7 HDHDOMe film (*c* = 200 nM in 100 mM NaCl in D$_2$O, *T* = 20 °C). (B) IRRA spectra (angle 40°, *s*-polarized light) of the N-Ras MIC7 HDHDOMe film at the respective positions 1-4 of the surface pressure time curve in Figure 3.41(A).
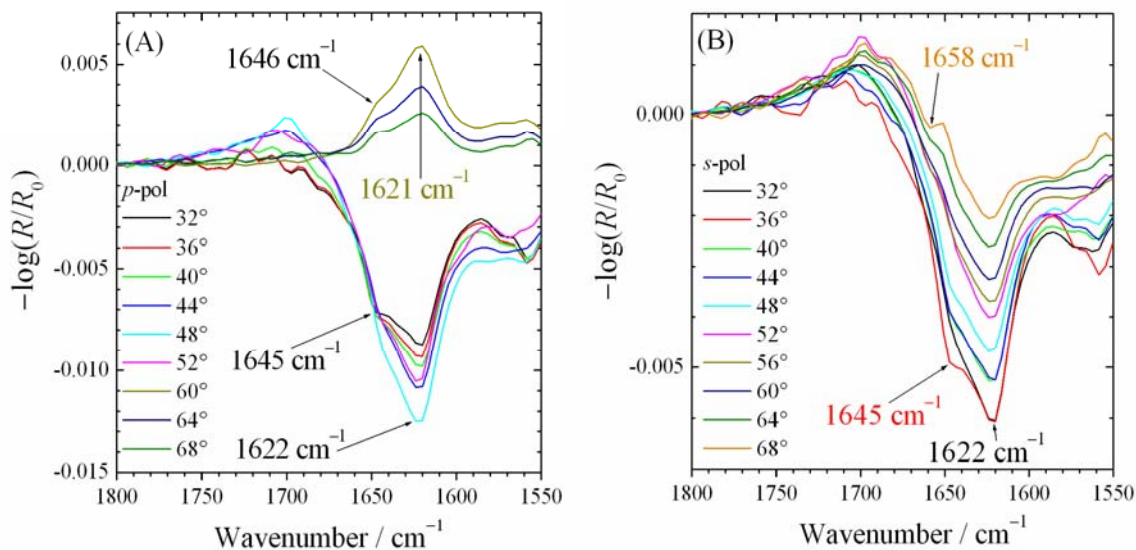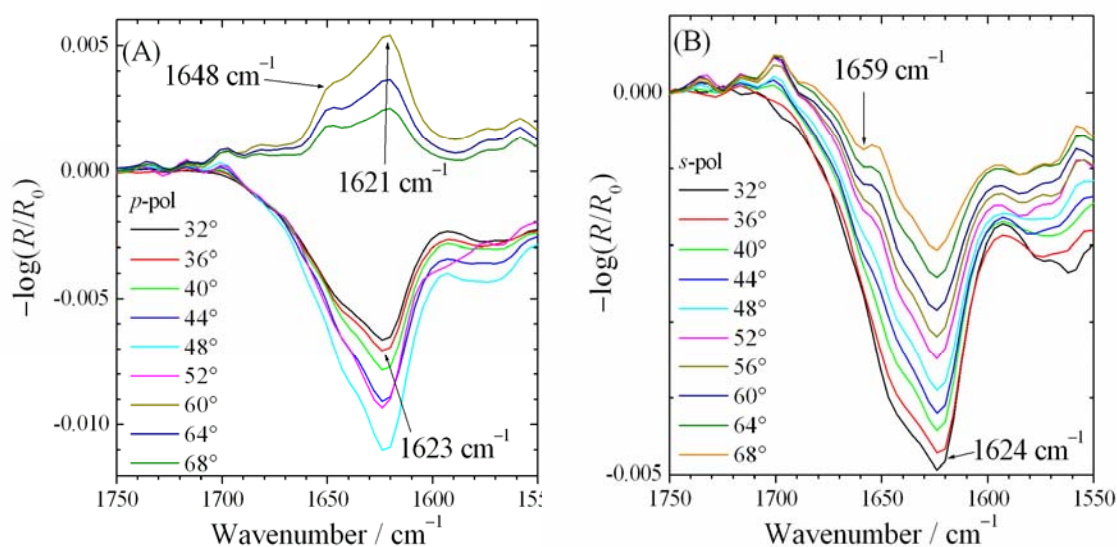
Figure 3.42 IRRA angle dependence measurements of N-Ras MIC7 HDHDOMe (c = 200 nM in 100 mM NaCl in D$_2$O, T = 20 °C), performed at Π = 20 mN m^{-1}. The spectra have been recorded at different angles of incidence (A) with p- and (B) with s-polarized light.

The same kind of experiments were conducted with N-Ras wt 1-181 MIC7 HDHDOMe and the results are depicted in Figure 3.41. Similar to N-Ras MIC7 HDFar Bodipy, the surface pressure increases right after the injection into the subphase of the double hexadecylated protein (c = 200 nM) (Figure 3.41(A)). The adsorption kinetics of the N-Ras HDHD protein at the interface, however, is faster than of the N-Ras containing the farnesylated/hexadecylated anchor. Only after ~10 h the surface pressure reaches its maximum at Π = 22 mN m^{-1}. The surface pressure profile curve as a function of time shows a kink at Π = 13 mN m^{-1}. Until this point, the corresponding amid I band from the IRRA spectra shown in Figure 3.41 (B) (positions 1-3) is predominantly characterised by an α-helical structure; after that, the bands (positions 4-7) shift to smaller wavenumbers, indicating the appearance of a β-sheet structure (1623 cm^{-1}).

The angle dependent measurements performed at Π = 22 mN m^{-1}, displayed in Figures 3.42(A) and 3.42(B) for p-polarized and s-polarized light, respectively depict the same secondary structure for the N-Ras HDHDOMe as for N-Ras HDFarBodipy, i.e. a band at

~1622 cm^{-1}, characteristic of a intramolecular β-sheet secondary structure, and a shoulder at ~1645 cm^{-1}, indicating an α-helical structure.

The measurements, using *s*- and *p*-polarized light at different angles of incidence at constant surface pressure values, allow to determine the orientations of secondary structure elements considering the changes in shape, intensity, and position of the amide I bands. The amid I band contour for *s*- and *p*-polarized light at different angle of incident light ranging from 32 to 68°, was simulated (simulations were performed by Dr. Annette Meister). For the α-helical and β-sheet structures were taken into account the different relative orientations of the secondary structure elements as obtained from the protein crystal structure of the Ras protein as shown in Figure 3.42a (WITTINGHOFER, 1991). A comparison of the measured (Figures 3.40 and 3.42) and simulated spectra (data not shown) reveals that orientations C and D can be excluded for both N-Ras proteins. Orientations C and D are obtained by a ± 45° rotation of the protein around the x-axis. It appears as if N-Ras wt 1-181 Bodipy MIC7 HDFarOMe adsorbs at the air/D$_2$O interface directly in orientation A, whereas N-Ras wt 1-181 MIC7 HDHD first randomly adsorbs at the interface at lower surface pressure (orientation B) and then with increasing surface pressure it changes its orientation to orientation A. At the saturation pressure, both N-Ras proteins adsorb at the air/D$_2$O interface in the same way corresponding to the orientation A.
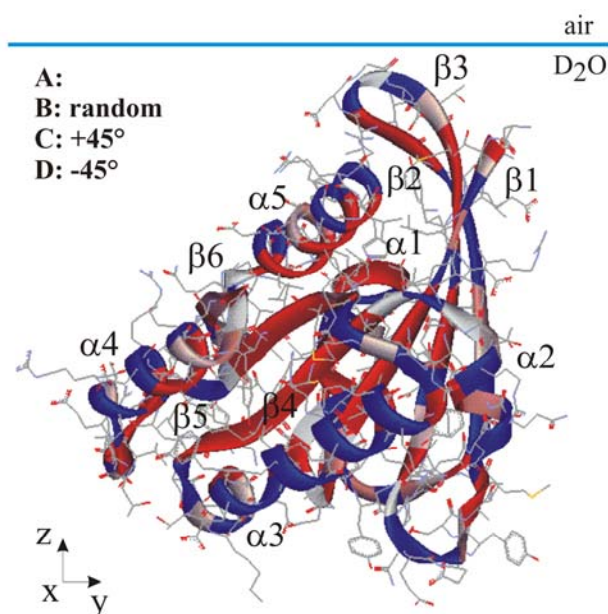
Figure 3.42a Assumed orientation (A) of one Ras protein of the unit cell (PDB entry 121p taken from WITTINGHOFER, 1991) relative to the normal of the air/D$_2$O interface. (B-D) indicate further considered orientations corresponding to a random orientation (B) and two orientations (C, D) obtained by a ± 45° rotation of the protein around the x-axis. The hydrophobic and hydrophilic parts of the protein are indicated in red and blue, respectively.
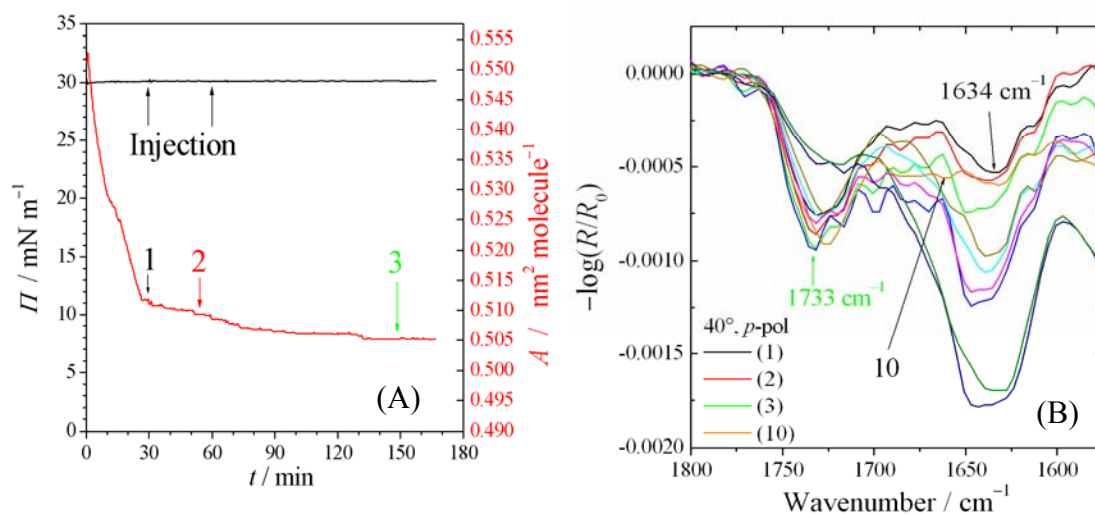
Figure 3.43 (A) Surface pressure versus time of N-Ras MIC7 HDFarBodipy (c = 200 nM in 100 mM NaCl in D$_2$O, T = 20 °C) injected into the subphase of a lipid monolayer consisting of POPC/SM/Chol (50:25:25) at a fixed surface pressure value of Π = 30 mN m^{-1}. (B) IRRA spectra (angle 40°, s-polarized light) of the N-Ras MIC7 HDFarBodipy protein injected into the subphase of the lipid monolayer film at the respective positions 1-3 of the surface pressure time curve in Figure 3.43(A). The position 10 corresponds to the curve taken at a compression of Π = 30 mN m^{-1} after the lipid film was decompressed first to Π = 20 and then to 10 mN m^{-1}, respectively.
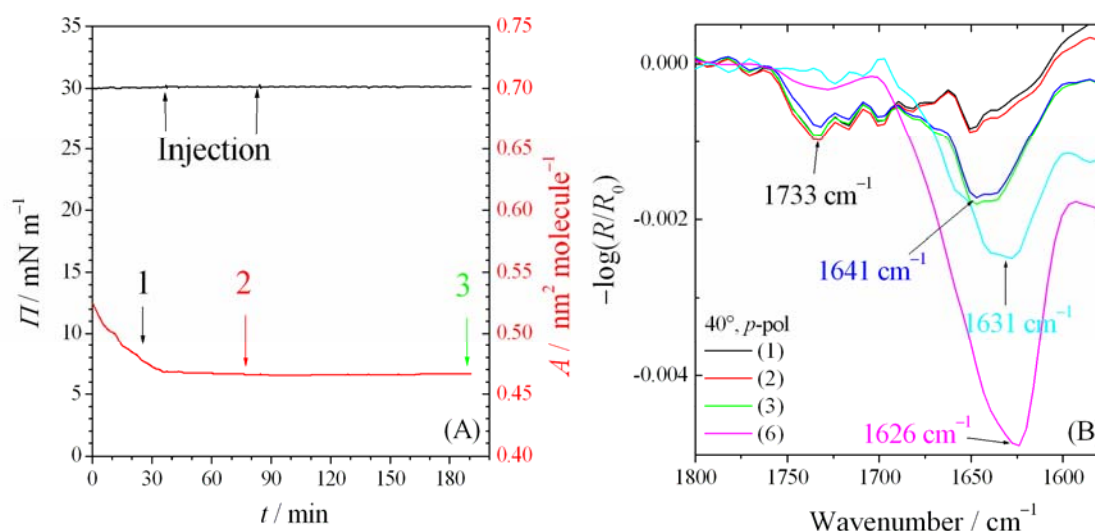
Figure 3.44 (A) Surface pressure versus time of N-Ras MIC7 HDHDOMe (c = 200 nM in 100 mM NaCl in D$_2$O, T = 20 °C) injected into the subphase of a lipid monolayer consisting of POPC/SM/Chol (50:25:25) at a fixed surface pressure value of Π = 30 mN m^{-1}. (B) IRRA spectra (angle 40°, s-polarized light) of the N-Ras MIC7 HDHDOMe protein injected into the subphase of the lipid monolayer film at the respective positions 1-3 of the surface pressure time curve in Figure 3.44(A). The position 6 corresponds to the curve taken at a compression of Π = 30 mN m^{-1} after the lipid film was decompressed first to Π = 20 and then to 10 mN m^{-1}, respectively.
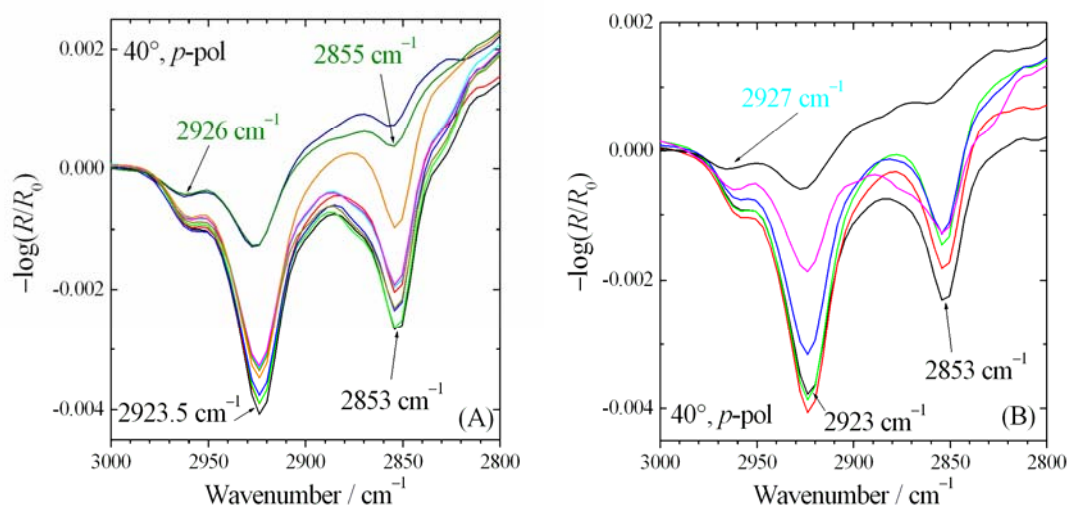
Figure 3.45 (A) Examples of IRRA spectra of the lipid monolayer composed of POPC/SM/Chol (50:25:25), before and after the injection of the dually lipidated proteins, (A) N-Ras MIC7 HDFarBodipy and (B) N-Ras MIC7 HDHDOMe, taken during the compression and decompression cycles of the monolayer film. The position of the CH_2 antisymmetric stretching mode at 2923.5 cm^{-1} and the CH_2 symmetric stretching mode at 2853 cm^{-1} remain constant during the different processes.

3.5.3   N-Ras protein interactions with the lipid monolayer

Measurements at constant surface pressure The lipid monolayers consisting of POPC/SM/Chol (50:25:25) were fixed at a constant, biological relevant, surface pressure of 30 mN m^{-1}. Figures 3.43(A) and 3.44(A) display the respective areas as a function of time. After ~30 min, the time necessary for the lipid film to achieve an equilibrium (corresponding to the decay of the curve profile), 50 µl of the protein were injected at a concentration of 400 nM. The corresponding IRRA spectra taken at 40° with *s*-polarized light are shown in Figures 3.43(B) and 3.44(B) (position 1). The amid I band, which is characteristic of the secondary structure of the N-Ras protein with a farnesyl and a hexadecyl anchor, shown in Figure 3.43(B), reveals a peak at ~1634 cm^{-1}, which is typical of a β-sheet structure. On the contrary, no amid I band for the N-Ras HDHDOMe is observable at all (Figure 3.44(B)), in spite of adding the same amount of the protein into the subphase at t = 75 min (position 1-2) for a second time. The addition of an other 50 µl into the subphase of N-Ras HDFarBodipy, taking place after ~55 min, was also recorded. The corresponding IRRA spectrum shows a broad shoulder due to the presence of α-helices next to the β-sheet structure. After 150 min, the area has still a value of 0.50 nm^2 molecule^{-1} as at the beginning of the measurement, but the amid I

band shows an increase of the α-helical structure. The area *vs*. time curve of N-Ras HDHDOMe shows a behaviour, which is similar to the one mentioned above: the area ($A =$ 0.45 nm^2 molecule^{-1}) remains constant with the time, and after ~190 min the amid I band for this Ras isoform also reveals β-sheet and α-helical secondary structures.

At constant surface pressure of 30 and 20 mN m^{-1} (data not shown), no adsorption at the air/D$_2$O interface for both proteins studied was detected. The appearance of the amid I band after the injection of the proteins suggests, though, that the anchors bind to the lipid monolayer. Since, when the number of protein molecules is approximated from the band intensity increase (ca. 0.00025 absorbance units), one comes to the conclusion that there is only one protein per 500 lipid molecules, i.e. the area should change by 0.2% only, which is outside the detection limit of the method.

At a constant surface pressure of 10 mN m^{-1}, the area of the N-Ras HDHDOMe increases, reaching a plateau after ~125 min ($A =$ 1.35 nm^2 molecule^{-1}). The corresponding maximal surface pressure reaches a value of ~17 mN m^{-1} in the presence of the lipid monolayer composed of POPC/SM/Chol (50:25:25). The amid I band intensity increases concomitantly by a factor of 2 and its maximum shifted to 1631 cm^{-1} (Figure 3.44(B), position 3), which indicates a reorientation of the protein from the random to orientation A (Figure 3.42a). The other protein isoform also shows an increase of the area at constant $\Pi =$ 10 mN m^{-1}. After ~ 240 min, however, a plateau is still not reached (data not shown). Apparently, at this pressure the protein was now able to insert into the lipid monolayer and reaches the air/D$_2$O interface. This was also evident from the much larger increase in intensity of the amide I band. Concomitantly, its maximum shifted slightly to 1632 cm^{-1} (Figure 3.43(B), position 3), which indicates a reorientation of the protein when inserted in between the lipids at the air/D$_2$O interface.

After the measurements performed at $\Pi =$ 10 mN m^{-1}, the lipid film was compressed back to the physiological surface pressure (30 mN m^{-1}). At this point, the two studied dually lipidated N-Ras proteins show a completely different behaviour. The N-Ras HDFarBodipy is entirely desorbed from the D$_2$O/air interface and removed from the lipid monolayer, as shown in Figure 3.43(B) position 10, i.e., the amid I band intensity totally disappears. Obviously, the protein was not inserted into the lipid monolayer in a stable fashion, indicating that the two anchors, one farnesyl and one hexadecyl, provide not enough gain in free energy to allow the protein to remain incorporated in the monolayer at high surface pressure. The N-Ras HDHDOMe isoform at $\Pi =$ 30 mN m^{-1} still shows a decrease of the area. The amid I band

intensity, however, grows, reaching an absolute value, which is twice the one observed for the measurements at Π = 10 mN m^{-1}. This indicates that the doubly hexadecylated protein remains inserted in between the lipid molecules in the monolayer and that some protein molecules are in contact with the air/D$_2$O interface. The comparison of measured and simulated angle-dependent spectra shows that this protein is inserted into the lipid monolayer with the same orientation as it is adsorbed at the air/D$_2$O interface.

Figures 3.45(A) and 3.45(B) depict the position of the CH$_2$ antisymmetric stretching mode at 2923.5 cm^{-1} and the CH$_2$ symmetric stretching mode at 2853 cm^{-1}. As we can clearly see, during the decompression cycles from 30 to 20 and to 10 mN m^{-1}, respectively, and the compression back to 30 mN m^{-1}, no significant shifts of the characteristic lipid bands are detected. The addition of the dually lipidated proteins do not influence the lipid monolayers phase, either.

Measurements at constant area Measurements were also carried out with 200 nM protein subphase concentration at constant area with a lipid film composed of POPC/SM/Chol (50:25:25) at a surface pressure of 10 mN m^{-1}. The N-Ras HDFarBodipy and the N-Ras HDHDOMe, respectively, were injected into the subphase 1 hour after the lipid film was prepared. The surface pressure increases immediately after the injection of the lipoproteins showing a similar behaviour which is also seen in the case without the presence of the lipid monolayer. Comparison of the two cases leads to the observation that the adsorption of the dually lipidated proteins at the air/D$_2$O interface is faster and the surface pressure is higher without the presence of a lipid monolayer. For N-Ras HDHDOMe, the surface pressure as a function of the time presents an analogous curve profile with and without the lipid monolayer: after 4 hours both graphs display a kink (Figures 3.47(A) and 3.41(A)). The kinetic process involved to reach the interface implicates many rearrangements in the orientation of the protein, in particular if the lipid monolayer is present, as we can also see in the corresponding amid I band intensities in Figure 3.47(B). According to the frequency shift of the amide I bands from 1635 to 1624 cm^{-1} the insertion of N-Ras wt 1-181 MIC7 HDHD into the lipid monolayer starts in a random way up to the first small surface pressure plateau and ends up in orientation A of the final surface pressure plateau. The bands taken at the position 2-5 of the corresponding surface pressure *vs.* time graph reveal strong intensity oscillations. The N-Ras HDFarBodipy also exhibits analogous intensity oscillations of the amid I bands (Figure 3.46(B)), at corresponding positions (3-6 and 7-10) of the surface pressure as a function of the time diagram, the curve profile shows no kinks, however (Figure 3.46(A)). The amid I bands with a frequency maximum of 1624 cm^{-1} indicates a preferred insertion in orientation A.

Again, the study of the position of the CH$_2$ antisymmetric stretching mode at 2923.5 cm^{-1} and the CH$_2$ symmetric stretching mode at 2853 cm^{-1} reveals that the lipid film composition is not influenced by the insertion of the proteins (Figures 3.48(A) and 3.48(B)).
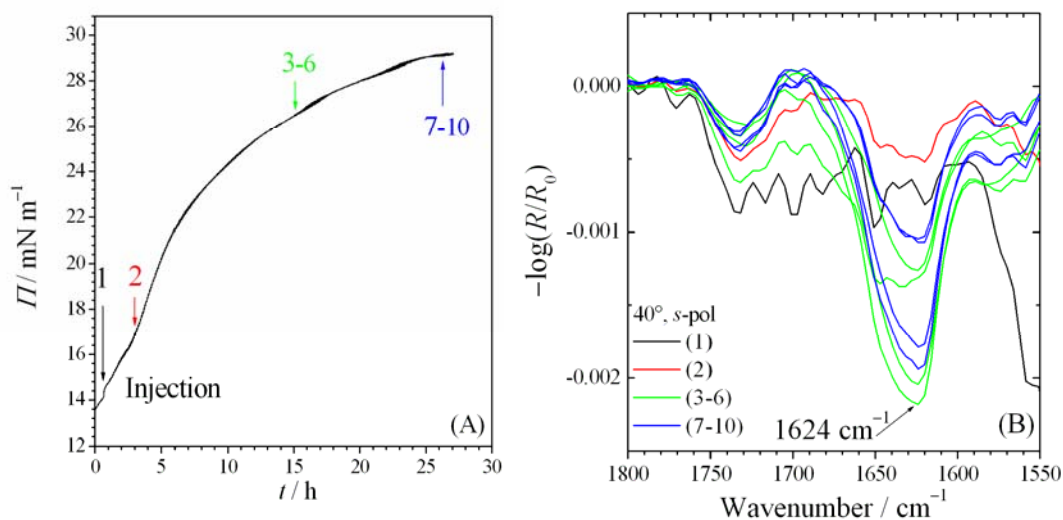
Figure 3.46 (A) Π/t isotherm of N-Ras MIC7 HDFarBodipy (c = 200 nM in 100 mM NaCl in D$_2$O, T = 20 °C) injected into the subphase of a lipid film composed of POPC/SM/Chol (50:25:25) having a constant area. (B) IRRA spectra (angle 40°, s-polarized light) of the same system at the respective positions 1-10 of the surface pressure/time curve in Figure 3.46(A).
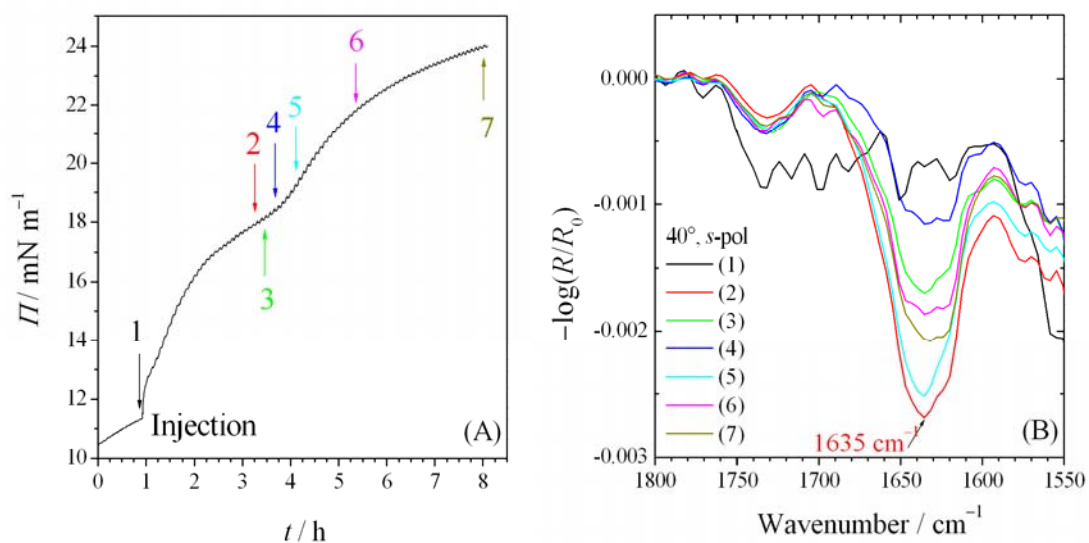
Figure 3.47 (A) Π / t isotherm of N-Ras MIC7 HDHDOMe (c = 200 nM in 100 mM NaCl in D_2O, T = 20 °C) injected into the subphase of a lipid film composed of POPC/SM/Chol (50:25:25) having a constant area. (B) IRRA spectra (angle 40°, s-polarized light) of the same system at the respective positions 1-7 of the surface pressure/time curve in Figure 3.47(A).
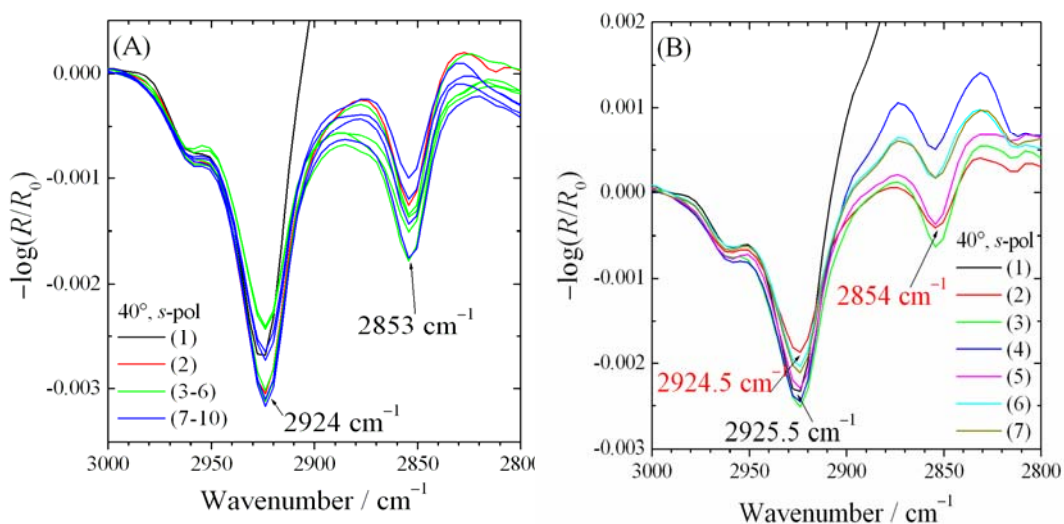
Figure 3.48 Examples of IRRA spectra of the lipid monolayer composed of POPC/SM/Chol (50:25:25), before and after the injection of the dually lipidated proteins (A) N-Ras MIC7 HDFarBodipy and (B) N-Ras MIC7 HDHDOMe, taken at constant area. The positions of the CH_2 antisymmetric stretching mode at 2923.5 cm^{-1} and the CH_2 symmetric stretching mode at 2853 cm^{-1} do not shift.

3.5.4 Conclusions

At first, the adsorption of N-Ras wt 1-181 HDFarBodipy at the air/D_2O interface was studied. The saturation value of the surface pressure, Π_{max}, approaches 24 mN m^{-1} corresponding to a concentration of 200 nM. This quantity was used for all other experiments.

The surface pressure as a function of time of the same protein isoform reaches a plateau after 22 h with Π_{max} = 19.5 mN m^{-1}. The corresponding angle dependent measurements clearly show that the amid I band has characteristic peaks typical for intramolecular β-sheets and α-helical secondary structure. Comparison with the simulated spectra reveals that the adsorption at the air/D_2O interface correspond to orientation A (Figure 3.42a). The same kind of experiments with N-Ras wt 1-181 MIC7 HDHDOMe reveal that its adsorption kinetics at the air/D_2O interface occurs faster and the amid I band of the IRRA spectra taken before Π = 13 mN m^{-1} are predominantly characterised by α-helical structure, then, until Π_{max} is reached, β-sheet structures appear. At low surface pressure the N-Ras wt 1-181 MIC7 HDHDOMe first adsorbed in a more random orientation and then changes its orientation with increasing surface pressure to orientation A.

The experiments with a lipid monolayer composed of the canonical raft mixture POPC/SM/Chol (50:25:25) at the biological relevant surface pressure of 30 mN m^{-1} reveals that the proteins bind to the lipid monolayer through their anchors, however the insertion process of N-Ras MIC7 HDFarBodipy into the lipid monolayer is faster than for the other protein isoform. At Π = 10 mN m^{-1}, both isoforms insert with their lipid anchors into the lipid monolayer a compression back to Π = 30 mN m^{-1} leads, however, to different behaviour. The farnesylated and hexadecylated protein is completely desorbed from the air/D_2O interface and removed from the lipid monolayer, no amid I band in the IRRA spectra is more detectable. On the contrary, the amid I band of the double hexadecylated protein still shows strong intensity, i.e. it remains attached with its anchors to the lipid monolayer. During the insertion process, changes in orientation of the protein were detected by comparison with simulated IRRA spectra. At high surface pressures, the N-Ras wt 1-181 MIC7 HDFarBodipy inserts in orientation A. However, the protein is not inserted into the lipid monolayer in a stable fashion, indicating only little gain in free energy upon insertion into the lipid monolayer. On the contrary, the dually hexadecylated protein N-Ras wt 1-181 MIC7 HDHDOMe remains inserted in between the lipid molecules in the monolayer even at high surface pressures. Its insertion into the lipid monolayer starts in a random fashion and ends up in orientation A.

3.6 Temperature study of the effects of various chaotropic and kosmotropic cosolvents on a minimum elastin-like polypeptide GVG(VPGVG) by CD and FTIR spectroscopy

3.6.1 Introduction

Elastin, a principle protein component in vertebra's connective tissues, and its precursor tropoelastin feature very unusual viscoelastic properties (URRY, 1993; URRY, 1997). Most interesting is the peculiar feature that folding of these proteins is achieved by increasing the temperature beyond 40 °C. The term "inverse temperature transition" (ITT) was coined for this apparently paradoxical change from a disordered (extended) to an "ordered" (folded) conformation upon heating. To understand this phenomenon, the total system, i.e. the protein with its surrounding hydration sphere, should be considered. This suggests that the structural and dynamic properties of water markedly influence the protein's behaviour, as already pointed out in the theoretical work of Rousseau *et al.* (ROUSSEAU, 2004). Interestingly, it has been indicated that protein-based polymers comprised of the elastine's particular properties are capable of performing many of the energy conversions that sustain life and may be used for designing biomolecular machines (URRY, 1997).

In general the stability of proteins depends on temperature, solvent properties, and its hydration capacity. The phenomenon of protein hydration is not regarded as a rigid shell of water around a protein molecule, but rather as a fluctuating cloud of water molecules that are thermodynamically affected more or less strongly by the protein molecule (TIMASHEFF, 2002). Apart from water, proteins are normally surrounded by other solvent components, such as buffer salts and stabilizers/denaturants, the so-called "cosolvents". Generally, they alter proteins equilibria and reaction kinetics by perturbing the chemical potential, in which they associate either more strongly or more weakly with the protein than with water ("preferential binding"). Thermodynamically, when a cosolvent is added to an aqueous solution of protein, the water activity is lowered by the colligative effect and cosolvent molecules enter in interactions with the protein. The chemical potential of the protein (μ_p) is then altered by the following relationship:

$$\Delta\mu_{p,tr} = \int_0^{m_x} \left(\frac{\partial\mu_p}{\partial m_x} \right)_{T,p,m_p} dm_x \qquad\qquad (3.1)$$

$$= -\int_0^{m_x} \left(\frac{\partial \mu_x}{\partial m_x} \right)_{T,p,m_p} \left(\frac{\partial m_x}{\partial m_p} \right)_{T,p,\mu_x} dm_x \tag{3.2}$$

in which $\Delta \mu_{p,tr}$ is the transfer free energy of the protein from the pure water into the mixed solvent system, m is molality, and subscripts x and p identify the cosolvent and protein, respectively. Two partial derivates appear in equation (3.2): the first one explains the dependence of the cosolvent chemical potential on cosolvent molality, while the second is the "preferential binding coefficient", Γ_{xp}

$$\Gamma_{xp} \equiv \left(\frac{\partial m_x}{\partial m_p} \right)_{T,p,\mu_x} \tag{3.3}$$

If $\Gamma_{xp} > 0$, i.e. the interaction is favourable, there will be an excess of cosolvents in the vicinity of the protein than in bulk solvent. Denaturants, such as urea and guanidinium chloride show this type of behaviour. Reciprocally, for sugars, $\Gamma_{xp} < 0$, i.e. the interaction is unfavourable, and there is a deficiency of cosolvent around the protein relative to the bulk solvent.

A protein in aqueous medium is fully hydrated. If it binds to a ligand (cosolvent), a replacement of water molecules must occur. For the equilibrium R $\leftrightarrow$ Pr (Reactant $\leftrightarrow$ Product), this change is equal to the change in the transfer energy of the protein from water to the cosolvent system. Therefore, the measured standard free energy of binding, ΔG_b^0, is an exchange free energy, ΔG_{ex}^0. This is the difference between the hypothetical free energy of binding of cosolvent, ΔG_x^0, and water, ΔG_w^0, respectively, to a dry site on the protein dissolved in the mixed solvent:

$$\Delta G_{ex}^0 = \Delta G_x^{0(R-Pr)} - \Delta G_w^{0(R-Pr)} = \Delta \mu_{p,tr}^{Pr} - \Delta \mu_{p,tr}^{R} \tag{3.4}$$

The effect of the cosolvent is examined best through the variation of the equilibrium constant (K) and its relation to the change in the preferential interaction parameter during the course of the reaction, namely trough the Wyman linkage reaction (WYMAN, 1964):

$$\left(\frac{\partial \ln K}{\partial \ln a_x}\right)_{T,p,m_p} = \frac{\left(\partial \mu_x / \partial m_p\right)^R_{T,p,m_x} - \left(\partial \mu_x / \partial m_p\right)^{Pr}_{T,p,m_x}}{\left(\partial \mu_x / \partial m_x\right)_{T,p,m_p}} = \Delta\left(\frac{\partial m_x}{\partial m_p}\right)_{T,p,m_x} \qquad (3.5)$$

The Wyman plot ($\ln K$ vs $\ln a_x$) is determined by the change in preferential binding in the course of the reaction, at any given cosolvent concentration. Since the slope of the Wyman plots may be positive (enhancer), negative (inhibitor), or zero (no effect), it defines the direction in which a cosolvent displaces the equilibrium (TIMASHEFF, 1993).

During the last decade, there have been a large number of observations on the effect of the organic cosolvent 2,2,2-Trifluorethanol (TFE). TFE has been shown to act as an indirect chaotrope disrupting the solvent shell on α-helices (LUO, 1998), but also as a kosmotrope where its desolvating effect destabilizes the unfolded state (KENTSIS, 1998; STORRS, 1992). There are in literatures contrasting views concerning the effect of TFE on peptides and proteins. On the one hand TFE strengthens local hydrophobic interactions in α-helices (SÖNNICHSEN, 1992; BLANCO, 1994), β-turns and β-hairpins (REIERSEN, 1998) on the other hand there is a lack of experimental evidence that TFE actually binds to hydrophobic groups (STORRS, 1992). Again, TFE disrupts tertiary interactions in proteins, while preserving secondary structure (LUO, 1998). A structural model was proposed by Reiersen *et al*. in studies with an elastin peptide in TFE solutions at different temperatures. TFE forms clusters at low concentration (TFE <50%), which locally assist the folding of secondary structures by first breaking down interfacial water molecules on the peptide and then providing a solvent matrix for further side chain-side chain interactions. The differences in cluster size, dependent on TFE concentration, may also explain why TFE-induced transitions between secondary structures at concentrations >50% (REIERSEN, 2000).

The Hofmeister series characterizes some properties of ions as cosolvents in protein solutions. In this series the ions are divided into two groups: kosmotropic and chaotropic. The protein is salted out, i.e. stabilized, by kosmotropic ions and salted in, i.e. destabilized, by chaotropic ions (CACACE, 1997). Reduction of the net charge of proteins via salts acting as

counterions (screening effect), is an additional important effect of salts on protein stability (RAMOS, 2002).

In this work temperature dependent effects of different cosolvents (glycerol, TFE, urea, GuHCl and LiI) on the structure properties of the octapeptide GVG(VPGVG) elastin-like model system, which behaves undergoes an inverse-temperature folding transition, are explored. The use of chemical stabilizers and denaturants in this particular case could behave in a different way as for other proteins like lysozyme, SNase or RNase A.

3.6.2 Glycerol and TFE

Glycerol and other polyolic cosolvents have been shown to enhance protein stability. This implies a preferential hydration of the protein, i.e., the exclusion of the cosolvent molecules from the protein surface. In contrast, alcohols like TFE can act as a kosmotrope or as chaotrope.

Figures 3.49(A), 3.49(B), and 3.49(C) show CD spectra of the GVG(VPGVG) peptide (0.5 mg/mL in 10 mM phosphate buffer pH 7.0) in buffer solution only, in 2 M glycerol and in 2 M TFE, respectively, taken at different temperatures. At 2 °C, all the spectra depict a similar shape consisting of a large negative band at ~197 nm and a weak one at ~221 nm (Figure 3.50(A)). A pure random structure is in CD-spectroscopy normally characterised by a strong negative band at ~197 nm with a larger minimum mean residual (MRE) value (–40000 ° cm^2 dmol^{-1}). CD-studies conducted on the octamer in pure buffer solution show a MRE of –7000 ° cm^2 dmol^{-1}. This fact indicates the presence of still some remaining order, as already discussed in other works (REIERSEN, 1998). The addition of a small quantity of a polyolic solvent such as 0.5 M glycerol does not change markedly the shape and the MRE average values of the spectra as adding 0.5 M TFE, 2 M TFE or 2 M glycerol (Figures 3.50(A)). In the latter cases, the MREs shift to higher values ~–5700 ° cm^2 dmol^{-1}, the amount of disordered structures decrease by ~18% in comparison to that of the octamer in pure buffer solution. In all cases studied, an isodichroic point which indicates the presence of two main conformational states, is observed at ~212 nm upon heating. When the temperature increases, the amplitude of the band with the absolute minimum decreases moving to larger residual ellipticity values (Figures 3.51(A), 3.51(B), 3.51(C), and 3.51(D)), while the shallow minimum at ~221 nm together with the development of a positive peak in the 206-212 nm spectral region, characteristic of type II β-turns, increases concomitantly (PERCZEL, 1993).
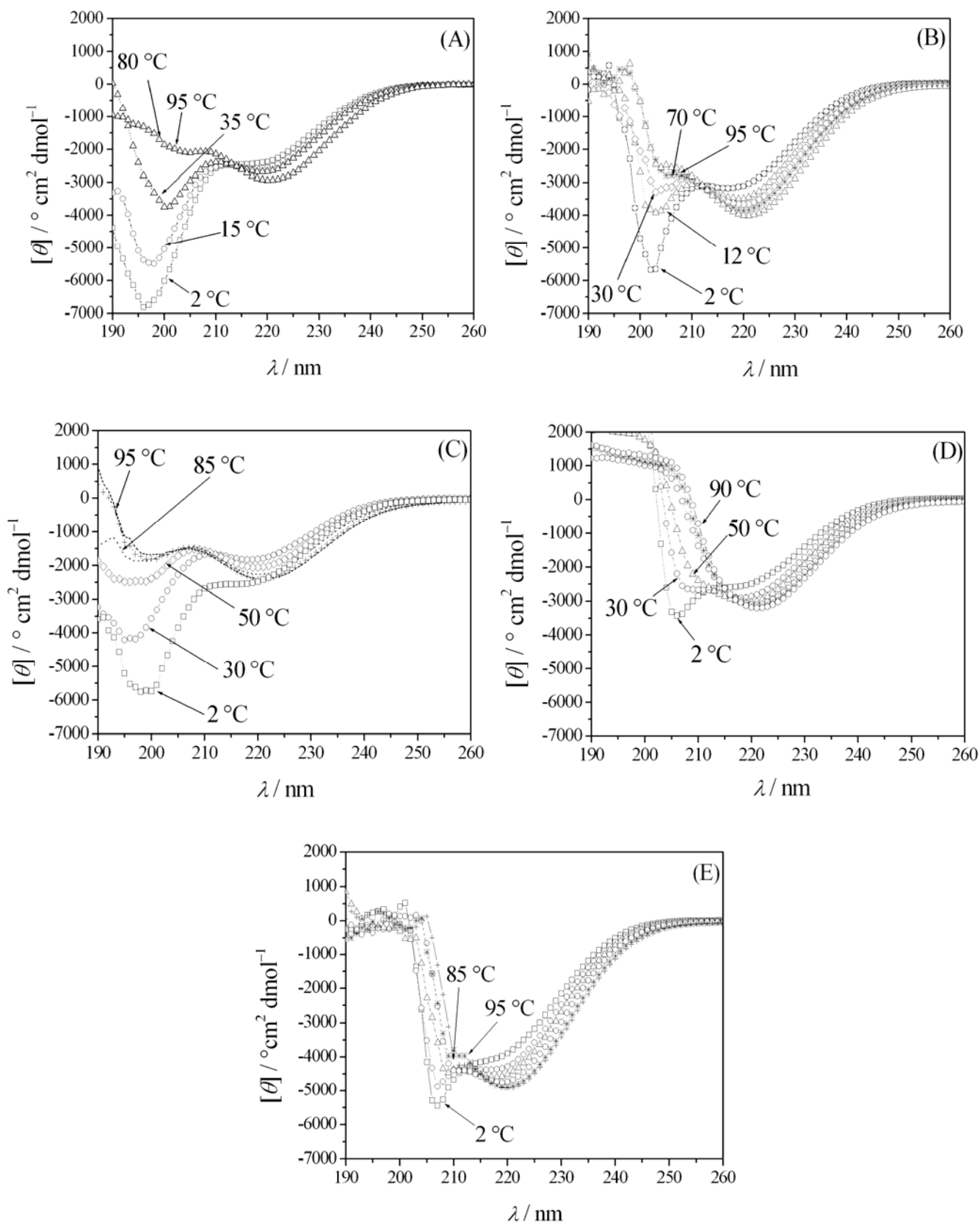
Figure 3.49 CD spectra of the peptide GVG(VPGVG) at selected temperatures in the temperature range from 2 to 95 °C (0.5 mg/mL peptide in 10 mM phosphate buffer with different cosolvents, pH 7.0). (A) without cosolvent; (B) in 2 M glycerol; (C) in 2 M TFE; (D) in 0.5 M urea and (E) in 0.5 M GuHCl.
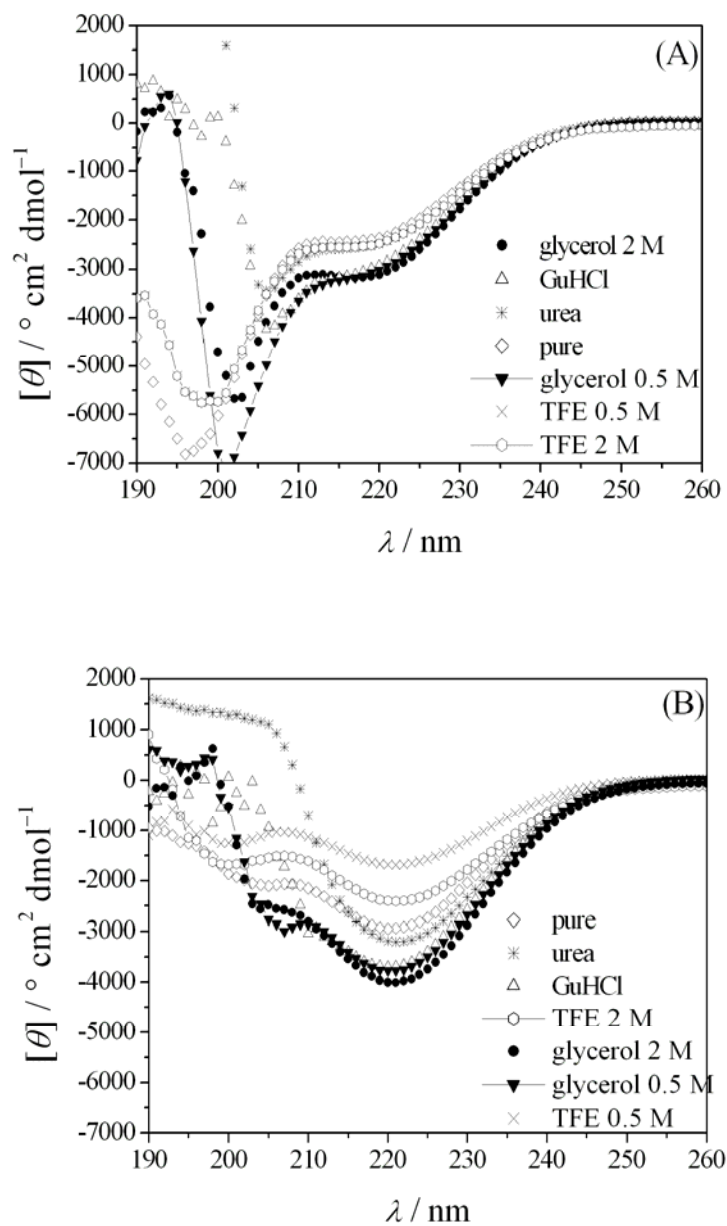
Figure 3.50 CD spectra of the peptide GVG(VPGVG) (0.5 mg/mL peptide in 10 mM phosphate buffer with different cosolvents, pH 7.0); (A) at a low temperature (~2 °C) and (B) at a high temperature ~95 °C.
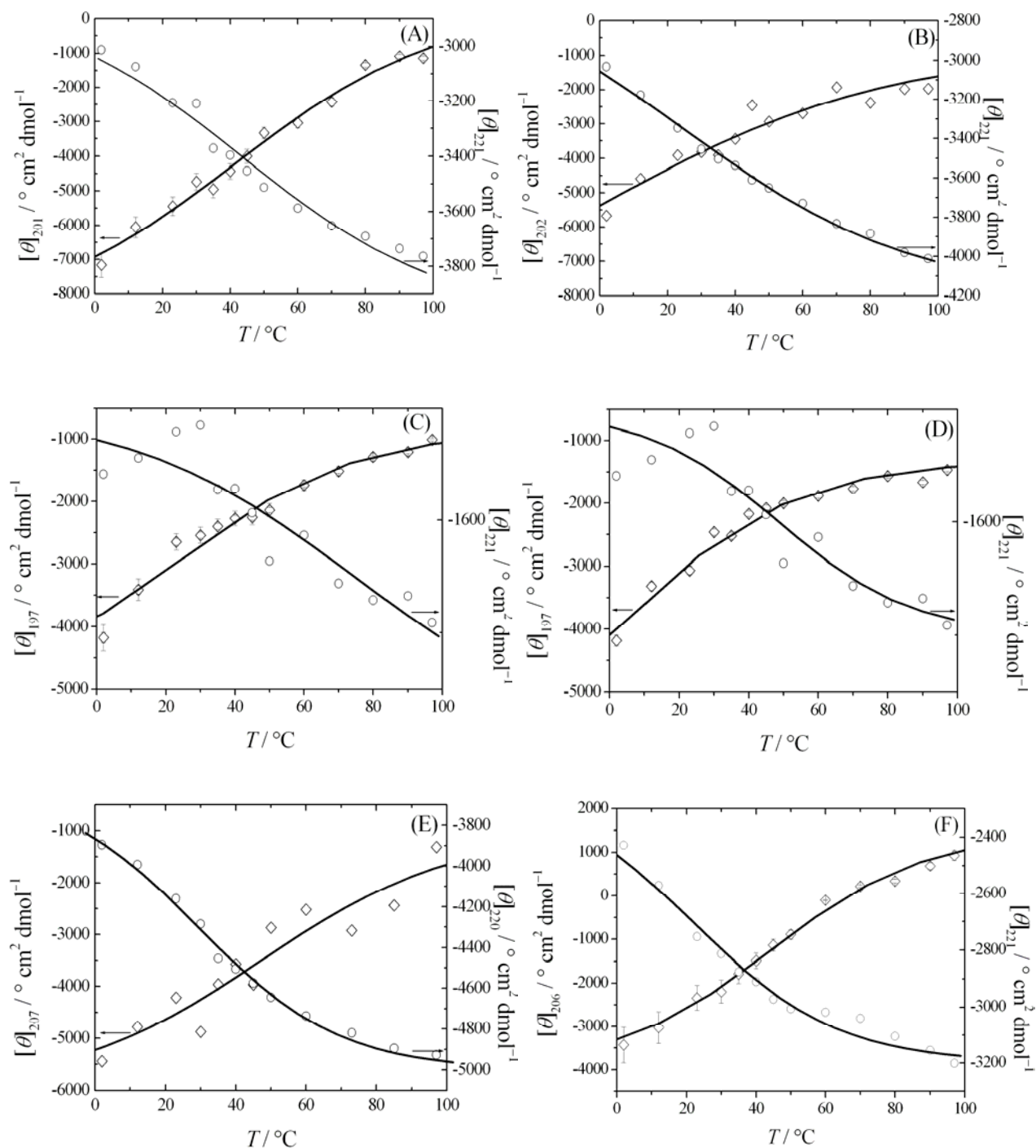
Figure 3.51 Temperature dependence of the mean residual ellipticity of the peptide GVG(VPGVG) (0.5 mg/mL in 10 mM phosphate buffer pH 7.0 and (A) 0.5 M glycerol, (B) 2 M glycerol, (C) 0.5 M TFE, (D) 2 M TFE, (E) 0.5 M GuHCl and (F) 0.5 M urea) between 197-207 nm (◊) and ~221 nm (o), respectively. The data were fitted with a sigmoidal function.

The convex constraint algorithm (CCA) is used for the analysis of the secondary structure elements. This method examines the CD spectra of the spectral region between 195 and 240 nm and deconvolutes them in their pure components, which are chosen *a priori*. At first, different numbers of pure components (P) were tried for the deconvolution. The use of higher numbers of components delivered unreasonable and unsystematic results. A reasonable good fit according to the root-mean square value which remains <25 in this case, is obtained only for $P = 2$. The choice of two pure components is also supported by the appearance of an isodichroic point. As shown in Figures 3.52(A) and 3.52(B), in all the studied cases two main conformational states are detected. The state dominating at low temperatures consisting of disordered structures decreases in 0.5 M glycerol by 57 ± 15% upon increasing temperature up to 90 °C, whereas in 0.5 M TFE, 2 M glycerol, and TFE by 30 ± 8%, 33 ± 7%, and 27 ± 6%, respectively. Concomitantly the second state, consisting of type II β-turns, prevails at higher temperatures and increases by the same amount increasing temperature.

The full reversibility of all the systems was tested by heating the sample up to 90 °C and followed by a rapid cooling to 20 °C.

3.6.3   Urea and GuHCl

Denaturation is induced by using cosolvents which directly bind to particular groups of proteins, for example, to peptide groups in the case of urea. Measurements of the GVG(VPGVG) peptide in urea and GuHCl are carried out to explore the behaviour of an inverse-temperature folding transition peptide in the presence of common denaturant agents.

The CD spectra of the GVG(VPGVG) peptide 0.5 mg/mL in 10 mM phosphate buffer and 0.5 M urea and GuHCl, respectively, at pH 7.0, taken at various temperatures, are shown in Figures 3.49(D) and 3.49(E). In comparison to the octamer in pure buffer solution, the minimum of the spectra, containing denaturant agents, shifts to higher wavelengths, from 197 nm to ~206 nm at low temperature; its MRE has an average value of ~−4400 ° cm^2 dmol^{-1}. Upon increasing temperature, the curves show a behaviour similar to that seen with glycerol and TFE: the negative band decreases at ~206 nm, while the negative peak increases in amplitude at 220 nm (Figures 3.51(E), 3.51(F)). The concomitant development of a positive peak at 206-212 nm, however, which together with the negative band at 206 nm are characteristic of type II β-turns, does not appear for these cosolvents anymore (Figure 3.50(B)). The deconvoluted CD-spectra, in their pure components, using the convex constraint algorithm, clearly show features no more typical of type II β-turns at low

temperatures, they are probably due to other turn/loop structures, since prolines and glycines have a poor tendency to form α-helices or β-sheets (URRY, 1993).

Again, the presence of an isodichroic point at 212 nm is useful for the analysis of the secondary structure, that is why $P = 2$ as number of pure components was chosen. Figure 3.52(C) presents the changes of the relative intensities of the secondary structure in dependence of temperature. The effect of the denaturant agents like 0.5 M urea and 0.5 M GuHCl on a small peptide like GVG(VPGVG) is quite clear: at 2 °C, the dominant structures are already turns/loops with a small quantity, ~8 ± 2% and 27 ± 8%, respectively, of unordered structure which remains stable upon increasing temperature.

The complete reversibility of the conformational transitions was tested by heating the sample to 90 °C and subsequent rapid cooling to 20 °C (Figure 3.53).
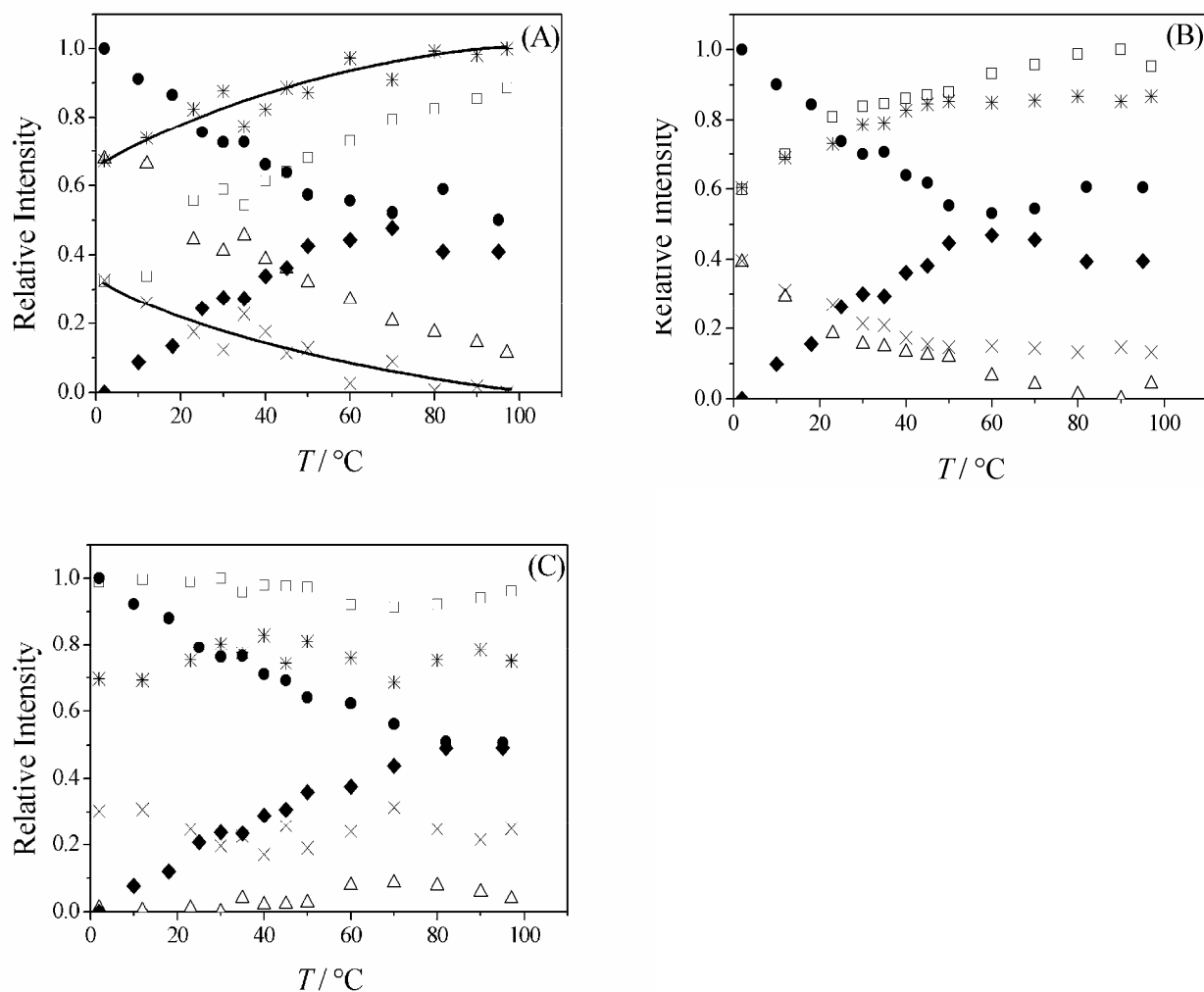
Figure 3.52 Temperature dependence of the relative intensities of the secondary structure elements of GVG(VPGVG) (0.5 mg/mL peptide in 10 mM phosphate buffer with different cosolvents, pH 7.0); (A) 0.5 M glycerol (□ = turns; Δ = disordered structure), 2 M glycerol (∗ = turns; × = disordered structure), and pure buffer solution (♦ = turns; ● = disordered structure); (B) 0.5 M TFE (□ = turns; Δ = disordered structure), 2 M TFE (∗ = turns; × = disordered structure), and pure buffer solution (♦ = turns; ● = disordered structure); (C) 0.5 M urea (□ = turns; Δ = disordered structure), 0.5 M GuHCl (∗ = turns; × = disordered structure), and pure buffer solution (♦ = turns; ● = disordered structure).
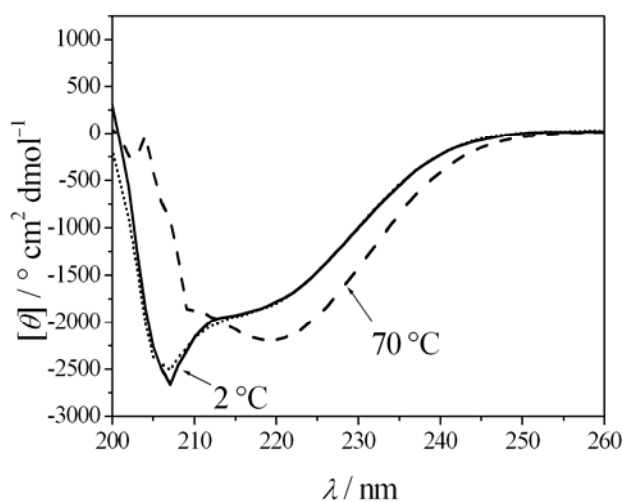
Figure 3.53 CD spectra of the peptide GVG(VPGVG) (0.5 mg/mL in 10 mM phosphate buffer and 0.5 M GuHCl, pH = 7.0) at 2 °C before heating (—), at 70 °C (- -), and after rapid cooling back to 2 °C (····).

3.6.4   Temperature dependent FTIR spectroscopic measurements

LiI   Experiments are carried out to measure the effect of the temperature on the secondary structure of GVG(VPGVG) in the presence of LiI at two different concentrations: 0.5 M and 2 M. The temperature-induced changes in the amide I′ region (1575 to 1700 cm^{-1}) of the infrared spectrum were measured in the temperature range between 2 °C and 95 °C using D$_2$O as solvent at pD 7.0 (Figure 3.54). The secondary structure elements are assigned to IR bands as summarized in Table 3.1 (TAMM, 1997). The band at ~1673 cm^{-1} can be assigned to type II β-turns, the band at 1656 cm^{-1} is associated with turn and loop structures, and the band at 1641 cm^{-1} is assigned to disordered structures (no α-helices can be formed for this small peptide). The other band, which appears at 1617 cm^{-1}, is probably due to the IR absorption of the terminal COO$^-$ group.

The deconvoluted IR spectra of GVG(VPGVG) with 0.5 M and 2 M LiI, respectively, are characterized by a maximum at 1673 cm^{-1} at all temperatures, which is a feature of type II β-turns. The intensity of this band decreases with increasing temperature and shifts to larger wavenumbers. The evolution of the secondary structure of GVG(VPGVG) as a function of temperature, as obtained by fitting the spectra using five subcomponents according to the data given in Table 3.1, is shown in Figure 3.55. Within experimental error, the fractional

intensities of loops/turns are constant and are therefore not included in the plot. In the case of the solution containing 0.5 M LiI, a decrease (~5%) of disordered structures and a concomitant increase in turn structures is observed upon increasing the temperature up to ~20 °C. In comparison to the pure peptide in buffer solution a low concentration of salt leads to smaller changes of the secondary structure, though the trend of the transformation is still the same: the fraction of disordered structures decrease by increasing the temperature. The system GVG(VPGVG) in 2 M LiI shows another behaviour, however: a ~ 13% less fraction of disordered structures, and a larger fraction of turns, respectively, than with 0.5 M LiI is detected at 2 °C. As shown in Figure 3.55(C), changes in temperature leave the secondary structure unchanged throughout the spectrum.
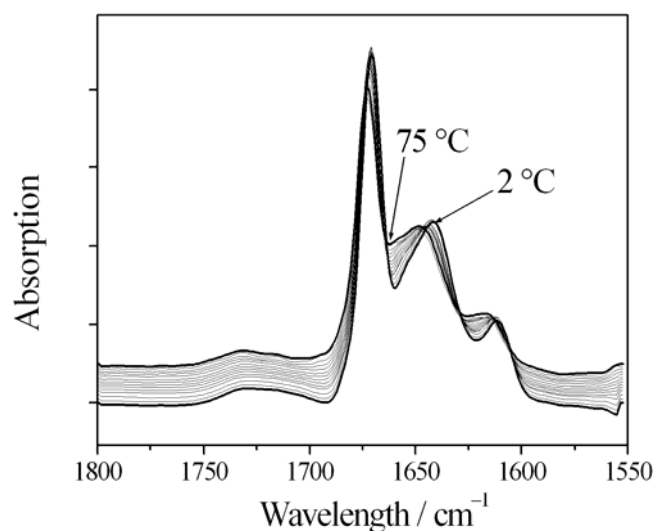
Figure 3.54 Deconvoluted FTIR absorption spectra of the peptide GVG(VPGVG) (5% (w/w) in 10 mM phosphate buffer and 2 M LiI, pD 7.0) as a function of temperature at ambient pressure.

Table 3.1 Wavenumbers of secondary structure elements in the amide I′ infrared region (TAMM, 1997)

Secondary structure element	Wavenumber / cm^{-1}
extended β-chains	1615-1628
β-sheets	1625-1640
disordered structures (random coil)	1640-1650
α-helices or loops/turns	1650-1658
turns (β- und γ-turns)	1660-1690
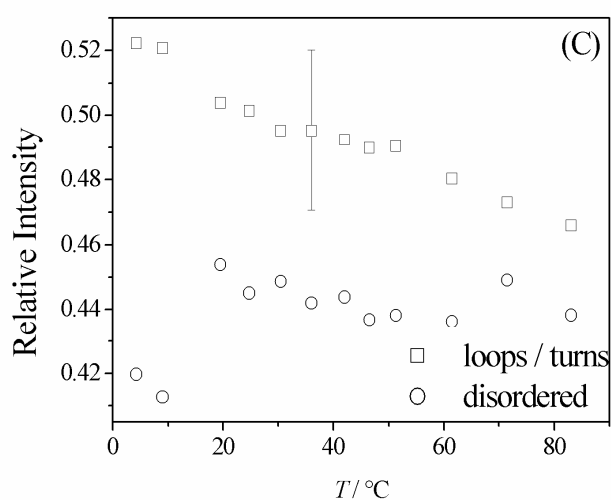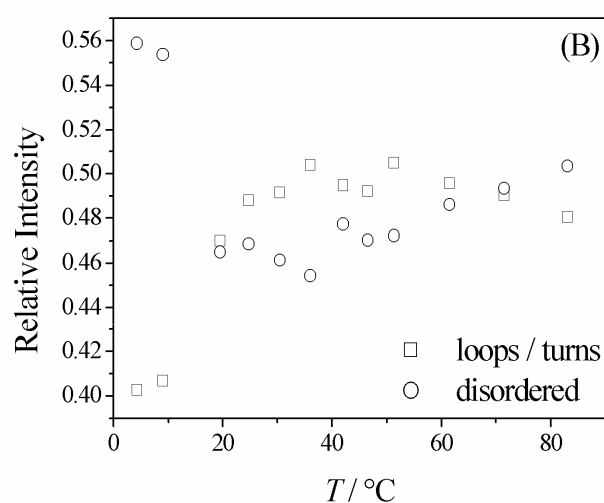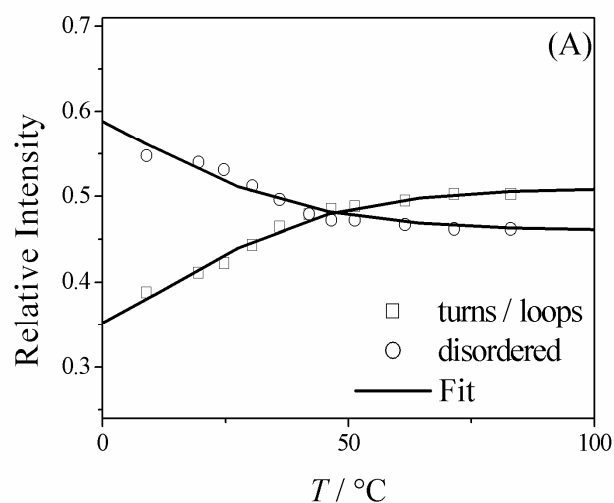
Figure 3.55 Temperature dependence of the relative intensities of secondary structure elements (□: loops/turns, ○: disordered structures) of GVG(VPGVG) in (A) pure buffer, data fit with a sigmoidal function, (B) 0.5 M LiI and (C) 2 M LiI as obtained from the FTIR data.

3.6.5   Thermodynamic analysis

In order to determine the standard Gibbs free-energy change, ΔG^0, of the conformational transition as well as the corresponding enthalpy and entropy changes, the temperature dependent CD data (at 197 nm for glycerol and TFE and at 220 nm for urea and GuHCl) and FTIR data (Figures 3.51, 3.55(A), and 3.55(B), respectively) were fitted to a two-state model. The van't Hoff plot (plot of $\ln K$ *vs.* $1 / T$, K being the equilibrium constant) as obtained from the CD and FTIR curves (data not shown) was constructed from $K = ([\theta]^{\text{obs}} - [\theta]^{\text{U}})/([\theta]^{\text{F}} - [\theta]^{\text{obs}})$, where $[\theta]^{\text{obs}}$ are the CD and FTIR data for the experimentally observed ellipticity and relative intensities, respectively, and $[\theta]^{\text{F}}$, $[\theta]^{\text{U}}$ the values for the previously fitted endpoints of the transition (high-temperature folded form, $[\theta]^{\text{F}}$, and low-temperature unfolded form $[\theta]^{\text{U}}$. The data for ΔG^0, the enthalpy changes ΔH^0 and entropy changes ΔS^0 are shown in Tables 3.2 and 3.3 for $T = 23$ °C. Positive enthalpy and entropy changes are obtained at room temperature for all cosolvents.

Table 3.2 Thermodynamic values of the temperature-induced conformational transition of the peptide GVG(VPGVG) as obtained from the CD-spectroscopy data.

	ΔH^0 / kJ·mol^{-1}	ΔG^0 / kJ·mol^{-1}	ΔS^0 / kJ·mol^{-1}K^{-1}	T_{m} / °C
buffer only	37 ± 16	2.21 ± 0.95	0.12 ± 0.05	41
0.5 M Glycerol	27 ± 3.5	1.26 ± 0.16	0.09 ± 0.02	38
2 M Glycerol	18 ± 2.4	−2.36 ± 0.40	0.06 ± 0.01	40
0.5 M GuHCl	32 ± 6	0.79 ± 0.14	0.11 ± 0.02	30
0.5 M TFE	17 ± 6	−0.32 ± 0.11	0.06 ± 0.02	24
2 M TFE	34 ± 4	−1.96 ± 0.20	0.12 ± 0.01	13
0.5 M Urea	37 ± 4	2.06 ± 0.25	0.12 ± 0.01	40

Table 3.3 Thermodynamic values of the temperature-induced conformational transition of the peptide GVG(VPGVG) as obtained from the FTIR spectroscopy data.

	ΔH^0 / kJ mol^{-1}	ΔG^0 / kJ mol^{-1}	ΔS^0 / kJ mol^{-1}K^{-1}	T_{m} / °C
buffer only	45 ± 8	3.72 ± 0.67	0.14 ± 0.02	51.6
0.5 M LiI	104 ± 19	3.94 ± 0.71	0.34 ± 0.06	36.3

3.6.6   Conclusions

In this study the behaviour of the oligopeptide GVG(VPGVG), which serves as a minimalistic elastin-like model system, has been investigated in the presence of osmolytes and denaturants applying CD and FTIR spectroscopy in a temperature range between 2 and ~95 °C.

The pure peptide behaves as a two-state system which undergoes an inverse-temperature folding transition occurring over a broad temperature range around $T \approx 36$ °C (NICOLINI, 2004). The addition of a small quantity of a polyolic solvent like, 0.5 M glycerol, does not influence the system considerably, whereas measurements at higher concentrations lead to an increase of the MREs. This indicates, that in comparison with the pure octamer, less random structures are present at similar temperatures. For both studied concentrations, TFE as well as LiI act in a kosmotropic manner, stabilizing type II β-turns also at lower temperatures. The thermodynamic analysis at room temperature still shows positive enthalpy and entropy changes for these systems, suggesting that the folding is a consequence of hydrophobic interactions being largely driven by the increase in entropy of water. The temperature folding transitions happen over a broad temperature range and for the solutions containing TFE they occur at lower temperatures than for the elastin-like octamer in pure buffer solution or in glycerol.

As expected, common denaturants like urea and GuHCl act differently upon the secondary structure of the peptide. Instead to stabilize the disordered structure they induce turns/loops at $T = 2$ °C. The type II β-turns do not appear anymore also at higher temperatures. The form of the CD spectra, however, does not exclude the possibility of intramolecular β-sheets, which could develop in solution from peptide-peptide associations to dimer or larger aggregates. MD simulation data (conducted by Aliaksei Krukau) support an increase in the hydrophobicity of the peptide in studies of GVG(VPGVG)$_3$ in urea; the presence of guanidinium ions, however, immediately destroys the secondary structure of the peptide.

4   General Conclusions

One of the current challenges in bioscience is the convergence of experimental parameters to the complexity of living systems. In this context, the study of microdomains has become an important topic in the last years. Part of this work concerns the study of such raft-type domains *in vitro* and their properties in dependence of temperature, pressure and lipid composition by using different methods. In the first part of this dissertation the *p*, *T*-phase diagram of the lipid raft mixture POPC/SM/Chol (33:33:33) was built by using Fourier transform infrared and small angle x-rays scattering techniques. The liquid disordered/liquid ordered + (solid ordered) phase coexistence region extends over a rather wide temperature range of about 40 °C. Above ~50 °C, an overall fluid phase is reached. Upon pressurization at room temperature, an overall (liquid- and solid-) ordered membrane state with high ordering of their acyl chains is reached at pressures of about 1 kbar. In the small-angle neutron scattering (SANS) experiments the ternary model raft mixture DOPC(POPC)/SM/Chol (33:33:33) clearly demonstrate the existence of microdomains also down to the size of several nanometres. From the biological point of view, the results presented in this work support the notion that rafts can well be studied using three-component mixtures as model.

The second topic of this doctoral thesis focused on pressure dependent experiments on model biomembranes such as POPC/DLPC (50:50), DOPC/DPPC/Chol (34.5:34.5:31) and DOPC/SM/Chol (33:33:33). The measurements are carried out from 1 bar up to ~3000 bar by using two-photon excitation fluorescence microscopy and small angle x-ray scattering. The two-photon excitation fluorescence microscopy studies in thin fused silica capillary permit to visualize local and morphological changes in the membrane of GUVs due to high pressure perturbation The lipid phase state of the vesicles are detected by using Laurdan as fluorescence label, calculating the *GP* values of the GUVs and extracting their average value.

During the compression cycle, the *GP* value increases, indicating an increasingly tighter packing of the lipids. The tree systems show phenomena of budding and fission, at low pressure of 200-300 bar. The budding process is not directly related to phase transitions to an overall ordered conformation state of the lipid membrane, which occur at much higher pressure for all the system studied. The budding and fission of small daughter vesicles probably occurs in order to decrease the pressure-induced rise of line tension between domains. The topological changes of the lipid vesicles exhibit a different behaviour depending

if the pressure is increased or decreased. Upon decreasing pressure, the vesicle starts to "crack" as the packing of the lipids becomes less tight and the fluid phase region starts to build up. However, the vesicle cannot absorb the amount of water that was ejected during the compression cycle during the time-course of the experiment, and therefore the membranes of the GUVs lose their tension, leading to spherical-ellipsoidal-polygonal shape transitions of the membrane surface and fission of lipid material. The raft lipid mixtures containing more than 30 mol% cholesterol maintain mostly a spherical-ellipsoidal shape upon compression and decompression, though. The changes in *GP* value mostly occur in the same pressure range where also SAXS data exhibit characteristic changes on the lipid conformation and phase state.

It has been observed in natural membrane environments that in a pressure range of 1-2 kbar membrane protein functions cease. At these pressures the membrane matrix reaches a physiologically unacceptable overall ordered state. As demonstrated in this chapter, this might also be due to pressure induced morphological changes of the membrane.

The third part dealts with protein/membrane interactions studied in GUVs and monolayers. Various coexisting lipid phases ($l_o + l_d$, $l_o + s_o$, and $l_d + l_o + s_o$) were prepared by mixing different lipid mixtures of the system palmitoylphosphatidylcholine, sphingomyelin and cholesterol. The two-channels fluorescence microscopy experiments reveal that the partitioning of hexadecylated and farnesylated N-Ras (N-Ras wt 1-181 MIC7 HDFarBodipy) to mixed-domain lipid vesicles occurs following a similar order: $l_d > l_o >> s_o$. The binding kinetics of incorporation into the fluid lipid bilayer membrane also reflects this behaviour. In fact, binding to l_o domains is about 60% slower than into l_d regions. and binding of N-Ras into s_o domains, in a $l_o + s_o$ mixed-domain lipid system, is ~40% slower than into l_o domains. However, studies on the same systems, as revealed by the better spatial resolution of the AFM, show that the lipidated protein is located in the boundary region of the domains in mixed-phase liquid-ordered/liquid-disordered bilayers to a large extent. This leads to a favourable decrease in line energy (tension) which is associated with the rim of the demixed phases.

Such an interfacial adsorption effect of inserting proteins can be generally expected in many-phase lipid systems that have no particular preferences for any particular phase (DUMAS, 1997; MOURITSEN, 2005) - for example due to hydrophobic mismatch - so that the proteins are expelled to the boundary. It is clear that the localization and accumulation of

proteins in the interfaces of a lipid bilayer with domains may provide special strong direct protein-protein interactions and, thus, may serve as a vehicle for protein association. Whereas protein-protein interactions maintain many signalling complexes, specific modifications are believed to be sufficient to sequester proteins in lipid rafts and caveolae. The collected data indicate that, at least for N-Ras in canonical three-component lipid raft mixtures, a possible mechanism for effective protein-protein interactions could also be a collective association in the interfacial region of lipid domains.

Infrared reflection absorption spectroscopy (IRRAS) experiments reveal the orientation and partitioning of a farnesylated and hexadecylated (N-Ras wt 1-181 MIC7 HDFarBodipy) and a doubly hexadecylated (N-Ras wt 1-181 MIC7 HDHDOMe) N-Ras protein, respectively. Simulation studies together with the experimental data reveal that both N-Ras proteins adsorb at the air/D_2O interface in the same way, corresponding to a characteristic orientation A (see Figure 3.42a). The HDHD isomer, however, at low surface pressures, adsorb first in a more random orientation, pointing to a different adsorption kinetics due to the different lipid patterns of the two protein isomers. The insertion experiments into a Langmuir monolayer consisting of the lipid mixture POPC/SM/Chol (50:25:25) show that the lipid anchors of both proteins insert into the lipid monolayer below a surface pressure of 20 mN m^{-1}. At 30 mN m^{-1}, which is supposed to be equivalent to lipid bilayer conditions, the farnesylated and hexadecylated N-Ras protein desorbs completely from the monolayer, whereas the doubly hexadecylated protein remains incorporated into the lipid monolayer. The insertion process shows changes in the orientation of the protein in comparison to simulated IRRA spectra. Moreover, at high surface pressures, the HDFar inserts in orientation A into the lipid monolayer, but not in a stable fashion, pointing that this isomer provides only little gain in free energy upon insertion into the lipid monolayer. The N-Ras HDHDOMe, on the contrary, inserts in between the lipid monolayer even at high surface pressures, at first in a random fashion, which ends up in orientation A.

The last chapter of this work concerns the octamer GVG(VPGVG), which serves as a minimalistic elastin-like model system. By using CD and FTIR spectroscopy in a temperature range between 2 and ~95 °C the behaviour of the oligopeptide is investigated in presence of osmolytes and denaturants. The pure peptide behaves as a two-state system which undergoes an inverse temperature folding transition. The addition of cosolvents like glycerol, in higher concentrations, TFE and LiI stabilizes the folded state. As result, the population of type II β-turns increases also at lower temperatures. On the contrary, common denaturants like urea and GuHCl induce turns/loops at low temperature. The type II β-turns do not appear anymore at

higher temperatures, either. The form of the CD spectra, however, does not exclude the possibility of intramolecular β-sheets, which could develop in solution from peptide-peptide associations into dimer or bigger aggregates. Positive enthalpy and entropy changes, at room temperature, suggest that the folding is a consequence of hydrophobic interactions which are largely driven by the increase in entropy of water.

5   Zusammenfassung

Eine der wichtigsten aktuellen Herausforderungen der modernen Biowissenschaft ist die Annäherung experimenteller Parameter an die Komplexität lebender Systeme. In diesem Zusammenhang hat das Interesse an Membrankompartimenten in den letzten Jahren zunehmende Aufmerksamkeit gewonnnen. Ein Teil dieser Doktorarbeit beschäftigt sich mit „raft" Mikrodomänen *in vitro* und der Messung ihrer Eigenschaften mit verschiedenen Methoden in Abhängigkeit von Temperatur, Druck und unterschiedlichen Lipidphasen. Im ersten Teil dieser Arbeit erlauben druckabhängige Messungen bei verschiedenen Temperaturen am „raft" Lipidsystem POPC/SM/Chol (33:33:33) die Erstellung eines *p, T*-Phasendiagramms. Als Methoden wurden Fourier Transform Infrarot Spektroskopie (FTIR) und Röntgenkleinwinkelstreuung (SAXS) angewendet. Fluide ungeordnete (l_d)/ fluide geordnete (l_o) + (gel geordnete (s_o)) Phasenkoexistenz breiten sich über einen weiteren Temperaturbereich von ca. 40 °C aus. Oberhalb von ~50 °C ist die fluide Phase überall erreicht. Die Druckmessungen zeigen, dass bei Raumtemperatur eine hohe Ordnung der Alkylketten entsprechend einer liquid und gel geordneten Phase erst bei ~1 kbar erreicht ist. Das mit der Neutronenkleinwinkelstreuung mit der Methode der Kontrastvariation untersuchte Lipidsystem DOPC(POPC)/SM/Chol (33:33:33) weist die Existenz von Mikrodomänen auch in Nanometer-Bereich nach. Als Ergebnis kann festgehalten werden, dass die biologisch relevanten „lipid-rafts" *in vitro* durch Dreikomponenten-Lipidmischungen als Modellsysteme untersucht werden können.

In Rahmen dieser Arbeit wurden als zweite Thematik die druckabhängigen Messungen (von 1 bis ~3000 bar) an den ausgewählten Lipidmischungen POPC/DLPC (50:50), DOPC/DPPC/Chol (34.5:34.5:31), and DOPC/SM/Chol (33:33:33) mit Hilfe der Zwei-Photonenanregungs-Fluoreszenzmikroskopie und Röntgenkleinwinkelstreuung durchgeführt. Die druckabhängigen Zwei-Photonenanregungs-Fluoreszenzmikroskopie Untersuchungen wurden in dünnen eingeschmolzenen Quarzkapillaren durchgeführt. Das ermöglichte die durch Druckänderung hervorgerufene Visualisierung der lokalen und morphologischen Modifikationen von GUVs. Die verschiedenen Lipidphasen der Vesikeln wurden durch *GP*-Änderungen ermittelt. Bei einer Erhöhung des Druckes nimmt der *GP*-Wert zu, da die Ordnung der Lipidketten unter Druck steigt. Alle drei untersuchten Systeme zeigen während der Messung „budding" und „fission" bei einem Druck von 200-300 bar. Der „budding"-Prozess hängt nicht mit einer Konformationsordnung der Membranen zusammen, die erst bei

viel höheren Drücken für alle drei untersuchten Systeme auftreten. „Budding" and „pinching-off" von kleinen Tochtervesikeln geschehen möglicherweise, um infolge der Erhöhung des Druckes die entstandene höhere Linienspannung zwischen den Domänen zu sinken. Die Form der Vesikel ändert sich in Abhängigkeit des Druckes unterschiedlich. Bei sinkendem Druck bricht die Lipidpackung zusammen, da die Ordnung der Lipidketten sinkt und sich die fluide Phase bildet. Allerdings können nicht die Vesikel die Menge des Wassers, die während der Messungen bei Erhöhung des Druckes abgegeben wurde, wieder absorbieren, daher verlieren die GUVs an Spannung und es werden morphologische Formübergänge, von sphärischen zu ellipsoidalen und zu polygonalen, zusammen mit Fluktuationen der Membranoberfläche und Abspaltung von Lipidmaterial beobachtet. Dabei zeigen die GUVs mit „rafts"-Mischungen, die 30 mol% Cholesterin enthalten, meistens nur eine sphärisch-ellipsoidale Form. Die Änderungen der GP-Werte sind mit den SAXS-Übergängen vergleichbar, die an MLVs beobachtet wurden. In natürlichen Systemen wurde beobachtet, dass Membranproteine in einem Druckbereich von 1-2 kbar ihre Funktion verlieren. Bei solchen Drücken erreicht die Lipid-Matrix eine Ordnung, die physiologisch inakzeptabel ist. Wie in diesem Kapitel erläutert, kann dieses Phänomen auch auf morphologische Änderungen der Membrane in Zusammenhang mit Druckänderungen zurückgeführt werden.

Der dritte Teil dieser Arbeit beschäftigt sich mit den Wechselwirkungen zwischen Proteinen und Modellbiomembranen in GUVs und in Langmuir-Monoschichten. Man kann durch verschiedene Anteile an Palmitoylphosphatidylcholin, Sphingomyelin und Cholesterin unterschiedliche Lipidphasen herstellen, wie z.B. $l_o + l_d$, $l_o + s_o$ und $l_d + l_o + s_o$. Die zwei-Photonanregungs-Fluoreszenzmikroskopie zeigt, dass der Einbau von N-Ras wt 1-181 MIC7 HDFarBodipy die ungeordnete Phase bevorzugt. Das spiegelt sich auch in der Einbaukinetik, die ~60% schneller in die fluide Phase geschieht. Trotzdem wird sich ca. 50% vom Protein auch in die „liquid-ordered"-Phase einbauen. Wenn nur eine l_o/s_o-Phasenkoexsistenz verfügbar ist, wird sich das Protein in der l_o-Phase ~2 mal mehr als in der Gelphase befinden. Allgemein kann man daraus schließen, dass N-Ras in dem Bindungsprozess in Modellbiomembranen die folgende Reihung bevorzugt: $l_d > l_o \gg s_o$. Jedoch zeigen AFM Untersuchungen, die eine genauere Auflösung erlauben (nm-Bereich), dass sich das Protein weiterhin auch an den Grenzen zwischen verschiedenen Domänen befindet. Dies begünstigt die Grenzenergie an der Randzone zwischen unterschiedlichen Phasen. Allgemein ist der Einbau von Proteinen in Lipidsystemen an der Grenzzone zu beobachten, wenn sie keine Präferenz zu einer bestimmten Phase haben (DUMAS, 1997; MOURITSEN, 2005) – wegen z.B.

hydrophober Wechselwirkungen – so dass die Proteine an die Randzone hinausgedrängt werden. Proteine, die sich an der Grenze von Lipiddoppelschichten mit Domänen einordnen, können Protein-Protein Wechselwirkungenprozesse begünstigen, wodurch es zur Proteinassoziationen kommen kann.

Mit Hilfe der Infrarot-Reflektions-Absorption-Spektroskopie (IRRAS) wurde die Orientierung des N-Ras-Proteine mit Hexadecyl- und Farnesylrest (N-Ras wt 1-181 MIC7 HDFarBodipy) und mit doppeltem Hexadecylrest (N-Ras wt 1-181 MIC7 HDHDOMe) untersucht. Durchgeführte Simulation an der Spektren für beide Proteine zusammen mit den experimentellen Daten weisen auf eine ähnliche Adsorption an der Luft/D$_2$O Oberfläche mit einer bestimmten Orientierung A (s. Abb. 3.42a). Da die HDHD-Isoform allerdings beim niedrigen Oberflächendruck erst mit einer ungeordneten Orientierung adsorbiert, folgt, dass die Adsorptionskinetik wegen der unterschiedlichen Ankerstrukturen für die beiden Isoformen unterschiedlich ist. Die Messungen an den injizierten Proteinen in einer Langmuir-Monoschicht, die aus der „rafts"-Lipidmischung (POPC/SM/Chol (50:25:25)) besteht, zeigen, dass sich beide Proteine mit ihren lipidierten Ankern in die Lipidschicht unter einem Oberflächendruck von 20 mN m^{-1} einbauen. Während bei Π =30 mN m^{-1} (der einem Doppelschichtzustand entsprechen sollte) das N-Ras mit Hexadecyl- und Farnesylrest vollständig aus dem Lipidfilm herausgedrückt wird, bleibt das N-Ras mit Hexadecylresten in der Lipidschicht verankert. Wiederum ein Vergleich mit den simulierten Daten zeigt, dass der Einbauprozess eine Änderung der Proteinorientierung aufweist. Bei hohem Oberflächendruck baut sich das N-Ras wt 1-181 MIC7 HDFarBodipy in die Lipidmonoschicht mit Orientierung A ein, die aber instabil ist. Dagegen baut sich N-Ras wt 1-181 MIC7 HDHDOMe zunächst mit einer ungeordneten Orientierung, die mit einer stabilen Orientierung A endet, auch bei hohen Oberfläckendrücken ein.

Anschließend wird im Rahmen dieser Arbeit das Oligopeptid GVG(VPGVG) in Anwesenheit von verschiedenen Cosolventien in einem Temperaturbereich von 2 bis ~95 °C mit Hilfe der Circular Dichroism (CD)- und FTIR-Spektroskopie untersucht. Dieses Octamer wurde als Model für das Protein Elastin gewählt. Es ist ein einfaches Zwei-Phasen System mit einer Eigenart: Seine Konformation weist ein inverses Temperaturverhalten auf. Die Zugabe von Cosolventien wie Glycerol, bei einer hohen Konzentration (2 M), TFE and LiI stabilisieren die gefaltete Struktur des Peptides. Es folgt, dass der Anteil an Typ II β-Schleifen schon bei niedrigen Temperaturen zunimmt. Denaturantien wie Harnstoff und GuHCl

induzieren hingegen Schleifen-Strukturen schon bei $T = 2$ °C. Die Typ II β-Schleifen treten auch bei hoher Temperatur nicht mehr auf. Die Form der Kurve in der CD-Spektroskopie lässt allerdings auch nicht auf eine intramolekulare β-Faltblattstruktur schließen, die durch die Bildung von Dimeren und größeren Aggregaten in Lösung entstehen könnte. Bei Raumtemperatur weisen die positive Standardfaltungsenthalpie und -entropie darauf hin, dass es sich hier um eine hydrophobe Umwandlung handelt, die hauptsächlich von der Zunahme der Wasserentropie beeinflusst wird.

6   References

AHMED, S.N., BROWN, D.A. and LONDON, E. (1997) Biochemistry **36**, 10944-10953.

ALBERTS, B., BRAY, D., LEWIS, J., RAFF, M., ROBERTS, K. and WATSON, J.D. (1983) in *Molecular Biology of the Cell*, Garland Publishing, New York.

BAGATOLLI, L.A. and GRATTON, E. (1999) Biophys. J. **77**, 2090-2101.

BAGATOLLI, L.A. and GRATTON, E. (2000) Biophys. J. **79**, 434-447.

BAGATOLLI, L.A. (2003) Chem. Phys. Lip. **122**, 137-145.

BAUMGART, T., SAMUEL, T.H. and WEBB, W.W. (2003) Nature **425**, 821-824.

BAUMGART, T., DAS, T., WEBB, W.W. and JENKINS, J.T. (2005) Biophys. J. **89**, 1067-1080.

BENEY, L., PERRIER, J.M., HAYERT, M. and GERVAIS, P. (1997) Biophys. J. **72**, 1258-1263.

BERNDL, K., KÄS, J., LIPOWSKY, R., SACKMANN, E. and SEIFERT, U. (1990) Europhys. Lett. **13**, 659-664.

BIRGE, R.R. (1986) Acc. Chem. Res. **19**, 138-146.

BLANCO, F.J., JIMENEZ, M.A., PINETA, A., RICO, M., SANTORO, J. and NIETO, J.L. (1994) Biochemistry **33**, 6004-6014.

BLOOM, M., EVANS, E. and MOURITSEN, O.G. (1991) Q. Rev. Biophys. **24**, 293-297.

BLUME, A. (1979) Biochim. Biophys. Acta **557**, 32-44.

BROWN, D.A. and ROSE J.K. (1992) Cell **68**, 533-544.

BROWN, D.A. and LONDON, E. (1997) Biochem. Biophys. Res. Commun. **240**, 1-7.

BROWN, D.A. and LONDON, E. (1998) J. Membr. Biol. **164**, 103-114.

CACACE, M.G., LANDAU, E.M. and RAMSDEN, J.J. (1997) Q. Rev. Biophys. **30**, 241-277.

CHOY, E., CHIU, V.K., SILLETTI, J., FEOKTISTOV, M., MORIMOTO, T., MICHAELSON, D., IVANOV, I.E. and PHILIPS, M.R. (1999) Cell **98**, 69-80.

CZESLIK, C., ERBES, J. and WINTER, R. (1997) Europhys. Lett. **37**, 577-582.

DAMAY, P., LECLERCQ, F and CHIEUX, P. (1984) J. Phys. Chem. **88**, 3734-3740.

DE ALMEIDA, R.F.M., FEDOROV, A. and PRIETO, M. (2003) Biophys. J. **85**, 2406-2416.

DIETRICH, C., BAGATOLLI, L.A., VOLOVYK, Z.N., THOMPSON, N.L., LEVI, M., JACOBSON, K. and GRATTON, E. (2001) Biophys. J. **80**, 1417-1428.

DÖBEREINER, H.G., KÄS, J., NOPPL, D., SPRENGER, I. and SACKMANN, E. (1993) Biophys. J. **65**, 1396-1403.

DUMAS, F., SPEROTTO, M.M., LEBRUN, M.C., TOCANNE, J.F. and MOURITSEN, O.G. (1997) Biophys. J. **73**, 1940-1953.

FARGE, E. and DEVAUX, P.F. (1992) Biophys. J. **61**, 347-357.

FERON, O., BELHASSEN, L., KOBZIK, L., SMITH, T.W., KELLY, R.A. and MICHEL, T. (1996) J. Biol. Chem. **271**, 22810-22814.

FLACH, C.R., GERICKE, A. and MENDELSOHN, R. (1997) J. Phys. Chem. **101**, 58-65.

FOSTER, L.J., DE HOOG, J.E. and MANN, M. (2003) Procl. Natl. Acad. Sci. U.S.A. **100**, 5813-5818.

FRA, A.M., WILLIAMSON, E., SIMONS, K. and PARTON, R.G. (1995) Procl. Natl. Acad. Sci. U.S.A. **92**, 8655-8659.

GANDHAVADI, M., ALLENDE, D., VIDAL, A., SIMON, S.A. and MCINTOSH, T.J. (2002) Biophys. J. **82**, 1469-1482.

GIEHL, A., LEMM, T., BARTELESEN, O., SANDHOFF, K. and BLUME, A. (1999) Eur. J. Biochem. **261**, 650-658.

GOMASHCHI, F., ZHANG, X., LIU, L. and GELB, M.H. (1995) Biochemistry **34**, 11910-11918.

GREENFIELD, N. and FASMAN, G.D. (1969) Biochemistry **8**, 4108-4116.

HANCOCK, J.F., PATERSON, H. and MARSHALL, C.J. (1990) Cell **63**, 133-139.

HERBERHOLD, H., MARCHAL, S., LANGE, R., SCHEYHING, C.H., VOGEL, R.F. and WINTER, R. (2003) J. Mol. Biol. **330**, 1153-1164.

HOOPER, N.M. (1999) Mol. Membr. Biol. **16**, 145-156.

HUSTER, D., VOGEL, A., KATZKA, C., SCHEIDT, H.A., BINDER, H., DANTE, S., GUTBERLET, T., ZSCHÖRNIG, O., WALDMANN, H. and ARNOLD, K. (2003) J. Am. Chem. Soc. **125**, 4070-4079.

IKONEN, E. and PARTON R.G. (2000) Traffic **1**, 212-217.

JANOSCH, S., NICOLINI, C., LUDOLPH, B., PETERS, C., VOLKERT, M., HAZLET, T.L., GRATTON, E., WALDMANN, H. and WINTER, R. (2004) J. Am. Chem. Soc. **126**, 7496-7503.

JOHNSON, D.R., BHATNAGAR, R.S., KNOLL, L.J. and GORDON, J.I. (1994) Ann. Rev. Biochem. **63**, 869-914.

JÜLICHER, F. and LIPOWSKY, R. (1993) Phys. Rev. Lett. **70**, 2964-2967.

JÜLICHER, F. and LIPOWSKY R. (1996) Phys. Rev. E **53**, 2670-2684.

KAHMS, M. (2004) in *Graduierte Analyse der Ras-vermittelten Signaltransduction in Systemen unterschiedlicher Komplexität*, Dissertation, Bochum.

KÄS, J. and SACKMANN, E. (1991) Biophys. J. **60**, 825-844.

KENNEDY, S.M. and LYTLE, F.E. (1986) Anal. Chem. 58, 2643-2647.

KENTSIS, A. and SOSNICK, T.R. (1998) Biochemistry **37**, 14613-14622.

KENWORTHY, A.K., PETRANOVA, N. and EDIDIN, M. (2000) Mol. Biol. Cell **11**, 1645-1656.

KERTH, A.M. (2003) in *Infrarot-Raflextions-Absorptions-Spektroskopie an Lipid-, Peptid- und Flüsssigkristall-Filmen an der Luft/Wasser-Grenzfläche* Dissertation, Halle.

KRAINEVA, J., NARAYANAN, R.A., KONDRASHKINA, E., THIYAGARAJAN, P. and WINTER R. (2005) Langmuir **21**, 3559-3571.

KRASNOWSKA, E., GRATTON, E. and PARASASSI, T. (1998) Biophys. J. **74**, 1984-1993.

LAI, E.C. (2003) J. Cell Biol. **162**, 365-370.

LE, P.U., GUAY, G., ALTSCHULER, Y. and NABI, I.R. (2002) J. Biol. Chem. **277**, 3371-3379.

LI, X.M., MOMSEN, M.M., SMABY, J.M., BROCKMAN, H.L. and BROWN, R.E. (2001) Biochemistry **40**, 5954-5963.

LIPOWSKY, R. (1992) J. Phys. II France **2**, 1825-1840.

LIPOWSKY, R. and SACKMANN, E. (1995) in *Structure and dynamics of membranes*, Vols. 1A, 1B, Elsevier, Amsterdam.

LIPOWSKY, R. and SACKMANN, E. (1995) in *Handbook of Biological Physics*, Vol I, Elsevier, Amsterdam.

LOMMERSE, P.H.M., BLAB, B.A., COGNET, L., HARMS, G.S., SNAAR-JAGALSKA, B.E., SPAINK, H.P. and SCHMIDT, T. (2004) Biophys. J. **86**, 609-616.

LU, Z.X., FOK, K.F., ERICKSON, B.W. and HUGLI, T.E. (1984) J. Mol. Chem. **259**, 7367-7370.

LUISI, P.L and WALDE, P. (2000) in *Giant Vesicle*, John Wiley & Sons, Chichester, England.

LUO, Y. and BALDWIN, R.L. (1998) J. Mol. Biol. **279**, 49-57.

MACKAY, D.J.G. and HALL, A. (1998) J. Biol. Chem. **273**, 20685-20688.

MELKONIAN, K.A., OSTERMEYER, A.G., CHEN, J.Z., ROTH, M.G. and BROWN, D.A. (1999) J. Biol. Chem. **274**, 3910-3917.

MENDELSOHN, R., BRAUNER, J.W. and GERICKE, A. (1995) Annu. Rev. Phys. Chem. **46**, 305-334.

MIAO, L., FOURCADE, B., RAO, M., WORTIS, M. and ZIA, R.K.P. (1991) Phys. Rev. A **43**, 6843-6856.

MOLUMBRES, M. and BARBACID, M. (2002) Nature **3**, 7-13.

MOORE, M.S. (1998) J. Biol. Chem. **273**, 22857-22860.

MOURITSEN, O.G. (1991) Chem. Phys. Lipids **57**, 179-194.

MOURITSEN, O.G. (2005) in *Life - As a matter of fat*, Springer-Verlag, Berlin.

MUNRO, S. (2003) Cell **115**, 377-388.

NABI, I.R. and LE, P.U. (2003) J. Cell Biol. **161**, 673-677.

NEEDHAM, D. and NUNN, R.S. (1990) Biophys. J. **58**, 997-1009.

NICOLINI, C., RAVINDRA, R., LUDOLPH, B. and WINTER, R. (2004) Biophys. J. **86**, 1385-1392.

NIV, H., GUTMAN, O., KLOOG, Y. and HENIS, Y.I. (2002) J. Cell Biol. **157**, 865-872.

OHVO-REKILÄ, H., RAMSTEDT, B., LEPPIMÄKI, P. and SLOTTE, J.P. (2002) Progr. Lip. Res. **41**, 66-97.

PANICK, G., MALESSA, R., WINTER, R., RAPP, G., FRYE, K.J. and ROYER, C. (1998) J. Mol. Biol. **275**, 389-402.

PARASASSI, T., DE STASIO, G., D'UBALDO, A. and GRATTON, E. (1990) Biophys. J. **57**, 1179-1186.

PARASASSI, T., DE STASIO, G., RAVAGNAN, G., RUSCH, R.M. and GRATTON, E. (1991) Biophys. J. **60**, 169-179.

PARASASSI, T. and GRATTON, E. (1995) J. Fluorescence. **5**, 59-70.

PARASASSI, T., GRATTON, E., YU, W.M, WILSON, P. and LEVI, M. (1997) Biophys. J. **72**, 2413-2429.

PARASASSI, T., KRASNOWSKA, E., BAGATOLLI, L.A. and GRATTON, E (1998**)** J. Fluor. **8**, 365-373.

PARTON, R.G. and RICHARDS, A.A. (2003) Traffic **4**, 724-738.

PERCZEL, A., HOLLÓSI, M., TUSNÁDY, G. and FASMAN, G.D. (1991) Protein Eng. **4**, 669-679.

PERCZEL, A., PARK, K. and FASMAN, G.D. (1992) Analyt. Biochem. **203**, 83-93.

PERCZEL, A., HOLLÓSI, M., SANDOR, P. and FASMAN, G.D. (1993) Int. J. Pept. Protein Res. **41**, 223-236.

PFEIFER, P. and OBERT, M. (1989) in *The fractal approch to hetereogeneous chemistry: surface, colloids, polymers,* John Wiley & Sons, Chichester.

PORTER, J.A., KEITH, E. and YOUNG, P.A.B. (1996) Science **274**, 255-259.

PRALLE, A., KELLER, P., FLORIN, E.L., SIMONS, K. and HÖRBOR, J.K.H. (2000) J. Cell Biol. **148**, 997-1007.

PRIOR, I.A., HARDING, A., YAN, J., SLUIMER, J., PARTON, R.G. and HANCOCK, J.F. (2001) Nature Cell Biol. **3**, 368-375.

RAMOS C.H.I. and BALDWIN, R.L. (2002) Protein Sci. **11**, 1771-1778.

RAMSTEDT, B. and SLOTTE, J.P. (1999) Biophys. J. **76**, 908-915.

RAMSTEDT, B. and SLOTTE, J.P. (2002) FEBS Lett. **531**, 33-37.

REIERSEN, H., CLARKE, A.R. and REES, A.R. (1998) J. Mol. Biol. **283**, 255-264.

REIERSEN, H. and REES, A.R. (2000) Protein Eng. **13**, 739-743.

REIS, O., WINTER, R. and ZERDA, T.W. (1996) Biochim. Biophys. Acta **1279**, 5-16.

RESH, M.D. (1999) Biochim. Biophys. Acta-Molecular Cell Research **1451**, 1-16.

RIETVELD, A., NEUTZ, S., SIMONS, K. and EATON, S. (1999) J. Biol. Chem. **274**, 12049-12054.

ROTHBERG, K.G., HEUSER, J.E., DONZELL, W.C., YING Y.-S., GLENNEY, J.R. and ANDERSON, R.G.W. (1992) Cell **68**, 673-682.

ROUSSEAU, R., SCHREINER, E., KOHLMEYER, A. and MARX, D. (2004) Biophys. J. **86**, 1393-1407.

ROY, S., LUETTERFORST, R., HARDING, A., APOLLONI, A., ETHERIDGE, M., STANG, E., ROLLS, B., HANCOCK, J.F. and PARTON, R.G. (1999) Nature Cell Biol. **1**, 98-105.

SACKMANN, E., DE DUWE, H.P. and HENGELHARD, H. (1986) Faraday Discuss. Chem. Soc. **81**, 281-290.

SCHERFELD, D., KAHYA, N. and SCHWILLE, P. (2003) Biophys. J. **85**, 3758-3768.

SCHNITZER, J.E., MCINTOSH, D.P., DVORAK, A.M., LIU, J. and OH, P. (1995) Science **269**, 1435-1439.

SCHROEDER, R., LONDON, E. and BROWN, D.A. (1994) Procl. Natl. Acad. Sci. USA. **91**, 12130-12134.

SCHUCK, S., HONSHO, M., EKROOS, K., SHEVCHENKO, A. and SIMONS K. (2003) Procl. Natl. Acad. Sci. USA. **100**, 5795-5800.

SCHUTZT, G.J., KADA, G., PASTUSHENKO, V.P. and SCHINDLER, N. (2000) EMBO **19**, 892-901.

SEFTON, B.M. and BUSS, J.E. (1987) J. Cell Biol. **104**, 1449-1453.

SEIFERT, U., BERNDL, K. and LIPOWSKY, R. (1991) Phys. Rev. A **44**, 1182-1202.

SEIFERT, U. (1993) Phys. Rev. Lett. **70**, 1335-1338.

SHARMA, P., VARMA, R., SARASIJ, R.C., IRA, GOUSSET, K., KRISHNAMOORTHY, G., RAO, M. and MAYOR, S. (2004) Cell **116**, 577-589.

SHAROM, F.J. and LEHTO, M.T. (2002) Biochem. Cell Biol. **80**, 535-549.

SILVIUS, J.R., DEL GIUDICE, D. and LAFLEUR, M. (1996) Biochemistry **35**, 15198-15208.

SIMINOVITCH, D.J., WONG, P.T.T. and MANTSCH, H.H. (1987) Biochemistry **26**, 3277-3287.

SIMONS, K. and IKONEN, E. (1997) Nature **387**, 569-572.

SIMONS, K. and TOOMRE, D. (2001) Nat. Rev. Mol. Cell Biol. **2**, 216.

SINENSKY, M. (2000) Biochim. Biophys. Acta-Molecular & Cell Biol. of Lipids **1529**, 203-209.

SINGER, S.J. and NICOLSON, G.L. (1972) Science **175**, 720-731.

SÖNNICHSEN F.D., VAN EYK, J.E., HODGES, R.S. and SYKES, B.D. (1992) Biochemistry **31**, 8790-8798.

STORRS, R.W., TRUCKSES, D. and. WEMMER, D.E. (1992) Biopolymers **32**, 1695-1702.

SVETINA, S. and ZEKS, B. (1989) Eur. Biophys. J. **17**, 101-111.

TAMM, L. and TATULIAN, A. (1997) Quat. Rev. Biophys. **30**, 365-429.

THORN, H., STENKULA, K.G., KARLSSON, M., ORTEGREN, U., NYSTROM, F.H., GUSTAVSSON, J. and STRALFORS, P. (2003) Mol. Biol. Cell **14**, 3967-3976.

TIMASHEFF, S.N. (1993) Ann. Rev. Biophys. Biomol. Struct. **22**, 67-97.

TIMASHEFF, S.N. (2002) Proc. Natl. Acad. Sci. USA. **99**, 9721-9726.

URRY, D.W. (1993) Angewandte Chem., Int. Ed. **32**, 819-941.

URRY, D.W. (1997) J. Phys. Chem. B **101**, 11007-11028.

VARMA, R. and MAYOR, S. (1998) Nature **394**, 798-801.

VEATCH, S.L. and KELLER, S.L. (2003) Biophys. J. **85**, 3074-3083.

VEATCH, S.L. and KELLER, S.L. (2003a) Phys. Rev. Lett. **84**, 725-726.

VON HALLER, P.D., DONOHOE, S., GOODLETT, D.R., AEBERSOLD, R. and WATTS, J.D. (2001) Proteomics **1**, 1010-1021.

WALLACE, B.A. (2000) J. Synch. Rad. **7**, 289-295.

WARY, K.K., MARIOTTI, A., ZURZOLO, C. and GIANCOTTI, F.G. (1998) Cell **94**, 625-634.

WILLINGHAM, M.C., BANKS-SCHELGEL, S.P. and PASTAN I.H. (1983) Exp. Cell Res. **149**, 141-149.

WINTER, R., GABKE, A., CZESLIK, C. and PFEIFER P. (1999) Phys. Rev. E **60**, 7354-7359.

WINTER, R. (2002) Biochim. et Biophys. Acta **1595**, 160-184.

WITTINGHOFER, F., KRENGEL, U., JOHN, J., KABSCH, W. and PAI, E.F. (1991) Environ Health Perspect **93**, 11-15.

WU, J., YANG, J.T. and WU, C.-S. S. (1992) Analyt. Biochem. **200**, 359-364.

WYMAN, J.JR. (1964) Adv. Protein Chem. **19**, 223-286.

ZACHARIAS, D.A., VIOLIN, J.D., NEWTON, A.C. and TSIEN, R.Y. (2002) Science **296**, 913-916.

Lebenslauf

Persönliche Daten

Name   Chiara Nicolini

Geburtsdaten   23.05.1976 in Rovigo (Italien)

Schulausbildung

1982 – 1987   Grundschule Sacro Cuore in Rovigo

1987 – 1995   Gymnasium P.Paleocapa in Rovigo

Studium

WS 1995 – SS 1998   Alma Mater Studiorum Università di Bologna
                                 (Vordipl. Chemie)

WS 2000 – SS 2002   Dipl.-Chemie an der Universität Dortmund

05/2002 – 10/2002   Diplomarbeit mit dem Thema:
                                 „CD- und FTIR-spektroskopische
                                 Untersuchungen am Elastinfragment
                                 GVGVPGVG“

10/2002   Abschluss: Diplom

02/2003 – z.Z.   Promotion bei Prof. Dr. Winter an der Universität Dortmund

Berufstätigkeit

02/2003 – 05/2003   Wissenschaftliche Mitarbeiterin

05/2003 – 03/2006   Wissenschaftliche Angestellte